UNIVERSIDADE ESTADUAL DE CAMPINAS
Faculdade de Engenharia Mecânica

William Denner Pires Fonseca

PIV MEASUREMENTS FOR MODELLING SINGLE- AND TWO-PHASE LIQUID-LIQUID TURBULENT FLOWS INSIDE A CENTRIFUGAL PUMP IMPELLER

MEDIÇÕES PIV PARA MODELAGEM DE ESCOAMENTOS TURBULENTOS MONOFÁSICOS E BIFÁSICOS LÍQUIDO-LÍQUIDO DENTRO DE UM IMPELIDOR DE BOMBA CENTRÍFUGA

Campinas
2024

William Denner Pires Fonseca

PIV MEASUREMENTS FOR MODELLING SINGLE- AND TWO-PHASE LIQUID-LIQUID TURBULENT FLOWS INSIDE A CENTRIFUGAL PUMP IMPELLER

MEDIÇÕES PIV PARA MODELAGEM DE ESCOAMENTOS TURBULENTOS MONOFÁSICOS E BIFÁSICOS LÍQUIDO-LÍQUIDO DENTRO DE UM IMPELIDOR DE BOMBA CENTRÍFUGA

Thesis presented to the School of Mechanical Engineering of the University of Campinas in partial fulfillment of the requirements for the degree of Doctor in Mechanical Engineering in the area of Thermal and Fluids.

Tese apresentada à Faculdade de Engenharia Mecânica da Universidade Estadual de Campinas como parte dos requisitos exigidos para a obtenção do título de Doutor em Engenharia Mecânica, na Área de Térmica e Fluidos.

Orientador: Prof. Dr. Erick de Moraes Franklin

Coorientador: Prof. Dr. Rafael Franklin Lázaro de Cerqueira

ESTE TRABALHO CORRESPONDE À VERSÃO FINAL DA TESE DEFENDIDA PELO ALUNO WILLIAM DENNER PIRES FONSECA, E ORIENTADO PELO PROF. DR. ERICK DE MORAES FRANKLIN.

Campinas

2024

Ficha catalográfica
Universidade Estadual de Campinas (UNICAMP)
Biblioteca da Área de Engenharia e Arquitetura
Elizangela Aparecida dos Santos Souza - CRB 8/8098

	Fonseca, William Denner Pires, 1994-
F733p	PIV measurements for modelling single- and two-phase liquid-liquid turbulent flows inside a centrifugal pump impeller / William Denner Pires Fonseca. – Campinas, SP : [s.n.], 2024.
	Orientador: Erick de Moraes Franklin. Coorientador: Rafael Franklin Lázaro de Cerqueira. Tese (doutorado) – Universidade Estadual de Campinas (UNICAMP), Faculdade de Engenharia Mecânica.
	1. Bombas centrífugas. 2. Escoamento turbulento. 3. Escoamento bifásico. I. Franklin, Erick de Moraes, 1974-. II. Cerqueira, Rafael Franklin Lázaro de. III. Universidade Estadual de Campinas (UNICAMP). Faculdade de Engenharia Mecânica. IV. Título.

Informações Complementares

Título em outro idioma: Medições PIV para modelagem de escoamentos turbulentos monofásicos e bifásicos líquido-líquido dentro de um impelidor de bomba centrífuga
Palavras-chave em inglês:
Centrifugal pumps
Turbulent flow
Two-phase flow
Área de concentração: Térmica e Fluídos
Titulação: Doutor em Engenharia Mecânica
Banca examinadora:
Erick de Moraes Franklin [Orientador]
William Roberto Wolf
Rogério Gonçalves dos Santos
Henrique Stel de Azevedo
Igor Braga de Paula
Data de defesa: 19-08-2024
Programa de Pós-Graduação: Engenharia Mecânica

Identificação e informações acadêmicas do(a) aluno(a)
- ORCID do autor: https://orcid.org/0000-0001-5184-2193
- Currículo Lattes do autor: http://lattes.cnpq.br/5391475180246083

UNIVERSIDADE ESTADUAL DE CAMPINAS

FACULDADE DE ENGENHARIA MECÂNICA

TESE DE DOUTORADO ACADÊMICO

PIV MEASUREMENTS FOR MODELLING SINGLE- AND TWO-PHASE LIQUID-LIQUID TURBULENT FLOWS INSIDE A CENTRIFUGAL PUMP IMPELLER

MEDIÇÕES PIV PARA MODELAGEM DE ESCOAMENTOS TURBULENTOS MONOFÁSICOS E BIFÁSICOS LÍQUIDO-LÍQUIDO DENTRO DE UM IMPELIDOR DE BOMBA CENTRÍFUGA

Autor: William Denner Pires Fonseca

Orientador: Prof. Dr. Erick de Moraes Franklin

Coorientador: Prof. Dr. Rafael Franklin Lázaro de Cerqueira

A Banca Examinadora composta pelos membros abaixo aprovou esta Tese:

Prof. Dr. Erick de Moraes Franklin, Presidente

Universidade Estadual de Campinas - UNICAMP

Prof. Dr. William Roberto Wolf

Universidade Estadual de Campinas - UNICAMP

Prof. Dr. Rogério Gonçalves dos Santos

Universidade Estadual de Campinas- UNICAMP

Prof. Dr. Henrique Stel de Azevedo

Universidade Tecnológica Federal do Paraná - UTFPR

Prof. Dr. Igor Braga de Paula

Pontifícia Universidade Católica do Rio de Janeiro - PUC-Rio

A Ata de Defesa com as respectivas assinaturas dos membros encontra-se no SIGA/Sistema de Fluxo de Dissertação/Tese e na Secretaria do Programa da Unidade.

Campinas, 19 de agosto de 2024

To my princess, Maria Luiza.

To my parents, Genilma and Iranilson.

To my sister, Dayane.

Acknowledgments

Embora esta tese seja escrita em inglês, gostaria de expressar meus agradecimentos em minha língua materna.

É impossível descrever, em tão pouco espaço, a importância que meus pais, Iranilson e Genilma, tiveram na minha formação humana e acadêmica. Seu amor e constante incentivo foram fundamentais no meu processo educacional, culminando nesta tese de doutorado. A eles, devo praticamente tudo.

Gostaria também de mencionar minha irmã e companheira Dayane, meus primos Adson e Gracielle, e Samantha, que sempre me apoiaram em minhas decisões e me ajudaram de diversas formas durante todos esses anos.

Agradeço às minhas avós, Luiza e Maria, ao meu avô Severo e aos meus tios Ideneilton, Ideneilson, Idenilton, Gilvana, Vitalina e Gracileide, por todos os incentivos e pela constante preocupação comigo.

Agradeço também a todos os integrantes da república "CasAmarela" por todas as "pankas" na cozinha, os rolês e pelo acolhimento que me deram em Campinas.

Deixo aqui um agradecimento mais que especial aos meus irmãos de vida. Agradeço ao Felipe (Platinha) pela paciência nas discussões vazias sobre mecânica dos fluidos e mecânica quântica, e pela sua amizade incondicional. Ao Tomassela, pela compreensão, paciência, incentivo e carinho. Ao meu compadre Silvano, pelos conselhos, pela música e pelo acolhimento desde o meu primeiro dia em Campinas. Ao Henrique (Sequela), Vinicius (Carioca), Mauro (Mixto) e Guilherme (Duracell), pela sincera amizade e constante preocupação, que transformaram nossa relação em uma verdadeira irmandade. E, por fim, ao meu irmão de vida, André (Dac), por tudo aquilo que não cabe aqui, mas principalmente por me mostrar o que é ser preto. "Noiz."

Não poderia deixar de agradecer aos meus orientadores, professor Dr. Erick de Moraes Franklin e professor Dr. Rafael Franklin Lázaro de Cerqueira, por acreditarem na minha capacidade científica, pela paciência, compreensão e todas as orientações cruciais no desenvolvimento e conclusão desta tese.

Agradeço ao grupo de pesquisas Artificial Lift and Flow Assurance (ALFA) e a todos os pesquisadores do Centro de Estudos de Energia e Petróleo (CEPETRO). Agradecimentos especiais ao meu colega de laboratório e amigo Rodolfo, Natan, Kenji, William Monte Verde e ao Prof. Dr. Marcelo de Souza Castro. Agradeço aos competentes técnicos da oficina do ALFA, em especial ao Claudio Varani, Luís Gustavo Silva e Edmilson Sanches, cuja dedicação foi fundamental para o sucesso deste trabalho.

Agradeço o apoio do EPIC – Centro de Inovação em Produção de Energia e da FAPESP – Fundação de Amparo à Pesquisa do Estado de São Paulo (Processo Número 2017/15736-3). Agradeço também à FAPESP pela disponibilização do sistema PIV utilizado nesta pesquisa por meio do programa Equipamento Multiusuário (Processo Número 2019/20870-6). Reconheço o apoio da ANP (Agência Nacional de Petróleo, Gás Natural e Biocombustíveis) através da regulamentação da taxa de P&D. Os agradecimentos também se estendem ao Centro de Estudos de Energia e Petróleo (CEPETRO) e à Faculdade de Engenharia Mecânica (FEM).

Reitero meu agradecimento à empresa de energia Equinor pelo apoio financeiro ao projeto EPIC, que incentivou a produção deste trabalho. O presente trabalho foi realizado com o apoio do Conselho Nacional de Desenvolvimento Científico e Tecnológico (CNPq), processo nº 350825/2024-6.

Meus agradecimentos estendem-se, também, à Fundação de Desenvolvimento da Unicamp (FUNCAMP), pela concessão de bolsas de estudo que viabilizaram minha permanência no doutorado.

A todos, muito obrigado!

“Essa obrigação de resistir destrói muito da beleza que existe em nós (. . .)
Não ter a opção de ser vulnerável é muitas vezes desesperador.
A questão é que não há muitas opções para nós, além de ser forte.
A alternativa é virar estatística.”

Leandro “Emicida” Roque de Oliveira

Resumo

Os escoamentos turbulentos desempenham um papel dominante na operação de bombas centrífugas, que são amplamente utilizadas em ambientes industriais e em vários aspectos da vida humana. O campo de escoamento dentro dos canais do impelidor de uma bomba centrífuga é geralmente complexo, contendo estruturas turbulentas em uma ampla faixa de escalas de tempo e comprimento. Além disso, em determinadas situações, estas turbomáquinas operam em condições fora da condição de projeto, como é o caso dos escoamentos multifásicos. Um exemplo notável de operação de escoamento multifásico em bombas centrífugas é observado na mistura dispersa de óleo viscoso e água. Nesse contexto, o objetivo geral deste trabalho é estudar escoamentos monofásicos e bifásicos dentro de um impelidor de uma bomba centrífuga. Para isso, experimentos utilizando velocimetria de imagem de partículas resolvida no tempo (TR-PIV) em uma bomba de material transparente operando em diferentes condições foram conduzidos. Para o escoamento monofásico, as características estatísticas do escoamento turbulento foram calculadas a partir de médias do conjunto de fases de velocidade, vorticidade, energia cinética turbulenta, produção e dissipação de turbulência. Além disso, as características do escoamento instável foram observadas por meio da técnica POD (*proper orthogonal decomposition*). Os resultados indicam que o termo de produção de turbulência é a principal fonte de perda de energia no impulsor da bomba, e é particularmente pronunciada em condições operacionais de baixa vazão, caracterizadas por estruturas turbulentas de grande escala. Por outro lado, em situações onde as vazões excedem a condição de ponto de melhor eficiência (BEP), as estruturas de escoamento predominantes são marcadas por características de pequena escala, atribuídas principalmente à dissipação local de turbulência. No que se refere ao escoamento bifásico, foi introduzida uma metodologia para a caracterização do escoamento óleo-água disperso no impelidor. Para atingir esse objetivo, um conjunto de técnicas de processamento de imagens de aprendizagem profunda foi desenvolvido e aplicado às aquisições brutas de TR-PIV para distinguir gotículas de óleo (fase dispersa) de partículas traçadoras adicionadas à água (fase contínua). Essa análise demonstrou que a fase dispersa tende a se acumular nas pás de sucção, consequência de zonas de recirculação da fase contínua do escoamento. Além disso, observou-se que o campo de velocidade da fase contínua no escoamento bifásico se assemelha muito ao do escoamento monofásico. Essa semelhança está relacionada ao fato de que a altura manométrica da bomba permanece aproximadamente a mesma para ambos os tipos de escoamento.

Palavras-chave: PIV; bomba centrífuga; escoamento turbulento; perda de energia; escoamento bifásico.

Abstract

Turbulent flows play a dominant role in the operation of centrifugal pumps, which are widely used in industrial environments and various aspects of human life. The flow field within channels of a centrifugal pump impeller is generally complex, containing turbulent structures over a wide range of time and length scales. Furthermore, in certain situations, these turbomachines operate under off-design conditions, as seen in multiphase flows. A notable example of multiphase flow operation in centrifugal pumps is observed in the dispersed mixture of viscous oil and water. In this context, the general objective of this work is to study single-phase and two-phase flows inside a centrifugal pump impeller. For this, experiments using time-resolved particle image velocimetry (TR-PIV) in a transparent material pump operating under different conditions were conducted. For single-phase flow, the statistical characteristics of turbulent flow were calculated from phase-ensemble averages of velocity, vorticity, turbulent kinetic energy, turbulence production, and dissipation. Furthermore, the characteristics of the unsteady flow were observed using the POD (proper orthogonal decomposition) technique. The results indicate that the turbulence production term is the main source of energy loss in the pump impeller, particularly pronounced under low-flow rate operating conditions characterized by large-scale turbulent flow structures. On the other hand, in situations where flow rates exceed the best efficiency point (BEP) condition, the predominant flow structures are marked by small-scale characteristics, mainly attributed to local dissipation of turbulence. Regarding two-phase flow, a framework was introduced to characterize the dispersed oil-water flow within the impeller. To achieve this goal, a set of deep learning image processing techniques was developed and applied to raw TR-PIV acquisitions to distinguish oil droplets (dispersed phase) from seeding particles added to water (continuous phase). This analysis demonstrated that the dispersed phase tends to accumulate in the suction blades due to recirculation zones of the continuous phase flow. Furthermore, it was observed that the velocity field of the continuous phase in two-phase flow closely resembles that of single-phase flow, indicating that the pump head remains approximately the same for both types of flow.

Keywords: PIV; centrifugal pump; turbulent flow; energy loss; two-phase flow.

List of figures

List of tables

List of symbols and acronyms

Latin characters

A	interrogation window area	[px^2]
$\boldsymbol{A}$	eigenvectors or area normal vectors	[-]
$\boldsymbol{a}$	acceleration	[$\mathrm{m/s}^2$]
a_k	POD time coefficients	[-]
$\mathbf{B}$	analyzed flow variables	[-]
b_i	low-pass filter bandwidths constants for the i-direction	[-]
$\mathbf{C}$	correlation matrix (PIV and POD)	[-]
C_s	Smagorinsky constant	[-]
c	circumferential position	[°]
D_a	aperture diameter of the lens	[mm]
D_{ij}	viscous diffusion	[m^2/s]
d	impeller diameter	[mm]
d_p	seeding particle diameter	[μm]
d_s	point response function	[-]
d_T	total diameter of the seeding particle image	[μm]
e	blade thickness	[mm]
$e_{ff,\mathrm{pump}}$	pump efficiency	[-]
f	focal length of the camera lens	[mm]
$f^{\#}$	numerical aperture of the camera lens	[mm]
g	acceleration of gravity	[$\mathrm{m/s}^2$]
H_{ideal}	ideal head	[m]
H_{imp}	impeller head	[m]
H_{pump}	pump head	[m]
h	blade height	[mm]
I_i	image intensity distribution	[-]

k	turbulent kinetic energy	[m²/s²]
L	energy loss	[W]
L_C	CMOS array dimension	[px]
L_{IW}	interrogation window dimension	[px]
L_r	smallest resolved length scale with the PIV system	[mm]
L_v	length scale of the viewing area in the flow	[mm]
l	integral length	[mm]
M_{dry}	torque produced by impeller under “dry running” operation	[N.m]
M_{ideal}	ideal torque at pump shaft	[N.m]
M_{imp}	torque produced by impeller	[N.m]
M_{pump}	torque at pump shaft	[N.m]
$\dot{m}$	mass flow rate	[kg/s]
N	number of snapshots	[-]
P	pressure	[Pa]
$P_{\text{h,ideal}}$	ideal hydraulic power	[W]
$P_{\text{h,imp}}$	impeller hydraulic power	[W]
$P_{\text{h,pump}}$	pump hydraulic power	[W]
$P_{\text{in,pump}}$	pump input power (mechanical power)	[W]
Q	volumetric flow rate	[m³/h]
Re_c	Reynolds number of the impeller’s channel	[-]
Re_Ω	Reynolds number based on impeller angular speed	[-]
r	impeller radius	[mm]
$\mathbf{r}$	position vector	[mm]
s_U	standard error of PIV measurements	[-]
$\lvert\bar{S}\rvert$	filtered rate of strain	[s^{-1}]
$\bar{S}_{ij}$	strain rate tensor	[s^{-1}]
T	temperature	[°C]
T_{ij}	turbulent transport	[Pa]
$\mathbf{U}$	instantaneous velocity vector	[m/s]

U_p	seeding particle velocity	[m/s]
U_{tip}	blade tip speed	[m/s]
$\mathbf{u}$	velocity fluctuation vector	[m/s]
$\tilde{\mathbf{u}}$	phase-dependent velocity vector	[m/s]
V_t	circumferential velocity of ideal Euler's flow	[m/s]
$\boldsymbol{V}^*$	Hermitian matrix	[-]
W	relative velocity	[m/s]
x	spatial direction	[m]
z_c	PIV confidence coefficient	[-]

Greek characters

Δ	interrogation window size	[mm]
ΔP_{imp}	pressure increment produced by impeller	[Pa]
ΔP_{pump}	pressure increment produced by pump	[Pa]
Δt	time between laser pulse	[μs]
ε_{ij}	turbulence dissipation rate	[m^2/s^3]
ε_{SGS}	SGS turbulence dissipation rate	[m^2/s^3]
ϵ_μ	uncertainty associated with the mean PIV velocity	[-]
η_k	Kolmogorov scale	[μm]
θ	impeller angular position	[°]
$\mathbf{\Lambda}$	eigenvalues	[-]
λ	wavelength of laser light	[nm]
μ	dynamic viscosity	[Pa.s]
ν	kinematic viscosity	[m^2/s]
ρ	density	[kg/m^3]
σ	relative deviation	[-]
$\boldsymbol{\tau}_{ij}$	stress tensor	[N/m^2]
ϕ_k	POD spatial functions	[-]

Ω	angular speed	[rad/s]
ω	vorticity	[s^{-1}]

Other notations

$\Im$	FFT operator	[-]
$\mathcal{N}$	rotational speed	[rpm]
$\mathcal{P}_{ij}$	turbulence production	[m^2/s^2]
$u_i u_j$	Reynolds stress	[Pa]
$\forall$	volume	[m^3]
$\langle \quad \rangle$	phase-ensemble average	[-]

Subscripts

1	relative to x-direction
2	relative to y-direction
CS	control surface
CV	control volume
PS	pressure side
SS	suction side
o	relative to oil
p	relative to seeding particles
w	relative to water
i, j, k, m, n	spatial index

Superscript

$(\ )^*$	non-dimensional variables
$(\ )^\dagger$	transpose of a matrix
$(\ )^{TM}$	trademark
$(\ )^{®}$	trademark

Acronyms and abbreviations

BEP	Best Efficiency Point
CFD	Computational Fluid Dynamics
CDD	Charged Coupled Device
CNN	Convolutional Neural Network
CMOS	Complementary Metal-Oxide-Semiconductor
CPVC	Chlorinated Polyvinyl Chloride
DCC	Direct Cross-Correlation
DFT	Direct Fourier Transform
EMP	Endoscope Measuring Probe
FFT	Fast Fourier Transform
GAN	Generative Adversarial Network
GUI	Graphical User Interface
HSI	High-Speed Imaging
IW	Interrogation Window
LE	Leading Edge
LDV	Laser Doppler Velocimetry
LES	Large Eddy Simulation
LIF	Laser-Induced Fluorescence
LPSA	Laser Particle Size Analyzer

LOV	Labeled Object Velocimetry
OMOP	Optical Multimode Online Probe
POD	Proper Orthogonal Decomposition
PIV	Particle Image Velocimetry
PTV	Particle Tracking Velocimetry
RMS	Root Mean Square
SMM	Subtract Sliding Minimum
SPOD	Spectral Proper Orthogonal Decomposition
SVD	Singular Value Decomposition
TE	Trailing Edge
TKE	Turbulent Kinetic Energy
TR-PIV	Time-resolved Particle Image Velocimetry
UES	Ultrasonic Extinction Spectrometer
UPS	Uninterruptible Power Supply

Contents

1 Introduction

This chapter presents an overview of centrifugal pumps and their industrial applications, as well as their complications when subjected to operating conditions outside the design condition. Moreover, the main objectives of this research are defined. Finally, an outline of this thesis is presented, delineating its structure and contents.

1.1 Motivation and approach

Pumping systems constitute a substantial proportion of contemporary energy consumption. As reported by Volk (2013), centrifugal pumps indirectly contribute to approximately 20% of the global electricity demand, a number that reveals their paramount significance not only in industrial settings but also in various human activities. In light of the escalating emphasis on energy conservation and extended operational lifetimes, the study of flow structures within the impeller, the primary component of the centrifugal pump, has emerged as a persistent subject of investigation in the fluid mechanics field.

Despite their widespread use in industry, the flow structure within the impeller remains incompletely understood, particularly under off-design conditions, where the flow exhibits high temporal and spatial velocity gradients, regions of intense vorticity, and flow separation zones. Consequently, gaining a comprehensive understanding of the flow phenomena at different operational conditions assumes critical importance for the efficient design, assembly, and operation of centrifugal pumps. To address this issue, various research efforts have been undertaken to explore the internal flow behavior of centrifugal pumps. Pedersen *et al.* (2003), Krause *et al.* (2005), Feng *et al.* (2009), Keller *et al.* (2014), and Li *et al.* (2020a) employed the particle image velocimetry (PIV) technique to investigate single-phase flows within impellers. However, due to the intricacies associated with conducting PIV experiments and developing transparent pumps, most of these studies have been restricted to obtaining average flow field results. Consequently, the understanding of single-phase flow behavior and its correlation with pump efficiency remains an open question, necessitating further investigation, especially through methodologies capable of characterizing the unstable flow occurring within the impeller and its relationship with the pump head.

In some applications, such as petrochemical, chemical, food, energy, nuclear, and pharmaceutical industries, centrifugal pumps are employed for handling two-phase flows. Centrifugal pumps are fundamentally designed to work with incompressible and low-viscosity fluids. Consequently, the presence of a compressible phase or water-oil mixtures capable of forming highly viscous emulsions imposes limitations on their operational efficiency. When dealing with multiphase flows, centrifugal pumps commonly encounter efficiency losses and instabilities, which may result in undesirable consequences like reduced pump lifespan.

Recent research has focused on identifying gas-liquid two-phase flow patterns (Estevan, 2002; Barrios & Prado, 2009a,b; Monte Verde *et al.*, 2017; Shao *et al.*, 2018; Zhao *et al.*, 2021) and employing particle tracking techniques to investigate droplet dynamics (Perissinotto *et al.*, 2019b,a, 2020; Stel *et al.*, 2019; Cubas *et al.*, 2020). Despite these efforts, the characterization of unstable flows occurring within the pumps, as well as the influence of dispersed phases on the continuous phase flow fields, remains a relatively underexplored area of study.

Based on the preceding paragraphs, it is evident that the investigation of flow dynamics in centrifugal pumps is a contemporary and active area of research, as evidenced by recent studies. Nevertheless, despite these efforts, there remain numerous unexplored aspects related to the utilization of experimental measurements in the analysis of these devices. In the context of single-phase flows, a comprehensive investigation of the unstable flow phenomena and its inherent connection to energy dissipation within the pump holds considerable interest. By conducting such a characterization, it becomes possible to quantitatively and qualitatively analyze the energy losses that take place during pump operation. The outcomes of this investigation can be practically applied to enhance the understanding and optimization of energy usage in centrifugal pumps. Regarding two-phase liquid-liquid flows, the presence and behavior of dispersed droplets within the continuous flow field can be better comprehended through the implementation of PIV techniques. This approach enables a more profound insight into the influence of droplets on the overall flow dynamics and aids in developing a more comprehensive understanding of the multiphase flow behavior in centrifugal pumps.

Based on this context, the present work aimed to carry out an experimental study to characterize the single-phase and two-phase flows inside a centrifugal pump impeller. For this, experiments were carried out using time-resolved particle image velocimetry (TR-PIV) in a transparent material pump operating under different conditions.

For the single-phase flow analysis, the statistical properties of the turbulent flow were acquired through phase-ensemble averages of velocities, turbulent kinetic energy, vorticity, turbulence production, and turbulence dissipation. The application of modal decomposition techniques allowed an in-depth examination of the unstable flow patterns by establishing correlations between the turbulent flow field and the energy losses occurring within the centrifugal pump impeller.

Regarding the investigation of two-phase flow, the study focused on oil-water dispersion fields to elucidate the influence of the dispersed oil phase on the continuous water phase. A set of deep learning image processing techniques was developed and applied to raw TR-PIV acquisitions to distinguish oil droplets (dispersed phase) from seeding particles added to water (continuous phase). Furthermore, a new method was developed to evaluate the phase-ensemble average fields from TR-PIV acquisitions.

1.2 General objective

The primary aim of this investigation was to conduct an experimental analysis using PIV measurements for both single-phase flows and two-phase liquid-liquid dispersions within a centrifugal pump impeller. The analysis involves characterizing the flow of low-viscosity liquids in the channels of a radial impeller, intending to propose a relationship between flow dynamics and pump performance.

1.3 Specific objectives

- Investigate the hydrodynamics of single-phase flow in a pump impeller by analyzing velocity fields, vorticity, turbulent kinetic energy, turbulence production, and turbulence dissipation using PIV as a measurement method;

- Utilize the POD technique to identify and analyze the turbulent scales present in the single-phase flow under different pump operating conditions;
- Explore the correlation between the characteristics of turbulent single-phase flow and the resulting energy losses experienced within the pump impeller;
- Employ deep learning techniques to study the behavior of two-phase oil-in-water dispersions and gain insights into how the dispersed phase influences the average characteristics of the continuous phase.

1.4 Outline of the thesis

The structure of this PhD thesis is as follows: Chapter 2 provides a comprehensive literature review focusing on fundamental concepts related to centrifugal pumps, PIV, turbulent flows, and flow patterns occurring within the centrifugal pump's impellers.

In Chapter 3, the experimental apparatus utilized for the investigation of two flows - single-phase flow and two-phase flow - is described in detail. This includes information about the centrifugal pump prototype, the test circuit, and the PIV system implementation.

Chapter 4 presents a description of the methodologies used to obtain the results of this PhD thesis. The delineation encompasses pre-processing protocols and the computational processing framework pertinent to PIV method. Furthermore, a mathematical description is furnished, coupled with a detailed elucidation of the architectural construct of the U-Net neural network used for the analysis of the two-phase flow.

Chapter 5 presents the outcomes obtained through the application of the PIV method for single-phase flow. This section discusses the phase-ensemble averages of velocities, vorticity, and turbulence, along with energy loss contour plots. Additionally, a POD analysis on the impeller is carried out and its findings are discussed. The findings of the PIV method employed for the two-phase oil-water dispersion are reported in Chapter 6, with a particular focus on time-averaged fields. Lastly, Chapter 7 offers overall concluding remarks and outlines potential directions for future research.

1.5 Main contributions

The following main contributions achieved in this PhD thesis are highlighted:

- Use of robust, time-resolved visualization equipment and precise instruments to characterize the turbulent flow of water in a centrifugal pump impeller;
- Application of the TR-PIV technique and the POD modal decomposition method;
- Analysis of velocity fields, turbulent kinetic energy, production, and dissipation of turbulence in the main component of a centrifugal pump, subjected to a rotating motion;
- Application of the large-scale PIV approach to calculate the local turbulence dissipation rate;
- Determination of turbulent flow field scales and their correlation with energy loss in the impeller;
- Application of the TR-PIV technique alongside neural networks to evaluate a two-phase liquid-liquid flow in the impeller.

1.6 Related publications

The following publications resulted from this PhD thesis:
Articles in indexed journals

- Fonseca, W. D. P. et al. 2024. Particle image velocimetry in the impeller of a centrifugal pump: Relationship between turbulent flow and energy loss. Flow Measurement and Instrumentation, 99, 102675.
- Fonseca, W. D. P. et al. 2023. Particle image velocimetry in the impeller of a centrifugal pump: A POD-based analysis. Flow Measurement and Instrumentation, 94, 102483.

Full papers and abstracts in conference proceedings

- Fonseca, W. D. P. et al. 2024. Convolutional neural network-based approach for PIV measurement of two-phase liquid-liquid turbulent flow inside a centrifugal pump impeller. In: *20th Brazilian Congress of Thermal Sciences and Engineering*, Foz do Iguaçu–PR-Brazil.

- Cerqueira, R. F. L., Fonseca, W. D. P. et al. 2024. Pressure field in a centrifugal pump computed from particle image velocimetry. In: *XIV Escola de Primavera de Transição e Turbulência*, São João da Boa Vista–SP-Brazil.

- Fonseca, W. D. P. et al. 2023. Estimation of the dissipation rate in a centrifugal pump impeller by using PIV. In: *27th International Congress of Mechanical Engineering*, Florianópolis–SC-Brazil.

- Fonseca, W. D. P. et al. 2023. Turbulent two-phase liquid-liquid flow inside a centrifugal pump impeller. In: *11th International Conference on Multiphase Flow*, Kobe-Japan.

- Fonseca, W. D. P. et al. 2023. A coupled PIV/PTV framework for the determination and assessment of interfacial momentum closure in dispersed two-phase rotating flows. In: *7th Multiphase Flow Journeys*, Rio de Janeiro-RJ-Brazil.

- Fonseca, W. D. P. et al. 2022. Proper orthogonal decomposition of the turbulent flow in an impeller of a centrifugal pump. In: *20th International Symposium on Application of Laser and Imaging Techniques to Fluid Mechanics*, Lisbon-Portugal.

- Fonseca, W. D. P., Cerqueira, R. F. L., Franklin, E. M. 2021. A study on image pre-processing and PIV processing techniques for fluid flows. In: *26th International Congress of Mechanical Engineering*, Florianópolis–SC-Brazil.

2 Literature review

This chapter introduces basic concepts and definitions that are fundamental to understanding this thesis. The chapter was divided into five sections. In Sec. 2.1, fundamental concepts about centrifugal pumps are presented, such as the operating principle, basic pump performance parameters, and elementary pump theory. In Sec.2.2, the PIV flow measurement method is presented. In Sec.2.3, some concepts related to turbulent flows are presented. Among these, the mean-flow equations are described. From these equations of motion, terms such as the Reynolds stress tensor, turbulence production, and dissipation are defined. A description of the turbulent dissipation rate and the POD method is also presented at the end of this section. Sections 2.4 and 2.5 present a bibliographical review of a set of academic works found in the literature on flow characterization in centrifugal pumps. Studies related to single-phase and two-phase flow inside pumps are discussed as well.

2.1 Fundamental concepts about centrifugal pumps

2.1.1 Basic principles and components

Pumps are hydraulic machines used to transport fluids by performing work on them. As for their principle of operation, pumps can be classified into two categories: dynamic pumps or positive displacement pumps. Widely used in industrial applications, centrifugal pumps fit into the first classification.

A centrifugal pump according to Fig. 2.1 is essentially composed of an impeller rotating within a casing. Fluid enters axially through the eye of the casing, is caught up in the impeller blades, and is whirled tangentially and radially outward until it leaves through all circumferential parts of the impeller into the diffuser part of the casing. The fluid gains both velocity and pressure while passing through the impeller. The scrollt-shapede diffuser decelerates the flow and further increases the pressure. The impeller blades are usually backward-curved, as in Fig. 2.1. The blades may be open (separated from the front casing only by a narrow clearance) or closed (shrouded from the casing on both sides by an impeller wall). The diffuser may be vaneless, as in Fig. 2.1, or fitted with fixed vanes to help guide the flow toward the exit.

Figure 2.2 shows the meridional section and the plan view of an impeller. The leading face of the blade of the rotating impeller experiences the highest pressure for a given radius. It is called pressure surface or pressure side. The opposite blade surface with the lower pressure accordingly is the suction surface or suction side. Also defined in Fig. 2.2 are the leading edge LE and the trailing edge TE of the blade.

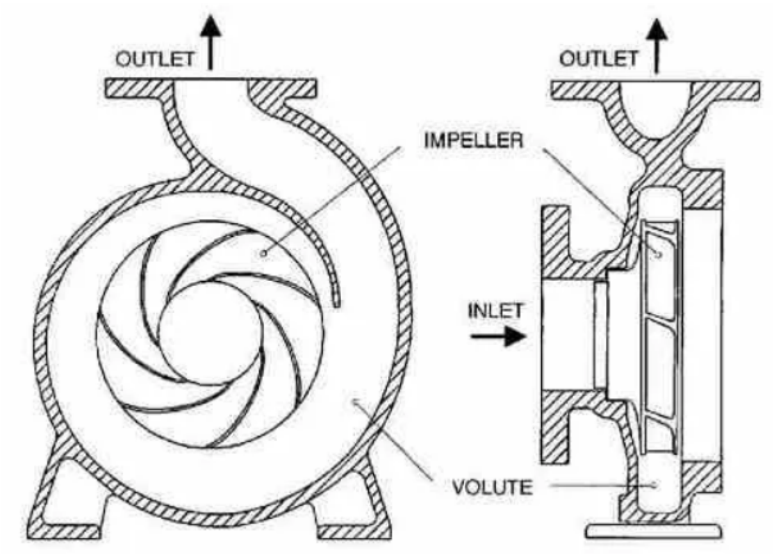

FIGURE 2.1 – Cutaway schematic of a typical centrifugal pump. Adapted from Lobanoff & Ross (2013).

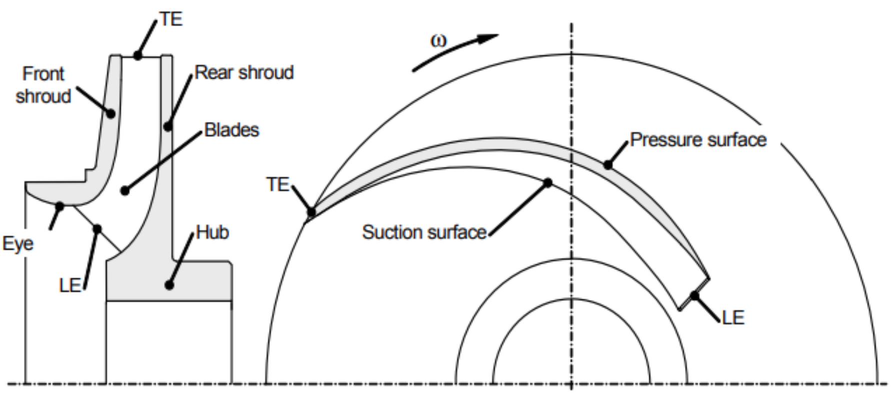

FIGURE 2.2 – Meridional section and plan view of a radial impeller (Gülich, 2008).

2.1.2 Pump performance

The amount of energy transferred by a centrifugal pump to a fluid is estimated from an energy balance at a control volume. Assuming a steady state, adiabatic, and isothermal flow of an incompressible fluid, in which the velocity and vertical elevation do not change significantly from the pump intake to discharge, we can define the head increment generated by the pump (H_{pump}).

$$H_{\text{pump}} = \frac{\Delta P_{\text{pump}}}{\rho \ g} \tag{2.1}$$

In Eq. (2.1), ΔP_{pump} represents the pressure increment from intake to discharge, ρ the water density e g the gravitational acceleration. The power delivered to the fluid by the pump is called hydraulic power ($P_{\text{h,pump}}$) while the power required to drive the motor-pump set is commonly named input power or brake horsepower ($P_{\text{in,pump}}$). They depend on the water flow rate (Q_w), torque at the pump shaft (M_{pump}), and angular speed of the pump ($\Omega = 2\pi\mathcal{N}$), as follows.

$$P_{\text{h,pump}} = \rho g H_{\text{pump}} Q_w \tag{2.2}$$

$$P_{\text{in,pump}} = \Omega M_{\text{pump}} \tag{2.3}$$

The power effectively transferred to the fluid is always lower than the power consumed by the pump. Thus, the pump efficiency ($e_{ff,\text{pump}}$) is always within the interval $0 \leq e_{ff,\text{pump}} \leq 1$:

$$e_{ff,\text{pump}} = \frac{P_{\text{h,pump}}}{P_{\text{in,pump}}} \tag{2.4}$$

Figure 2.3 illustrates typical performance curves for a centrifugal pump. There are three curves, the efficiency curve has a maximum point, where the best performance occurs, called BEP (best efficiency point). It is recommended to operate the pump around this point.

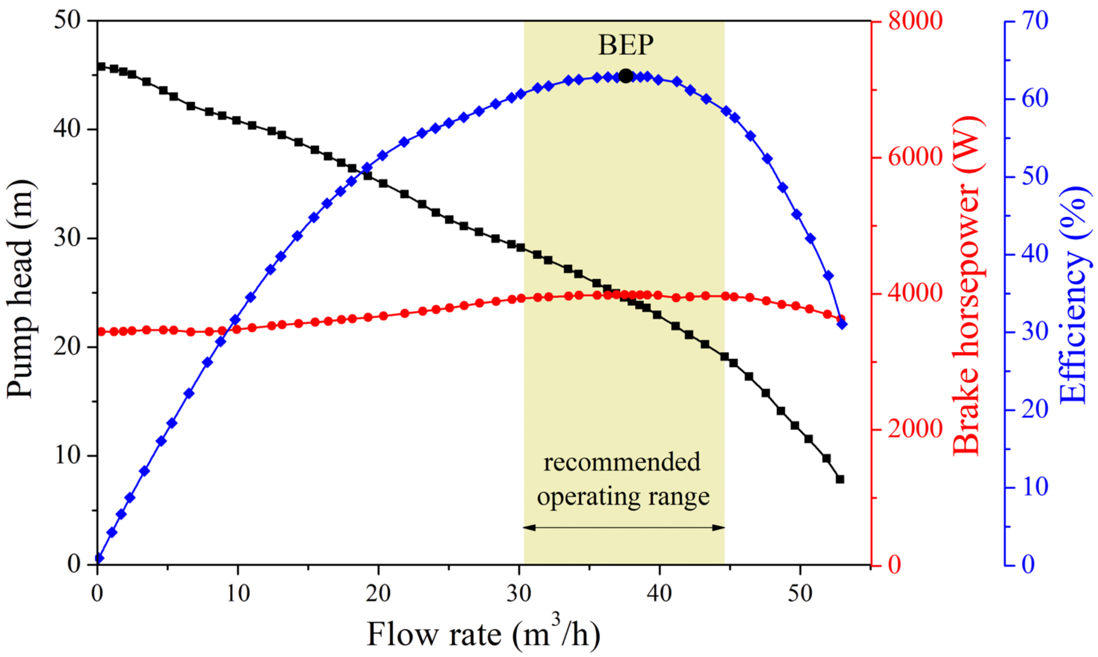

FIGURE 2.3 – Performance curves of a centrifugal pump (Perissinotto *et al.*, 2021).

2.1.3 Elementary pump theory

In centrifugal pumps, the concept of ideal flow pertains to the behavior of fluid under hypothetical operating conditions, assuming the absence of energy losses resulting from friction, viscosity, or other real-world factors. Ideal flows are employed to analyze pump behavior and can serve as a foundation for initial designs and calculations. Nevertheless, it is crucial to acknowledge that real flows, in practical scenarios, incur substantial energy losses, necessitating a more realistic consideration to engineer pumps that are efficient and dependable.

The flow velocity within the impeller of a centrifugal pump can be represented by a triangle of velocities, typically depicted at the inlet and outlet of the impeller blades, as illustrated in Fig. 2.4. This representation assumes an idealized impeller configuration, featuring an infinite number of blades with negligible thickness. Consequently, the flow is considered uni-dimensional, with its direction governed by the curvature of these blades.

As discussed in White (2015), the fluid enters the impeller at $r = r_1$ with a velocity component W_1 tangential to the blade angle β_1, and a circumferential velocity $U_1 = \Omega r_1$ corresponding to the impeller's tip velocity. The absolute inlet velocity is thus the vector sum of W_1 and U_1, represented as V_1. Similarly, the flow exits at $r = r_2$ with a component W_2 parallel to the blade angle β_2, and a tip velocity $U_2 = \Omega r_2$, resulting in the velocity V_2.

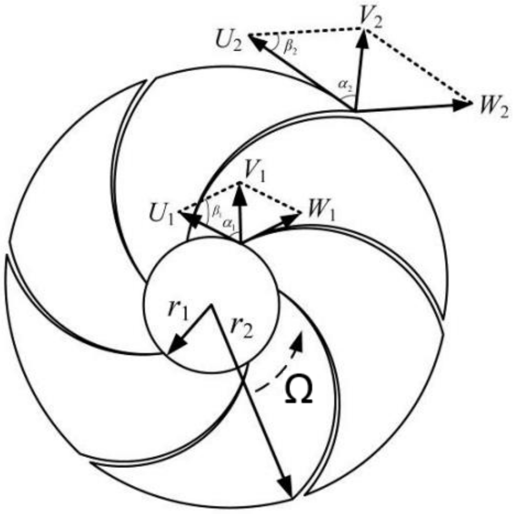

FIGURE 2.4 – Inlet and exit velocity diagrams for an idealized pump impeller (Li *et al.*, 2021).

By applying the angular momentum theorem to a turbomachine, we derive the ideal torque exerted by a one-dimensional, steady-state flow:

$$M_{\text{ideal}} = \rho Q(r_2 V_{t2} - r_1 V_{t1}) \tag{2.5}$$

where V_{t1} and V_{t2} are the absolute components of the circumferential flow velocity. The power delivered to the fluid is then given by:

$$P_{\text{h,ideal}} = \Omega M_{\text{ideal}} = \rho Q(U_2 V_{t2} - U_1 V_{t1}) \tag{2.6}$$

or

$$H_{\text{ideal}} = \frac{M_{\text{ideal}}}{\rho g Q} = \frac{1}{g}(U_2 V_{t2} - U_1 V_{t1}) \tag{2.7}$$

These equations represent Euler's turbomachine equations, demonstrating that the ideal torque, power, and head are functions solely dependent on the impeller tip velocities $U_{1,2}$ and the absolute tangential fluid velocities $V_{t1,2}$, regardless of axial velocities (if present) throughout the machine. Equations (2.6) and (2.7) describe an idealized pressure gain that cannot satisfactorily depict real fluid flow processes. In reality, the actual pump head is always lower than the ideal head due to energy losses occurring in the impeller, diffuser, inlet, and outlet of the pump as a whole (Monte Verde, 2016).

2.2 Particle image velocimetry

2.2.1 Principle

In fluid mechanics, the analytical and numerical approaches are not always able to effectively solve complex problems due to the non-uniformity of geometries and boundary conditions. In fact, most of the practical engineering situations involving fluid flows are physically and geometrically complex and hence demand the application of experimental approaches, such as techniques for flow visualization.

Nowadays, the techniques for flow visualization are especially suitable for producing images that may be used to measure fluid velocities, identify streamlines, and estimate quantities related to turbulence. These techniques provide qualitative and quantitative data for the study of flows (Perissinotto *et al.*, 2021). In the last three decades, those that use solid seeding particles to estimate the velocity fields of fluid flows have stood out (Smits, 2012). This is, in fact, the basis for the operation of the PIV method.

PIV is an advanced optical measurement technique that enables non-intrusive assessment of instantaneous velocity distributions within planar cross sections of a flow field. Its inception as a separate method can be traced back to the early 1980s (Adrian, 1984), and since then, it has witnessed remarkable progress. The rapid evolution of PIV over the last decade can be attributed to concurrent advancements in optics, pulsed lasers, computers, and digital recording and image analysis techniques. Numerous scholarly works have delved into the fundamental principles of this powerful approach to flow measurement. For instance, notable contributions have been made by researchers such as Adrian (1984), Keane & Adrian (1990), Willert & Gharib (1991), Buchhave (1992), Adrian (1997), Adrian (2005), Adrian & Westerweel (2011), and Raffel *et al.* (2018).

The general principle is to add to the flow seeding particles that move under the action of the flow structure of interest. Then, with an appropriate number of tracers, a rigorous reconstruction of the entire flow and its essential properties can be achieved.

The flow field is usually illuminated by a source of light (lighting system or laser light) to highlight the particle locations in the region of interest. The light scattered by the tracer particles is captured by a high-resolution camera (see Fig. 2.5). Through the acquisition of two images (or frames), formed by two pulses of the luminous plane in sequence (t and $t + \Delta t$), it is possible to obtain the particle displacement between two acquisitions through correlation methods. From the average particles displacement and the information of the period between the two pulses of illumination, it is possible to calculate the velocity field in a given region of the image.

Figure 2.5 presents the main components of a typical PIV system: a laser generator, a digital camera, as well as an electronic circuit responsible for synchronizing each pulse emitted by the laser with each image captured by the camera. In addition, a set of mirrors and lenses is fixed in front of the laser cavity to convert the light beam into a thin sheet that finally illuminates a plane region of the flow.

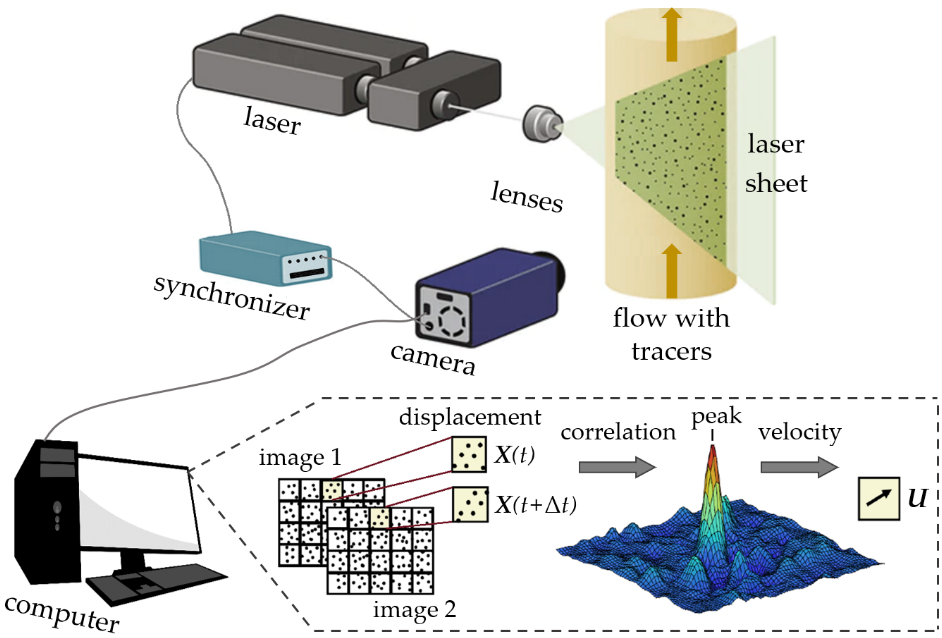

FIGURE 2.5 – Schematic illustration of a 2D-2C PIV system (Perissinotto *et al.*, 2021).

All the devices are connected to a computer that processes the images to calculate the fluid velocity vectors and other quantities dependent on their derivatives and integrals, such as gradient tensors, vorticity vectors, linear and angular deformations, and circulation integrals that reveal the presence of vortices (Perissinotto *et al.*, 2021). The procedure basically consists in dividing each pair of images into small regions, called interrogation windows, and then identifying the movement of the particles from differences in light intensity. The statistical concept of cross correlation is then used to calculate the average displacement of a group of tracers. As a result, the algorithm provides a correlation map with a peak intensity for each pair of interrogation windows. This peak intensity corresponds to a velocity vector that represents an estimated measure of the local fluid velocity. The algorithm is then repeated for other interrogation windows and other pairs of flow images as well.

In conventional PIV (Fig. 2.5), a single camera is positioned perpendicularly to the laser sheet. In this configuration, the method measures two components of the velocity vector in a two-dimensional region (2D-2C). However, for more complex flows, it is recommended to employ two or more cameras to estimate all three components of the velocity vector. In such cases, the method is referred to as stereoscopic PIV (Prasad, 2000; Wieneke, 2005), or simply stereo-PIV (2D-3C) when measurements are conducted on a thin laser plane. Alternatively, tomographic PIV (Elsinga *et al.*, 2008; Scarano, 2012), or simply tomo-PIV (3D-3C), is employed when measurements are taken within a thick laser volume. Figure 2.6 illustrates these variations of the PIV technique.

2.2.2 PIV setup

A brief description of some procedures associated with the PIV system is provided below. The emphasis is on providing generally applicable guidelines for properly setting up a PIV experiment. For a complete description of the individual components of the system, more information can be extracted from Raffel *et al.* (2018) and references therein.

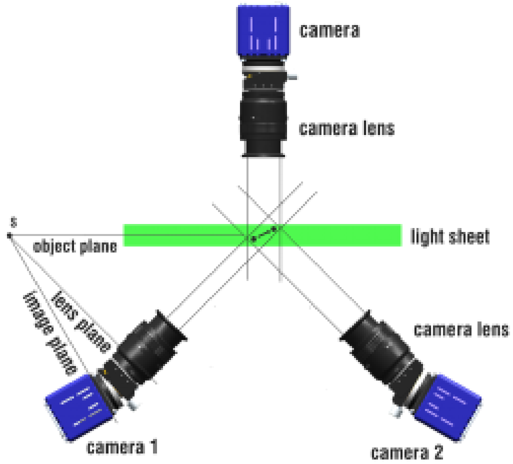

(A) stereo-PIV (2D-2C)

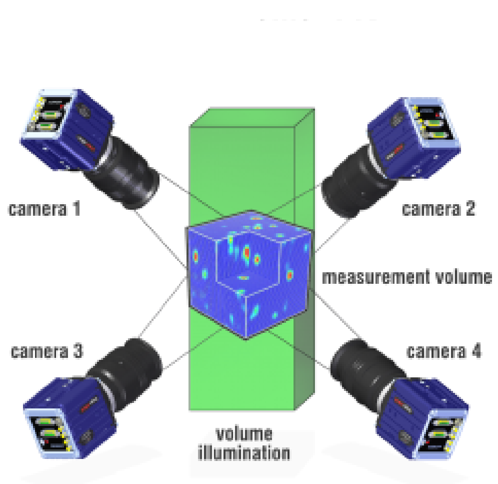

(B) tomo-PIV (3D-3C)

FIGURE 2.6 – Camera positions in stereoscopic and tomographic PIV configurations: Illustration of typical setups. Adapted from Jamil *et al.* (2021).

Seeding

Conducting a PIV experiment necessitates meticulous selection of appropriate tracers capable of accurately tracing the fluid motion and effectively scattering light to produce high-quality images. It has been previously observed that achieving a uniform and adequately concentrated flux seeding is imperative for any PIV experiment. Consequently, the ideal seeding particles should possess neutral buoyancy and be as small as possible, while still being large enough to scatter sufficient light. Therefore, the tracking of particle characteristics represents a crucial stage in a PIV experiment.

When a particle's density (ρ_p) differs from the density of the fluid (ρ), drag forces affect the particle's motion. Stokes' law can estimate the velocity reduction of a spherical particle (diameter d_p) dispersed in a fluid with viscosity μ and under constant acceleration $\boldsymbol{a}$.

$$\mathbf{U}_p - \mathbf{U} = d_p^2 \frac{(\rho_p - \rho)}{18\mu} \boldsymbol{a} \tag{2.8}$$

The velocity delay is the difference between the particle velocity ($\mathbf{U}_p$) and the fluid velocity ($\mathbf{U}$). To ensure satisfactory behavior as a tracer, this velocity slip should be minimized. The equation reveals that minimizing the difference between $\mathbf{U}_p$ and $\mathbf{U}$ occurs when the particle is small (smaller d_p), the fluid is viscous (larger μ), and their specific masses are similar ($\rho_p \approx \rho$).

For particles with diameters larger than the incident light's wavelength ($d_p > \lambda$), Mie theory governs the light scattering, which depends on various factors like refractive index ratios, particle size, shape, orientation, light polarization, and observation angle. On the other hand, when particle diameter is smaller than the wavelength ($d_p < \lambda$), Rayleigh theory predicts that the amount of scattered light varies with d_p^{-6}, making particle registration complex.

To address the issue of limited light scattering, fluorescent tracers are employed in the laser-induced fluorescence (LIF-PIV) technique. Rhodamine-doped polymeric microspheres are commonly used as fluorescent particles with Nd:YAG lasers. These particles absorb green light and emit reddish tones. To isolate the emitted waves from the fluorescent particles, an optical bandpass filter is installed in the camera, blocking the original light.

Illumination and recording

In the PIV context, the use of a pulsed Nd:YAG laser is essential. This laser emits short-duration pulses of high-energy light, ensuring that the particles in the stream are captured in non-blurred images. To achieve this, the pulsed laser beams are transformed into a two-dimensional sheet of light through the utilization of cylindrical and spherical lenses. For practical guidance on setting up the optical components, reference can be made to Stanislas & Monnier (1997).

As discussed in Sec. 2.2.1, the light scattered by illuminated particles is recorded using digital cameras equipped with light-sensitive CCD and CMOS sensors. In a concise manner, a sensor is basically a matrix with several individual elements, called pixels, which produce and store electrical charges from the absorption of incident photons of light. In the CMOS sensor, each element contains its own electronic circuit (active pixel), a characteristic that usually offers considerable advantages in comparison to the CCD sensor, including the possibility of working at high acquisition rates (Perissinotto *et al.*, 2021).

A crucial factor affecting the accuracy of PIV measurements is the size of the particle images captured in the recording plane. This size is influenced not only by the diameter of the particles (d_p) but also by the point response function of the camera lens. In the case of diffraction-limited images, the point response function (d_s) is represented by an Airy function (Olivier *et al.*, 2010), resulting in a diffraction pattern for particles with finite diameters, as shown in Adrian (1991).

$$d_s = 2.44(\mathcal{M} + 1)f^{\#}\lambda \tag{2.9}$$

The numerical aperture ($f^{\#}$) of the camera lens, defined as the ratio of its focal length (f) to the aperture diameter (D_a), along with the wavelength of laser light (λ), plays a significant role in determining the total diameter of the particle image. Neglecting lens aberrations, an estimated total diameter of the particle image (d_T) can be obtained, as described in Adrian (1991):

$$d_T = \sqrt{\mathcal{M}^2 d_p^2 + d_s^2} \tag{2.10}$$

When dealing with small magnifications ($\mathcal{M}$) that occur while measuring large areas in the flux, the size of the particle image is primarily governed by the diffraction-limited point, $d_T \approx ds$. Increasing the numerical aperture ($f^{\#}$) leads to a larger particle image diameter and focal depth, but it simultaneously results in a reduction in the intensity of light reaching the CCD or CMOS. Consequently, PIV measurements require careful optimization of the d_p, $\mathcal{M}$, and $f^{\#}$ parameters.

2.2.3 Image pre-processing

The PIV pre-processing step aims to enhance correlation signal and generate high-quality vector fields through contrast enhancement, brightness correction, and noise removal. This can be achieved using either algorithmic or hardware approaches. The pre-requisite for successful processing is the presence of a well-defined pattern with adequate contrast between particle images and back-light. Temporal and spatial filters can be employed to adjust intensity distribution and remove background lighting.

In two-phase flows, for example, the phase with a different refractive index (e.g., drops) contributes to light scattering and background illumination. Spatial filters may face challenges when interpreting moving drops as optical windows. To separate phases in images, fluorescent tracer particles and an optical high-pass filter can be utilized. Digital filters like Gaussian, RMS (root mean square), and SSM (subtract sliding minimum) can further improve contrast and remove backlighting. Moura (2017) presented comparisons between the original image of a seeding particle and the filtered versions (Fig. 2.7), in addition to a comparison of the intensity distribution of the original particle image and that pre-processed by the filters in Fig. 2.7.

As we can observe, the Gaussian filter smooths particle image shapes but may not efficiently remove background illumination (Figs. 2.7b and 2.8). The SSM filter effectively removes background illumination but can lead to high intensity differences between particle images, potentially compromising intensity distribution homogeneity and introducing correlation errors (Figs. 2.7c and 2.8). These errors can be mitigated by establishing an intensity limit. The RMS filter not only removes background lighting but also alters the shape of the intensity peak, resulting in a more flattened peak (Figs. 2.7d and 2.8). However, when corresponding particle images at different times are equally deformed, the correlation errors are low (Raffel *et al.*, 2018).

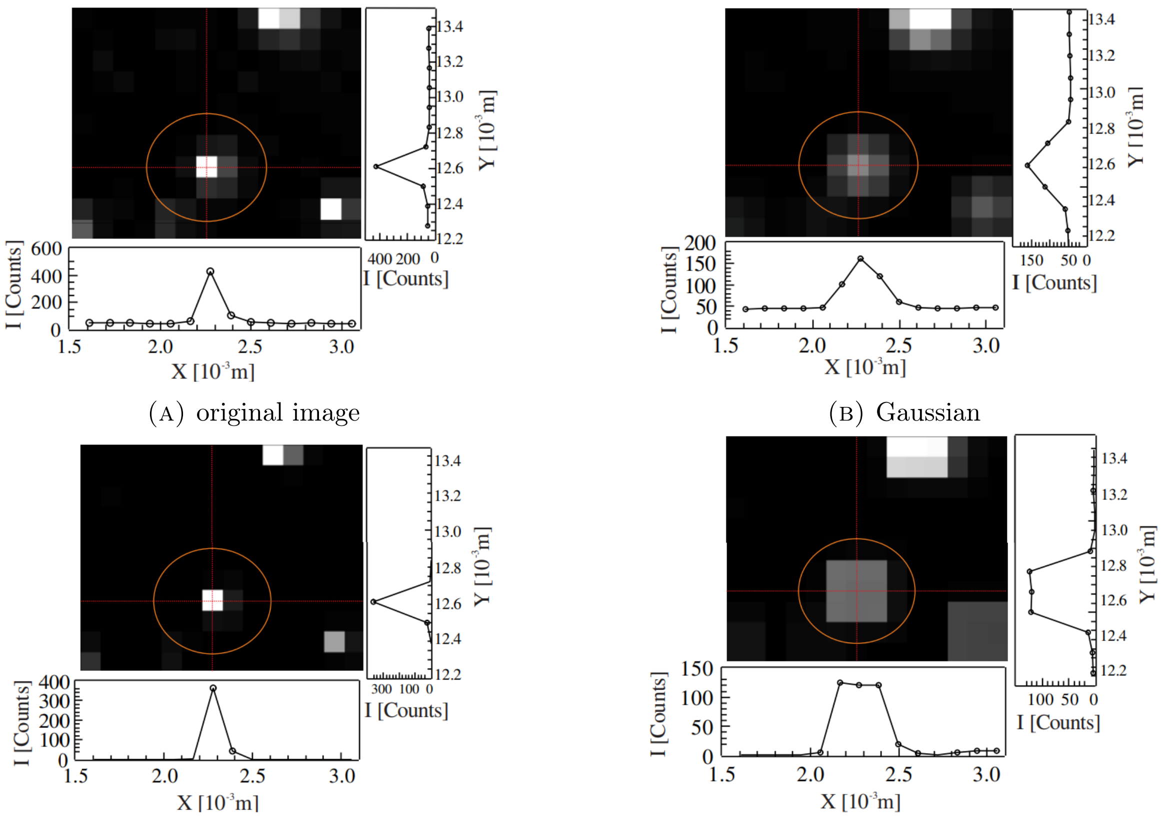

(A) original image (B) Gaussian (C) SSM (D) RMS

FIGURE 2.7 – Intensity distribution of a single seeding particle image (Moura, 2017).

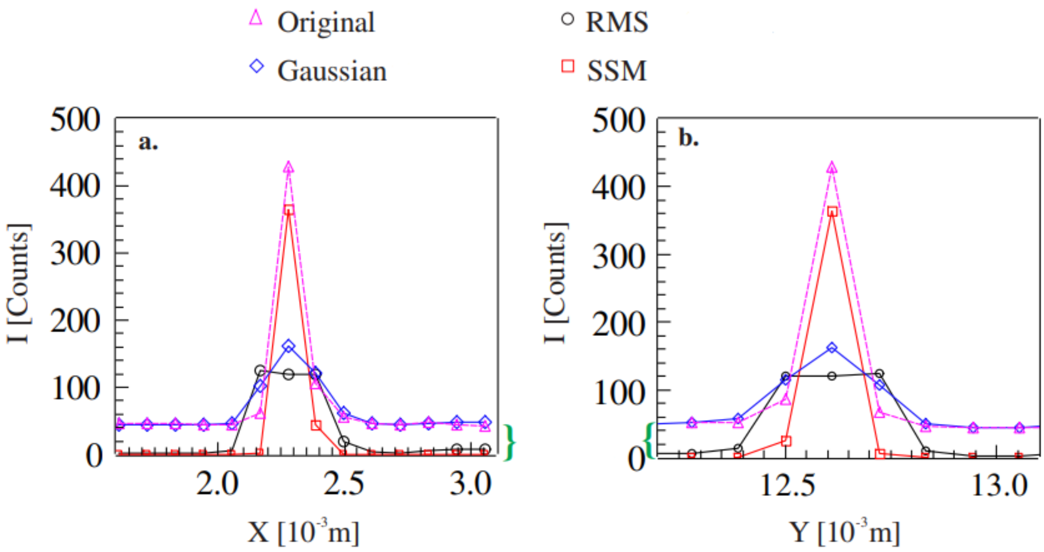

FIGURE 2.8 – Comparison of a original seeding particle image and pre-processed particle image through the filters in Fig. 2.7 (a) X-axis and (b) Y-axis (Moura, 2017).

There are also image treatments based on the normalization of gray intensities, designed to achieve uniform brightness and contrast across both highly illuminated and low-illumination particles (Westerweel, 1993; Shavit *et al.*, 2007). These methods primarily involve the adjustment of maximum and minimum intensities within image samples, thereby facilitating an overall equilibrium of light distribution across the entire image.

2.2.4 PIV processing

After the pre-processing step, the PIV images are stored in pairs which have a specific time step between acquisitions. Transforming the recorded particle image pairs to a velocity vector field first involves dividing the images in the interrogation windows. The displacement vector is obtained from the PIV cross-correlation algorithm, which returns the average motion of small groups of particles (Raffel *et al.*, 2018). The cross-correlation algorithm is a statistical pattern matching technique that tries to find the particle pattern from interrogation window $A(t)$ back in interrogation window $B(t + \Delta t)$. This statistical technique is implemented with the discrete cross-correlation function:

$$C(m, n) = \sum_{i}^{m} \sum_{j}^{n} I_1(i, j) \cdot I_2(i - m, j - n) \tag{2.11}$$

In Eq. (2.11), I_1 and I_2 denote the image intensity distribution of the first and second images, m and n the pixel offset between the two images. The location of the intensity peak in the resulting correlation matrix C gives the most probable displacement of the particles from I_1 to I_2 (Thielicke & Sonntag, 2021). There are two common approaches to solve Eq. (2.11): one approach proposes to compute the correlation matrix in the spatial domain. This approach is also called direct cross-correlation (DCC). Another approach, which is preferred due to this reduced computational cost, calculates the correlation matrix in the frequency domain (discrete Fourier transform, DFT) through the use of the fast Fourier transform (FFT).

The DCC computes the correlation matrix in the spatial domain. In a typical PIV acquisition, the images can be divided into hundreds of interrogation windows. Given the size of a square interrogation area A, a number of operations of the order of A^4 have to be computed (Keane & Adrian, 1992). Therefore, the DCC is an expensive computational technique. That is the main reason for introducing the fast Fourier transform into the cross-correlation process. The computational effort is reduced to the $O[A^2 \ln A]$, which means a considerable speed-up of the evaluation process of the cross-correlation function directly within a reasonable time-scale (Raffel *et al.*, 2018).

In the DFT approach, the local light intensity distributions contained in the interrogation windows are converted to the frequency domain to process the cross-correlation algorithm from the FFT. By multiplying the transform of the first image by the complex conjugate of the transform of the second one, the real and imaginary parts of the correlation map in the frequency domain are produced. The inverse FFT completes the operation and produces the correlation matrix C, given by Eq. (2.12):

$$C(m,n) = \Im^{-1}\{\Im[I_1(m,n)] \cdot \Im[I_2(m,n)]^*\} \tag{2.12}$$

where $\Im$ is the FFT operator of I_1 and I_2 and * represents their complex conjugate.

Figure 2.9 presents the process of correlation between two images employing an FFT.

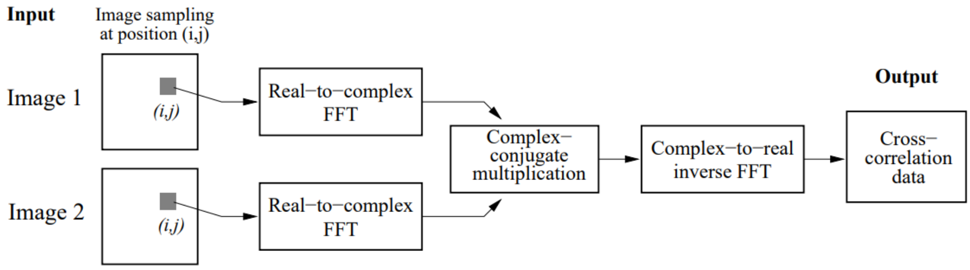

FIGURE 2.9 – Implementation of cross-correlation using FFT (Raffel *et al.*, 2018).

Significant advances in enhancing processing quality have been also made through the development of interrogation window refinement routines. Particular emphasis has been placed on the implementation of multiple pass schemes, mesh refinements, and window deformations (Hart, 2000; Wereley & Meinhart, 2001; Scarano, 2001). Nevertheless, the effectiveness of computational methods remains contingent, to some degree, on practical criteria that necessitate adherence by the system user. Additional insights into these criteria can be found in Raffel *et al.* (2018); Perissinotto (2023).

2.2.5 PIV post-processing

After establishing the most appropriate correlation algorithm, the final stage of the PIV analysis involves the application of post-processing methodologies. PIV measurements invariably encounter challenges including Gaussian background noise, outliers, and potential gaps in data. As an illustration, within Fig. 2.10, velocity fields portraying four distinct physical phenomena are exhibited. These fields encompass vectors that deviate significantly from the norm. In a broader context, an outlier within PIV data can be interpreted as an inaccurate vector embedded within the velocity field due to its lack of conformity with valid vectors. This discrepancy gives rise to incongruities that possess the capacity to not only distort the representation of velocity distribution but also exert direct influence on quantifiable parameters extracted from the instantaneous velocity field. These parameters encompass factors tied to turbulence, vorticity, and similar phenomena.

The PIV post-processing can be succinctly described as a series of three consecutive steps aimed at vector validation. These steps encompass: i) outliers identification, ii) substitution of these vectors, and iii) implementation of data smoothing techniques. While various methodologies exist in the literature for the elimination of such misleading vectors, Abrantes *et al.* (2012) emphasize several filters including those based on global mean, vector divergence, dynamic mean, median, and peak intensity. Nevertheless, more contemporary approaches for validating PIV vectors have gained prevalence and recommendation. For instance, the normalized median test introduced by Westerweel & Scarano (2005) and the weighted method (about neighboring velocities) for outlier detection within unstructured data proposed by Duncan *et al.* (2010) have become widely utilized techniques.

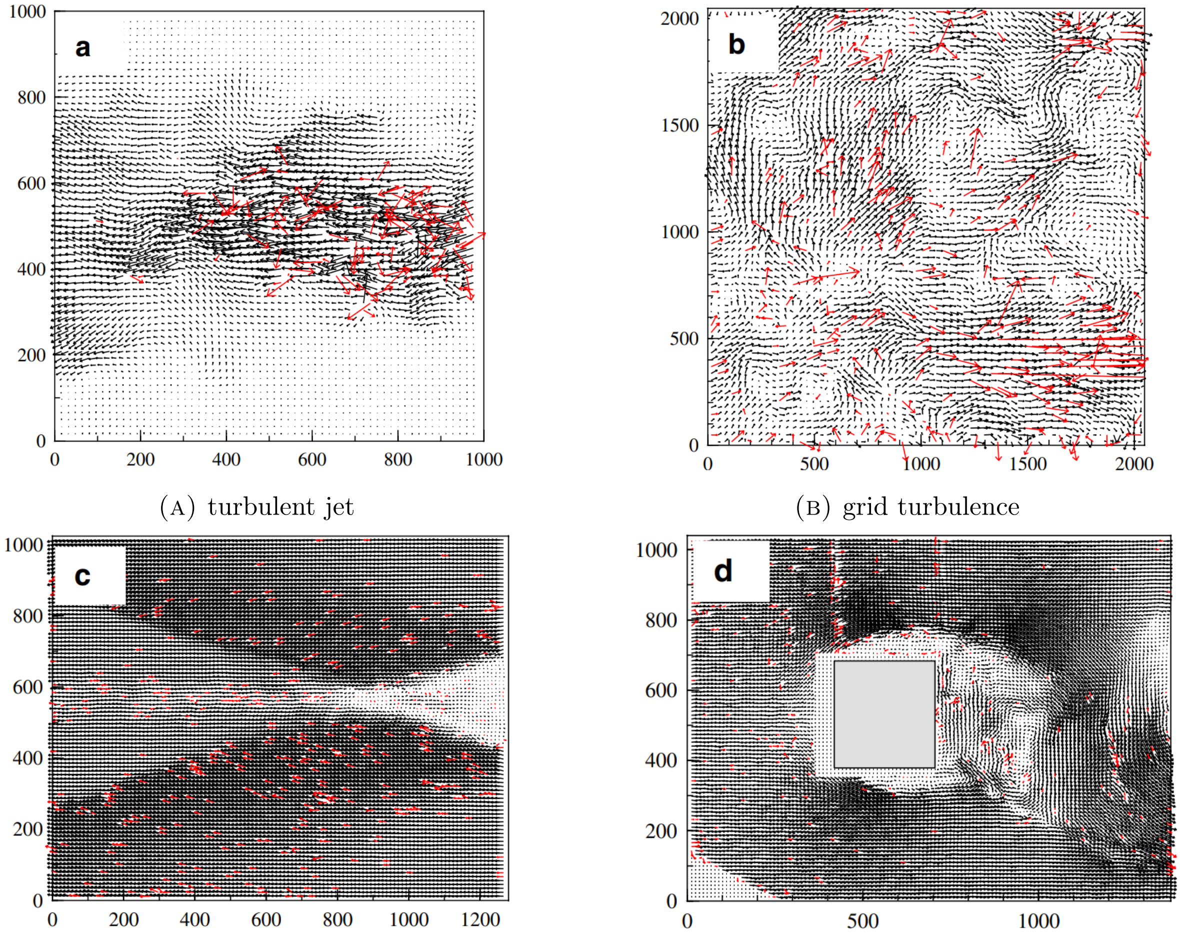

(A) turbulent jet

(B) grid turbulence

(C) supersonic (Ma=2) wake

(D) Von Kármán wake

FIGURE 2.10 – Outliers examples from the PIV data (Westerweel & Scarano, 2005).

Upon the outliers identification and elimination, flow statistics may be calculated from PIV data by ensemble averaging a large number of instantaneous velocity fields collected independently in a stochastically stationary flow. This procedure generates approximations of flow characteristics at every grid point (i, j) within the measurement plane. For example, if N denotes the total number of vector maps in an ensemble, estimations of ensemble-average flow properties can be calculated using the following equation:

$$\langle \mathbf{B}(i,j) \rangle = \frac{1}{N} \sum_{n=1}^{N} \mathbf{B}(i,j,n) \tag{2.13}$$

where $\mathbf{B}(i, j)$ represents any of the analyzed flow variables, such as velocity, vorticity, turbulence production and dissipation.

In accordance with established error metrics, which have been demonstrated to be applicable to mean PIV data as presented by Ullum *et al.* (1998), the uncertainty associated with the mean velocity stemming from N statistically independent samplings can be expressed as:

$$\epsilon_\mu = z_c \frac{s_U}{\sqrt{N}} \tag{2.14}$$

where z_c represents the confidence coefficient equal to 1.96 for a confidence interval of 95%, and s_U is the standard error on $\mathbf{U}$, as explained by Wernet (2000). With the precision of the instantaneous PIV velocity distributions established at approximately 1%, Eq. (2.14) illustrates the rapid reduction of statistical errors as the number of samplings is increased.

As previously discussed, the primary outcome provided by PIV method is the instantaneous velocity distribution of the fluid motion. Nevertheless, additional parameters derivable from these velocity distributions encompass the velocity gradient tensor, vorticity distribution, rate of viscous dissipation, turbulence production and the list goes on. In a broad sense, these quantities are ascertained through numerical computation formulas, such as finite difference techniques for differentiation and quadrature approaches for integration, as expounded in Burden *et al.* (2015).

2.3 Turbulent flows

Most flows found in nature and engineering applications are turbulent. Consequently, it is very important to understand the physical mechanisms that govern this type of phenomenon. Turbulent flows are unstable, irregular, diffusive, dissipative, random, chaotic, and contain fluctuations that are a function of time and spatial position. Among the most important characteristics of turbulent flows, it is possible to highlight the multiplicity of scales that characterize them, from the large structures to breaking up into small vortices and it dissipation, as can be seen in Fig. 2.11, in which large vortices are detached and advected by the flow dividing into smaller vortices (Tennekes & Lumley, 1972; Pope, 2000; Davidson, 2015).

FIGURE 2.11 – Axisymmetric jet directed downward (Van Dyke, 1982).

2.3.1 Turbulence equations

As already mentioned, turbulent flows are characterized by intense fluctuations (as seen in Fig. 2.12), which suggests the difficulty of obtaining a complete description of the flow field, as there is an enormous range of scales to be resolved, the smallest spatial scales being less than millimeters and the smallest time scales being milliseconds (Kundu & Cohen, 2008). However, for many of the phenomena of interest, it is sufficient to know the average value of the variables. The Reynolds decomposition (Reynolds, 1895), allows to separate an instantaneous field into its mean and the fluctuation, i.e.:

$$\mathbf{U}(\mathbf{x},t) = \langle \mathbf{U}(\mathbf{x},t) \rangle + \mathbf{u}(\mathbf{x},t) \tag{2.15}$$

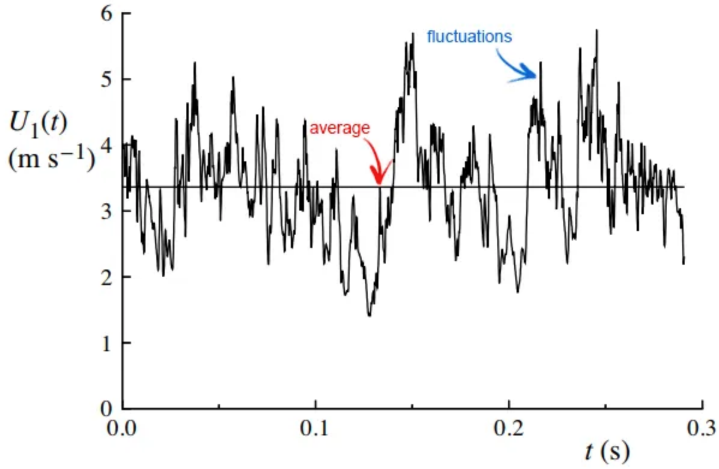

FIGURE 2.12 – Decomposition of instantaneous velocity. Adapted from Pope (2000).

where $\mathbf{U}(\mathbf{x}, t)$ is the instantaneous field, $\langle \mathbf{U}(\mathbf{x}, t)\rangle$ the mean velocity field and $\mathbf{u}(\mathbf{x}, t)$ the fluctuations. A turbulent flow instantaneously satisfies the Navier–Stokes equations. Therefore, the equations of motion for the instantaneous variables are given by:

$$\frac{\partial U_i}{\partial x_i} = 0 \tag{2.16}$$

$$\rho\left(\frac{\partial U_i}{\partial t} + U_j\frac{\partial U_i}{\partial x_j}\right) = \rho g_i - \frac{\partial p}{\partial x_i} + \mu\frac{\partial^2 U_i}{\partial x_j^2} \tag{2.17}$$

The equations satisfied by the mean-flow are obtained by substituting the Reynolds decomposition (Eq. 2.15) into the instantaneous Navier–Stokes equations (Eqs. 2.16 and 2.17) and taking the average of the equations (Pope, 2000). The equations transform as follows:

$$\frac{\partial \langle U_i\rangle}{\partial x_i} = 0 \tag{2.18}$$

$$\langle\rho\rangle\left(\frac{\partial \langle U_i\rangle}{\partial t} + \langle U_j\rangle\frac{\partial \langle U_i\rangle}{\partial x_j}\right) = \langle\rho g_i\rangle - \frac{\partial \langle p\rangle}{\partial x_i} + \mu\frac{\partial^2 \langle U_i\rangle}{\partial x_j^2} - \langle\rho\rangle\frac{\partial \langle u_i u_j\rangle}{\partial x_j} \tag{2.19}$$

Equation (2.19) when compared to instantaneous Navier–Stokes equation reveals a new term. This term is associated with the increase in resistance to deformation caused by the flow turbulence. The stress $\langle u_i u_j\rangle$ is the result of interactions between fluctuations in the flow field. This term is called turbulent stress tensor or Reynolds stress.

For an incompressible flow, the Reynolds stress term is given in matrix notation by:

$$\langle u_i u_j \rangle = \begin{pmatrix} \langle u_1^2 \rangle & \langle u_2 u_1 \rangle & \langle u_3 u_1 \rangle \\ \langle u_1 u_2 \rangle & \langle u_2^2 \rangle & \langle u_3 u_2 \rangle \\ \langle u_1 u_3 \rangle & \langle u_2 u_3 \rangle & \langle u_3^2 \rangle \end{pmatrix} \tag{2.20}$$

where the tensor trace, given by Eq. (2.20), is the turbulent kinetic energy:

$$k = \frac{1}{2} \langle u_i u_i \rangle \tag{2.21}$$

Equation (2.19) demonstrates that the average velocity components of a turbulent flow satisfy the same equations as a laminar flow, except that the laminar terms must be augmented by additional stresses provided by the Reynolds tensor. These stresses are due to turbulent fluctuations, being obtained by the mean values of the square terms of the turbulent components (Tennekes & Lumley, 1972; Panton, 2013).

A transport equation for second order moments $\langle u_i u_j \rangle$ is obtained by performing an algebraic manipulation of the average Navier-Stokes equation as presented in Tennekes & Lumley (1972):

$$\frac{\partial \langle u_i u_j \rangle}{\partial t} + \langle u_m \rangle \frac{\partial \langle u_i u_j \rangle}{\partial x_m} = -\mathcal{P}_{ij} + T_{ij} + D_{ij} - \varepsilon_{ij} \tag{2.22}$$

This equation indicates the balance of advection, production ($\mathcal{P}_{ij}$), turbulent transport (T_{ij}), viscous diffusion (D_{ij}), and dissipation (ε_{ij}) for the individual terms of the Reynolds stress tensor. According to Pope (2000) for a statistically stationary flow, the time derivative must be zero. The terms in the right-hand side are defined as:

$$\mathcal{P}_{ij} = -\langle u_i u_j \rangle \frac{\partial \langle U_i \rangle}{\partial x_j} \tag{2.23}$$

$$T_{ij} = -\frac{\partial \langle u_i u_i u_j \rangle}{\partial x_j} \tag{2.24}$$

$$D_{ij} = \nu \frac{\partial^2 \langle u_i u_j \rangle}{\partial x_j^2} \tag{2.25}$$

$$\varepsilon_{ij} = 2\nu \left\langle \frac{\partial u_i}{\partial x_j} \frac{\partial u_i}{\partial x_j} \right\rangle \tag{2.26}$$

The turbulence production term ($\mathcal{P}_{ij}$) represents the rate of creation of $\langle u_i u_j \rangle$ by the action of the mean-flow on the turbulent field. The term T_{ij} does not contribute to the global level of turbulence, serving only to redistribute energy between the normal stress components. The diffusive term (D_{ij}) promotes a spatial redistribution of turbulent stress and the dissipative term (ε_{ij}) represents the rate of destruction of $\langle u_i u_j \rangle$ by the viscous effects. This term indicates that the energy continuously withdrawn from the mean-flow by the turbulent field through the term $\mathcal{P}_{ij}$ will be destroyed, preventing an unlimited growth of $\langle u_i u_j \rangle$ (Tennekes & Lumley, 1972; Pope, 2000).

2.3.2 Estimation of the dissipation rate

The turbulent dissipation rate is a key parameter in centrifugal pump impeller studies, and its local values may significantly influence the performance of these devices. In recent research, experimental techniques with high temporal resolution (e.g., hot-wire anemometry and laser Doppler velocimetry - LDV) have been employed to calculate turbulent characteristics, including the turbulent dissipation rate. Following Taylor's frozen flow hypothesis (Hinze, 1994), velocities of temporal fluctuations can be transformed into spatial fluctuations, and the turbulent dissipation rate can be easily calculated, as the spatial velocity gradients are readily available. However, these methods cannot immediately provide the global distribution of the dissipation rate over a large flow region.

Contrary to single-point experimental techniques, the PIV technique can provide instantaneous multi-dimensional (2D or 3D) flow fields. At first glance, the PIV technique seems more suitable for examining the dissipation rate distribution. However, the PIV measured velocity fields have limited spatial resolution, constrained by a combined effect of the tracer particles and the camera sensor size:

$$L_r = \frac{L_{IW}}{L_C} L_v \tag{2.27}$$

In this equation, L_r is the smallest resolved length scale with the PIV system, L_v the length scale of the viewing area in the flow, and L_{IW} and L_C the dimensions of the interrogation window (IW) and CCD or CMOS array, respectively (usually in number of pixels). Clearly, for a given PIV technique, the decrease of L_r, requires the reduction of the viewing area size L_v. For a typical PIV system where IW = 32 pixels and CCD/CMOS = 1024 pixels, and a flow at Re = 10^6 based on the integral length scale of 10 cm, the viewing area dimension of the PIV measurement is only 0.1 mm in order to resolve the Kolmogorov scale (3 μm). This field of view is usually too small to provide useful full field information for engineering process applications. The alternative is to sacrifice spatial resolution.

It is imperative to underscore that velocities obtained through PIV measurements possess distinct characteristics compared to velocities obtained by single-point velocimetry techniques. As a result of the correlation technique (which generally forms the basis of PIV data reduction), each velocity vector is a result of a spatial average of the velocity field in one IW. This implies a form of low-pass filtering. It is paramount to exercise caution when deriving statistical parameters like time-averaged velocity, turbulent kinetic energy, and Reynolds stresses from PIV data. The real, point-wise velocity can be expressed in relation to the PIV-derived (spatially averaged) velocity as follows:

$$U_i = \langle U_i \rangle - \zeta \langle U_i \rangle + \frac{1}{2!}\zeta^2 \langle U_i \rangle - \frac{1}{3!}\zeta^3 \langle U_i \rangle + \cdots \tag{2.28}$$

where $\zeta \langle U_i \rangle = (b_1 \partial^2 x_1 + b_2 \partial^2 x_2 + b_3 \partial^2 x_3) \langle U_i \rangle$, $\langle U_i \rangle$ is the PIV resolved velocity, and b_1, b_2 and b_3 are constants related to the low-pass filter bandwidths for each direction. For a uniform filter, the constants are defined as:

$$b_i = \frac{\Delta_i^2}{8}, \quad i = 1, 2, 3 \tag{2.29}$$

where Δ_i is the filter width along the i-th axis. For an isotropic filter, filter widths along all three axes are the same, denoted as Δ. Therefore, Eq. (2.28) can be rewritten as:

$$U_i = \langle U_i \rangle - \frac{\Delta^2}{8} L^2 \langle \nabla_i \rangle + \frac{\Delta^4}{1024} \nabla^4 \langle U_i \rangle + \cdots \tag{2.30}$$

Based on this dimension analysis the second term in Eq. (2.30) scales like Δ^2/l^2, where l is the local scale of integral length. Therefore, the velocity (U_i) can be approximated by measuring PIV $\langle U_i \rangle$ when $\Delta << l$. Hence, when the IW size is much smaller than the local integral scale of the flow, Reynolds-averaged statistical quantities can be approximated from PIV data.

In order to obtain dissipation rate with PIV technique, relationships based on isotropy assumptions were proposed in the literature. Among these relationships, Sheng *et al.* (2000) suggests using "large-eddy" ideas from the large eddy simulation (LES). Through an analysis of the interplay between production and dissipation in relation to wave number (as depicted in Fig. 2.13), it can be shown that the turbulent kinetic energy is mainly generated at the integral scale, and then the same amount of energy is dissipated near the Kolmogorov scale. In between, lies a substantial expanse termed the inertial sub-range, where turbulent kinetic energy remains unaltered. Within this spectrum, the central role of turbulent structures becomes apparent – facilitating the seamless transference of energy from large-scale to small-scale structures without any alteration. Consequently, in instances where sub-integral scales attain a state of dynamic equilibrium, the flux of turbulent kinetic energy traversing the inertial sub-range corresponds precisely to the rate of turbulence dissipation (Ducci & Yianneskis, 2005). Thus, the large-eddy PIV method proposed by Sheng *et al.* (2000) does not require the velocity field to be resolved down to the Kolmogorov scale.

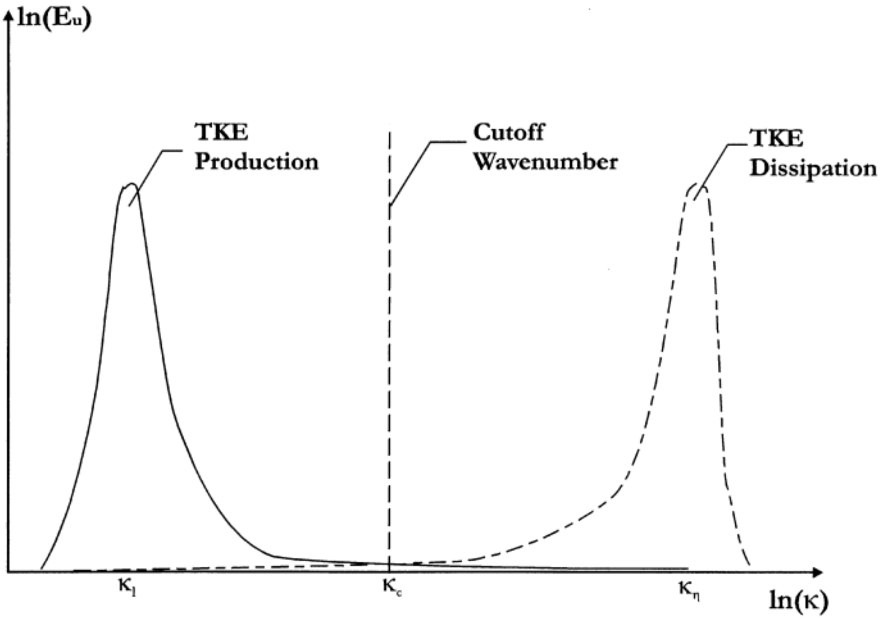

FIGURE 2.13 – Schematic model of production and dissipation of turbulent kinetic energy (Sheng *et al.*, 2000).

Based on this premise, Eq. (2.26), which models the kinetic energy transported to small scales from the resolved scales, will be equal to the turbulent kinetic energy dissipated on the smallest scales. Therefore, the turbulence dissipation rate can be approximated by calculating the Reynolds-averaged SGS (sub-grid scale) dissipation rate:

$$\varepsilon_{ij} \approx \langle \varepsilon_{SGS} \rangle = -2 \left\langle \tau_{ij} \bar{S}_{ij} \right\rangle \tag{2.31}$$

where $\bar{S}_{ij}$ is the strain rate tensor defined by:

$$\bar{S}_{ij} = \frac{1}{2} \left(\frac{\partial \langle U_j \rangle}{\partial x_i} + \frac{\partial \langle U_i \rangle}{\partial x_j} \right) \tag{2.32}$$

Using the Smagorinsky sub-grid model (Smagorinsky, 1963) it is possible to model the stress tensor (τ_{ij}) shown in Eq. (2.31) as:

$$\tau_{ij} = -C_s^2 \Delta^2 |\bar{S}| \bar{S}_{ij} \tag{2.33}$$

where $C_s = 0.17$ is the Smagorinsky constant, $\Delta = 3$ mm is the average filter width (equal to the interrogation window size), and $\left(C_S^2 \Delta^2 |\bar{S}|\right)$ is the eddy viscosity, where $|\bar{S}|$ is the filtered rate of strain $|\bar{S}| = \left(2\bar{S}_{ij}\bar{S}_{ij}\right)^{1/2}$. To estimate the dissipation rate from PIV measurements using the large-eddy PIV method, it is necessary to assess whether the dynamic equilibrium premise is valid. First, we check if the higher order terms in Eq. (2.30) can be dropped so that the statistical quantities can be calculated from the resolved scale velocity, $\langle U_i \rangle$, using the Reynolds decomposition. Next, the Kolmogorov length scale (η) must be $<< \Delta$ so that we have dynamic equilibrium (Sheng *et al.*, 2000).

Turbulent dissipation rate can be calculated from filtered gradients obtained from 2D-PIV:

$$\begin{aligned} \langle \varepsilon_{SGS} \rangle = (C_s \Delta)^2 \Bigg\{ & 2 \left\langle \left(\frac{\partial U_1}{\partial x_1} \right)^2 \right\rangle + \left\langle \left(\frac{\partial U_2}{\partial x_1} \right)^2 \right\rangle + \left\langle \left(\frac{\partial U_1}{\partial x_2} \right)^2 \right\rangle + 2 \left\langle \left(\frac{\partial U_2}{\partial x_2} \right)^2 \right\rangle + \\ & 2 \left[\left\langle \left(\frac{\partial U_1}{\partial x_2} \right) \left(\frac{\partial U_2}{\partial x_1} \right) \right\rangle \right] \Bigg\}^{3/2} \end{aligned} \tag{2.34}$$

Based on this approach, Sheng *et al.* (2000) employed a large-eddy PIV method to approximate the dissipation of energy at scales below the resolution of the measurements in a stirred tank. The turbulent dissipation rate was estimated from energy flux between the resolved and the sub-grid scales under dynamic equilibrium assumption. The Smagorinsky SGS (sub-grid scale) model (Versteeg & Malalasekera, 2007) was used to estimate the amount of dissipation rate contained in the unresolved scales and at least 70% of the true dissipation was captured. Gabriele *et al.* (2011) used large-eddy PIV to study the effect of particle loading on the modulation of turbulent dissipation rate in a stirred tank. The authors came to the conclusion that large Stokes number particles can suppress turbulence.

A study on the influence of the spatial resolution of PIV measurements on the estimated values of the rate of turbulent kinetic energy dissipation was carried out by Delafosse *et al.* (2011). In this study, a total of 12 spatial resolutions were tested. The authors verified that if the spatial resolution is divided by a factor 2, the dissipation rate increases by 220%. For the smallest spatial resolution value used by the authors, the maximum dissipation rate estimated is 50 times higher than the mean overall rate. Ertürk *et al.* (2013) performed PIV measurements on an external gear pump to also assess the influence of spatial resolution on dissipation rate. Results showed that the spatial resolution is a critical factor in the accuracy of the measurements in the dissipation rate estimations. The optimal results were achieved when the spatial resolution is neither too large (by the sampling phenomenon) nor too small (noise in the measurement data).

Comparisons using different methods to estimate the viscous dissipation rate in turbulent flows were also performed over the years. Gabriele *et al.* (2009) studied the local specific energy dissipation rates in a stirred tank with up- or down-pumping pitched blade turbine with PIV. Three methodologies, direct calculation from fluctuating velocity gradients, dimensional analysis and Smagorinsky closure method to model unresolved length scales, were compared to estimate the local dissipation rate of specific energy. It was found that values from direct calculation method gave 20% of the total value whilst the dimensional analysis and Smagorinsky model methods overestimated it respectively by a factor of 5 and 2. Hoque *et al.* (2015) also compared different methods of estimating energy dissipation rate. The method of direct computation from fluctuating velocity gradients was found to underpredict dissipation significantly due to the absence of spatial resolution of velocity gradient. To conclude, according to Hoque *et al.* (2015) spatial resolution is a critical factor in the accuracy of the direct calculation of dissipation rate.

2.3.3 Proper orthogonal decomposition

The turbulent flow field in the channels of a centrifugal pump impeller is usually complex, containing eddy motions across a wide range of time and length scales. Identifying coherent structures and their dynamic behavior in this context can be a challenging task. Therefore, modal decomposition techniques can be used to enhance the understanding of turbulence and coherent structures under rotating conditions.

Proper orthogonal decomposition (POD) offers a method for performing spatio-temporal analysis of turbulent flow structures, where turbulence structures are ranked by their energy content. The large-scale flow structures with higher energy content can reveal the main characteristics of turbulent flow. The main idea is to construct a spatial matrix of the velocity field and find its maximized projection onto an orthogonal basis.

In 1967, Lumley (1967) introduced the POD method to turbulence analysis for the first time, calling it the direct POD method. Since then, the analysis of coherent structures using POD has attracted significant interest in turbulence research. However, when dealing with turbulent flow rich in information, direct POD increases the size of the spatial matrix, making it more challenging to solve directly.

Therefore, Sirovich (1987) proposed the snapshot POD method, which is more convenient for dealing with complex flow fields using POD. The term snapshot in modal analysis refers to flow field data collected at a single instant in time. Before running POD on the snapshot data, each flow field dataset needs to be formatted into a column vector of the matrix $m \times n$, called the snapshot matrix (Taira *et al.*, 2017, 2020). For the fluctuation vector field (Eq. 2.15), we have:

$$\mathbf{u} = \begin{pmatrix} u_{11} & \dots & u_{1n} \\ u_{21} & \dots & u_{2n} \\ \vdots & & \vdots \\ u_{m1} & \dots & u_{mn} \end{pmatrix} \tag{2.35}$$

The idea of the POD method is to decompose $\mathbf{u}$ into a set of deterministic spatial functions $\phi_k(\mathbf{x})$ modulated by random time coefficients $a_k(t)$ using the Karhunen–Loeve expansion so that:

$$\mathbf{u}(\mathbf{x},t) = \sum_{k=1}^{N} \phi_k(\mathbf{x}) a_k(t) \tag{2.36}$$

As mentioned in Weiss (2019), Eq. (2.36) is essentially symmetric in t and $\mathbf{x}$, since mathematically there is no fundamental difference between the temporal variable t and the spatial variable $\mathbf{x}$. Therefore, we can interpret it as a decomposition involving deterministic temporal modes with random spatial coefficients. In other words, swapping t and $\mathbf{x}$ is mathematically valid. This method is called snapshot POD (Sirovich, 1987). The covariance matrix is defined as follows:

$$\mathbf{C} = \mathbf{u}\mathbf{u}^{\dagger} \tag{2.37}$$

In the snapshot POD method, the covariance matrix (Eq. 2.37) is an $m \times m$ matrix, where m represents the total number of velocity fields acquired using the PIV technique, as described in Sec. 3.3. In the direct POD method, the covariance matrix is decomposed into an $n \times n$ matrix, where $n = N_x \times N_y$ represents the number of spatial velocity points measured in each field.

The optimized basis of the dynamic system is given by the set of eigenvectors of the covariance matrix $\mathbf{C}$. In a POD analysis, the eigenvalues of matrix $\mathbf{C}$ are ordered from largest to smallest, so that the first eigenvector corresponds to the largest eigenvalue and so on. This ordering is equivalent to ranking the modes based on their contribution to the total turbulent kinetic energy (Weiss, 2019). In this approach, the matrix $\mathbf{C}$ is constructed by averaging in space, unlike Lumley's direct POD method, which averages in time. The eigenvectors ($\boldsymbol{A}$) and eigenvalues ($\boldsymbol{\Lambda}$) of $\mathbf{C}$ are computed numerically as follows:

$$\mathbf{A}\boldsymbol{\Lambda} = \mathrm{eig}(\mathbf{C}) \tag{2.38}$$

To obtain the spatial coefficients, the instantaneous data are projected onto temporal modes, as described by Eq. (2.39). The transposition of $\mathbf{u}$ is necessary both for dimensional consistency and because now only m modes are present instead of n.

$$\boldsymbol{\Phi} = \mathbf{u}^{\dagger}\boldsymbol{A} \tag{2.39}$$

The matrix $\mathbf{\Phi}$ then contains m spatial coefficients (equivalent to the spatial modes of the direct method), ordered from the "strongest" to the "weakest". The original instantaneous matrix $\mathbf{u}$ can be reconstructed from the spatial coefficients and temporal modes obtained.

$$\mathbf{\Phi} = \mathbf{u}^{\dagger}\boldsymbol{A} \Rightarrow \mathbf{u}^{\dagger} = \mathbf{\Phi}\boldsymbol{A}^{-1} = \mathbf{\Phi}\boldsymbol{A}^{\dagger} \Rightarrow \mathbf{u} = \boldsymbol{A}\mathbf{\Phi}^{\dagger} \tag{2.40}$$

or

$$\begin{pmatrix} u_{11} & \dots & u_{1n} \\ u_{21} & \dots & u_{2n} \\ \vdots & & \vdots \\ u_{m1} & \dots & u_{mn} \end{pmatrix} = \begin{pmatrix} a_{1k} \\ a_{2k} \\ \vdots \\ a_{mk} \end{pmatrix} \begin{pmatrix} \phi_{1k} & \dots & \phi_{nk} \end{pmatrix} \tag{2.41}$$

where the original snapshot matrix $\mathbf{u}$ is expressed as the sum of the contributions of the m modes:

$$\begin{pmatrix} \tilde{u}^k_{11} & \dots & \tilde{u}^k_{1n} \\ \tilde{u}^k_{21} & \dots & \tilde{u}^k_{2n} \\ \vdots & \vdots & \\ \tilde{u}^k_{m1} & \dots & \tilde{u}^k_{mn} \end{pmatrix} = \begin{pmatrix} a_{1k} \\ a_{2k} \\ \vdots \\ a_{mk} \end{pmatrix} \begin{pmatrix} \phi_{1k} & \dots & \phi_{nk} \end{pmatrix} = \tilde{\mathbf{u}}^k \tag{2.42}$$

so that:

$$\mathbf{u} = \sum_{k=1}^{m} \tilde{\mathbf{u}}^k \tag{2.43}$$

As the number n of spatial measurement points is greater than the number m of snapshots ($n > m$), the snapshot POD method is faster computationally than the direct method proposed by Lumley (1967). This means that the covariance matrix $\mathbf{C}$ is smaller and easier to store, and the corresponding eigenvalue problem is faster to solve. The POD algorithm used in this work was based on Weiss (2019) and is summarized in `algorithm` 1.

Another way to calculate the spatial modes of the POD is by using the singular value decomposition (SVD) of the covariance matrix $\mathbf{C}$, as shown below:

$$\mathbf{C} = \mathbf{u}\boldsymbol{\lambda}\boldsymbol{V}^{*} \tag{2.44}$$

In the context of the singular value decomposition of $\mathbf{C}$, $\boldsymbol{V}^*$ is the Hermitian of $\mathbf{C}$, representing the temporal dynamics of $\mathbf{C}$, and $\boldsymbol{\lambda}$ denotes the singular values. More information on the application of SVD in POD analysis and its connection to eigenvalue problems can be found in Golub & Van Loan (2013); Weiss (2019).

The POD method has received increasing attention for evaluating turbulent flows. After Lumley (1967) successfully applied the POD method on the study of turbulence, it remained one of the most widely used techniques and evolved in multiple forms (Sirovich, 1987; Christensen *et al.*, 1999; Willcox, 2006; Ilak & Rowley, 2008; Towne *et al.*, 2018). Ma & Karniadakis (2002), Liberge & Hamdouni (2010) and El-Adawy *et al.* (2018) investigated flow in cylinders, a classic fluid mechanics problem, demonstrating that the POD technique could precisely describe its characteristics. POD was also applied to analyses of engine (Fogleman *et al.*, 2004; Semlitsch *et al.*, 2014), compressor (Semlitsch & Mihăescu, 2016) and jet flows (Gordeyev & Thomas, 2000, 2002; Vernet *et al.*, 2009; Semeraro *et al.*, 2012).

Nevertheless, few studies regarding the use of the POD in centrifugal pumps have been developed so far. Zhang *et al.* (2017) used the method to improve the accuracy and reduce the calculation cost for the inverse problem of a centrifugal pump impeller. Guo *et al.* (2019) analyzed the interrelations among impeller blade geometry, flow field fluctuation intensity and impeller-induced hydrodynamic noise of centrifugal pump. Zhang *et al.* (2021) carried out a research, using a detached eddy simulation technique, on the flow characteristics and relationship between the hydraulic performance and the energy distribution of the internal flow structure in single-stage vertical marine centrifugal pumps.

In addition to the aforementioned studies using CFD techniques, TR-PIV measurements have also been employed for POD analyses in centrifugal pumps. In this context, Chen *et al.* (2022b) performed TR-PIV measurements to analyze the unsteady flow field in a centrifugal pump. The results indicated that the main flow structures are reflected by the first modes of the flow field and that jet-wake structures and stall vortex cells are associated with the first two POD modes.

Furthermore, Shaofei *et al.* (2023) conducted a comparative analysis of the POD and SPOD (spectral proper orthogonal decomposition) methods to investigate the unstable characteristics of the velocity field around the tongue of a volute in a centrifugal fan with forward-curved blades. The authors concluded that both POD and SPOD analyses reveal two types of instabilities in the flow field within the volute: large-scale fluctuations at the rotational frequency and its higher-order harmonics in the main exit flow, and jet-wake structures at the blade passing frequency in the cut-off clearance region. Additionally, the SPOD analysis identified a third type of disturbance, characterized by strip-like velocity structures at intermediate frequencies.

Algorithm 1 snapshot POD for planar velocity field

Input: Planar velocity field snapshots $\{\mathbf{U}_1, \mathbf{U}_2, \ldots, \mathbf{U}_N\}$
Output: POD modes and corresponding coefficients
Step 1: Data preparation
for $i = 1$ to N **do**
    Extract velocity fluctuations snapshot: $\mathbf{u}_i$
    Reshape $\mathbf{u}_i$ into a column vector $\mathbf{u}_i = (u_i, v_i)$
end for
Step 2: Assemble snapshot matrix
Construct the snapshot matrix $\mathbf{S}$ from reshaped snapshots
Step 3: Compute covariance matrix
Calculate the covariance matrix $\mathbf{C} = \frac{1}{m-1}\mathbf{u}\mathbf{u}^{\dagger}$
Step 4: Solve eigenvalue problem
Perform eigenvalue decomposition on $\mathbf{C}$: $\mathbf{A}\boldsymbol{\Lambda} = \mathrm{eig}(\mathbf{C})$
Step 5: Sort eigenvalues and eigenvectors
Sort eigenvalues and corresponding eigenvectors in descending order
Step 6: Extract POD modes
for $j = 1$ to m **do** ▷ Select number of modes m
    Extract POD mode: $\mathbf{A}_j$ (column of $\mathbf{A}$)
end for
Step 7: Compute POD coefficients
for $i = 1$ to N **do**
    Project each snapshot onto POD modes to compute coefficients
end for
Return: POD modes and coefficients

2.4 Single-phase flows in centrifugal pumps

As illustrated in Fig. 2.14 and unlike the theory presented in Sec. 2.1.3, single-phase flows in centrifugal pumps may be very complex. A well-behaved flow is generally observed when the pump operates at the flow rate that corresponds to BEP. However, in conditions away from the BEP, the boundary layers detach from the solid walls and consequently favor the formation of distorted velocity profiles in the impellers, with presence of jets, wakes, and re-circulation zones. Besides, the flow experiences a high turbulence which may promote the formation of vortices. The presence of vortices in an impeller influences the velocity fields and increases the energy losses due to the turbulent dissipation.

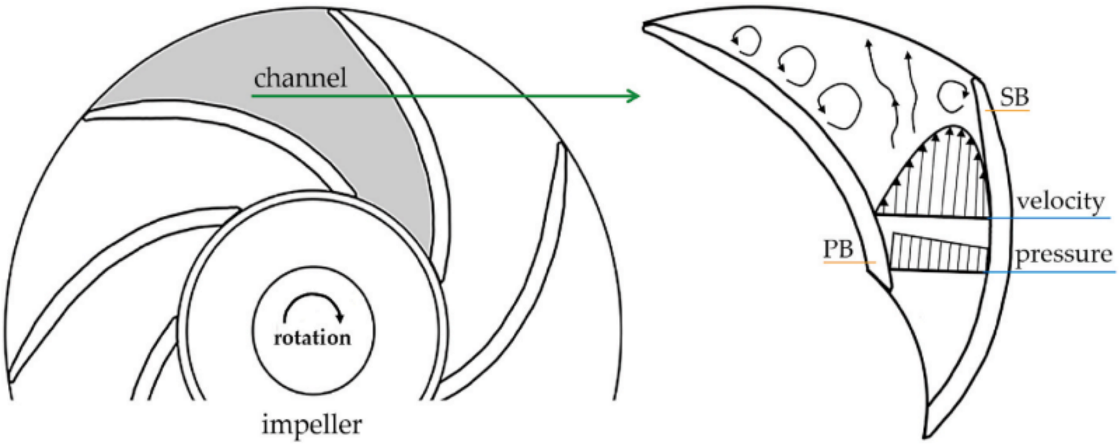

Figure 2.14 – Illustrative drawing of pressure and velocity profiles in a single channel of an impeller. The initials PB and SB indicate the pressure blade and suction blade, respectively (Perissinotto *et al.*, 2021).

Another important mechanism of energy dissipation is associated with the friction between the fluid flow and the solid surfaces. The energy losses due to friction, which generally increase with the square of flow rate, may depend directly either on the Reynolds number and/or on the roughness of the solid walls that compose the impeller channels. Therefore, energy losses may also occur when the centrifugal pump works with viscous fluids, a situation that causes a relevant degradation to its performance and efficiency (Gülich, 2008).

One way to assess the characteristics of the flow fields in a centrifugal pump impeller is through the application of optical techniques. Flow visualization investigations, mainly using PIV, were carried out over the years and they usually focused on flow features. Paone *et al.* (1989) were the pioneers to use PIV to investigate the flow in a centrifugal pump. The authors determined the relative velocity and vorticity fields in a pump diffuser. This research has been expanded by Dong *et al.* (1992a,b), who estimated momentum and energy fluxes, turbulent stresses, and turbulence production in a pump volute.

Years later, Sinha & Katz (2000) conducted experiments to investigate the flow in the gap between a pump impeller and diffuser. The authors identified the formation of turbulent structures, such as jets and wakes related to velocity fluctuations. Furthermore, the authors concluded that the rotating impeller of a centrifugal pump may promote the occurrence of hydrodynamic instabilities which affect the structure of the boundary layers in the blade walls, occasionally causing the separation of the flow.

The visualization of single-phase flows in rotating impellers was then explored by Pedersen *et al.* (2003), who carried out experiments using LDV and PIV methods in a transparent centrifugal pump to investigate the unsteady flow structures and turbulence. In a general way, such results achieved with LDV and PIV were quite similar, but the PIV method presented two advantages over LDV, which are a considerably reduced run time and an additional ability to identify instantaneous spatial flow structures. Hence, the authors concluded that the PIV technique is generally efficient in providing reliable and detailed velocity data inside full impeller channels, especially when fluorescent particles are used as tracers. In addition, they identified that at the lowest flow rates, intense instabilities arose in the diffuser and then spread to the impeller, leading to the prevalence of unsteady flow patterns.

Krause *et al.* (2005) and Zhang *et al.* (2018) characterized the evolution of a time-dependent water flow field, by using a time-resolved PIV system. The authors obtained velocities and streamlines which revealed the formation and propagation of vortices in a radial impeller (Krause *et al.*, 2005) and around the volute tongue region (Zhang *et al.*, 2018). A time-resolved approach was also adopted by Mittag & Gabi (2016) to study a mineral oil flow in the intake and impeller of a transparent centrifugal pump. The main advantage of using mineral oils in transparent pumps is basically the refractive index, which is very similar in both the oil and the acrylic material used in the pump manufacture.

In more recent years, Keller *et al.* (2014) executed one of the most extensive investigations on single-phase flows in pumps. The authors noted that for the flow rate corresponding to the BEP, an intense positive vorticity sheet was identified in the impeller suction blade as a consequence of velocity gradients. Besides, a negative vorticity sheet and an intense turbulent kinetic energy production zone were detected in the blade trailing edge.

Apart from the aforementioned studies, substantial focus has been dedicated to the visualization of internal flow within centrifugal pumps, aiming to validate the impact of flow patterns on hydraulic efficiency. Wang *et al.* (2019) carried out an analysis on the variation of vortex motion as a function of flow rate, also addressing the relationship between vorticity and pump head. Results showed that, at low flow rates, the channel passages are gradually occupied by vortices generated by flow separation until the complete blockage is reached.

Li *et al.* (2020a,b) quantitatively studied the influence of internal flow patterns on the hydraulic performance and energy conversion characteristics of a low specific speed centrifugal pump. The authors identified the formation of a clockwise vortex on the suction side and a counterclockwise vortex on the pressure side of each blade, in different channels of the impeller, as flow rate decreased. Furthermore, they concluded that the counterclockwise vortex is a source of energy losses, while the clockwise vortex positively affects the pump head. Analogously, Chen *et al.* (2022a) performed PIV experiments to describe the distribution of flow field losses in the impeller of a centrifugal pump. Results suggested that the distribution of pressure head increment is affected mainly by the flow field in the impeller inlet, while the maximum value region of the velocity increment along the radial direction is located downstream on the suction side of the blade and in the center of the unstable region on the pressure side of the blade. The authors concluded that these distributions are a consequence of the local increase in the absolute velocity of the flow field caused by the vortex motion.

In their latest experimental campaign, Perissinotto *et al.* (2023, 2024b) conducted PIV experiments on a centrifugal pump to gain insights into the relationship between flow behavior at various axial positions and pump performance. These studies shed light on the idea that, for two identical flow rates relative to the BEP, the morphology of the flow field in the impeller tends to be similar, regardless of rotational speed and absolute flow rate. As a consequence of this data, Perissinotto *et al.* (2024a) proposed an analytical model to represent the head produced by a radial impeller based on PIV data. The model reiterates that the head is influenced by energy losses due to recirculation, shock/impact, and internal friction.

Investigations to characterize the irreversible energy loss due to cavitation flow in centrifugal pumps have also been carried out recently. Jia *et al.* (2023) analyzed the distributions of pressure, velocity, bubble volume, vortex structure, and entropy generation across different degrees of cavitation and obtained internal flow characteristics and flow loss patterns. Computational fluid dynamics (CFD) together with the entropy production theory were then used by Wang *et al.* (2023) to study the relationship between irreversible flow losses and flow field details in a cavitation flow. Results showed that entropy production in the impeller is consistent with energy loss. In another recent work, Chen *et al.* (2023) used large eddy simulation (LES) to quantify, through a new model, the mean-flow viscous loss and turbulent loss. The authors adopted an analysis based on the estimation of the mean-flow kinetic energy and turbulent kinetic energy. The results showed that the energy loss due to turbulence is the main loss in the pump. Furthermore, the mean-flow viscous loss, mainly related to dissipation, decreases significantly under part-load conditions.

2.5 Two-phase liquid-liquid flows in centrifugal pumps

Two-phase liquid-liquid flows are omnipresent in the daily life of human beings, spanning from basic activities to industrial procedures. Across a diverse array of sectors, including food, chemicals, and pharmaceuticals, the occurrence of liquid-liquid dispersions is often a sought-after outcome. A notable instance of multiphase flow operation is observed in the mixture of viscous oil and water. Depending on the superficial velocities, these phases can adopt a dispersed flow pattern. The viscosity of this dispersion might surpass that of continuous phase, and its stability hinges upon the properties of the fluids involved and the quantity of energy dissipated during the flow. Understanding the dynamics of flow occurring within the impeller during operation is of paramount importance in establishing a foundational comprehension of the mechanisms underlying energy dissipation in dispersive systems.

The co-presence of oil and water within the impellers of pumps typically instigates the creation of dispersions characterized by high effective viscosity. Figure 2.15 visually depicts two distinct dispersions: water-in-oil (W/O) and oil-in-water (O/W).

Dispersions are characterized by the coexistence of droplets within a continuous phase. The morphology, rheological behavior, and stability of fluid dispersion hold profound implications in the context of new pumping designs. There are several classifications for dispersions: colloid, solution, suspension, among others. However, the main type of dispersion that occurs in industry is the emulsion composed of oil and water.

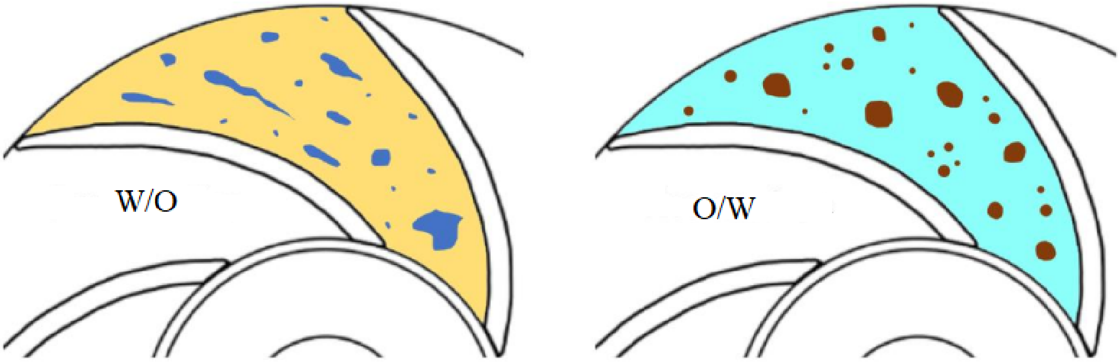

FIGURE 2.15 – Schematic illustration of dispersed drops in an impeller channel (Perissinotto, 2023).

In this context, the centrifugal pump can facilitate the initiation of emulsion formation. Within the confines of the impeller channels, rapid intermixing of fluids occurs due to the rotational motion of the blades. This interplay gives rise to shear forces, turbulence, and hydrodynamic instabilities, culminating in the rupture of one of the phases. Consequently, this phase adopts a morphological configuration characterized by dispersed droplets. With the passage of time, these droplets undergo successive fragmentation events, progressively assuming a distinctive size dictated by both pump conditions and liquid properties. Comprehensive insights into the process of emulsion development within centrifugal pumps can be sourced by Bulgarelli *et al.* (2020, 2021a,b, 2022).

Apart from the aforementioned investigations into emulsions, the literature encompasses numerous inquiries into two-phase liquid-liquid flows within pipes (Brauner & Maron, 1992; Angeli & Hewitt, 2000; Rodriguez & Oliemans, 2006; Grassi *et al.*, 2008; Wang *et al.*, 2011; Loh & Premanadhan, 2016; Cavicchio *et al.*, 2018). Nonetheless, the experimental characterization of liquid-liquid flow in centrifugal pumps remains relatively limited within the multiphase flows research domain. Some of the exceptions to this include investigations into the characterization of droplets dispersed on the impeller, as there is a relationship between average droplet diameter and pump performance.

In this context, the research conducted by Ibrahim & Maloka (2006) obtained drops size distributions in oil-in-water dispersion by using a laser particle size analyzer (LPSA). This apparatus incorporates both a laser emitter and a laser receiver, wherein the emitted light interacting with a droplet produces a diffraction pattern upon reception. The extent of diffracted light corresponds to the droplets dimensions, enabling their estimation.

Additionally, Morales *et al.* (2013) undertook an examination of oil drop formation within oil-in-water dispersions within a centrifugal pump. Employing an ultrasonic extinction spectrometer (UES) at the outlet of the centrifugal pump, the sizes of the oil droplets were measured. The UES operates based on ultrasound generation and detection; the waves encountering droplets undergo extinction at a frequency reliant on the droplet size. Their findings unveiled a direct correlation between drop size and impeller rotation speed. Consequently, for a continuous water phase, the researchers inferred that turbulence constitutes the principal mechanism governing oil droplet fragmentation. This conclusion paved the way for the formulation of a novel mechanistic model, facilitating the estimation of oil droplet diameters contingent upon the operational parameters of the pump.

More recently, innovative methodologies have emerged to evaluate droplet size distributions. The optical multimode online probe (OMOP) serves as a notable example of a shadowgraphic imaging instrument capable of discerning boundaries based on contrast disparities between droplets and their background. Consisting of dual probes — one housing a camera and the other a light source, interconnected by lenses — OMOP was harnessed by Schäfer *et al.* (2019) and Schmitt *et al.* (2021) to scrutinize oil and water droplet diameters both upstream and downstream of centrifugal pumps. Application of a convolutional neural network (CNN) procedure to process captured images proved effective for droplets exceeding 100 μm in size. Furthermore, an endoscope measuring probe (EMP), distinguished by its superior spatial resolution (1 pixel = 3.5 μm), was deployed to capture images at the discharge nozzle of a transparent pump. Consequently, the authors could investigate droplet breakup phenomena occurring within this stationary pump region, ultimately leading to the derivation of novel correlations from their observations.

Evidently, the analyses conducted using LPSA, UES, and OMOP have played a pivotal role in shaping understanding of droplet behavior within two-phase flows within centrifugal pumps. As previously elucidated, these techniques aptly identify droplet shape and size within regions external to the pump. However, these methods are insufficient in characterizing the dynamics and trajectories of individual droplets, a fundamental facet to advance in mathematical models.

In this context, Perissinotto *et al.* (2019b) embarked on employing a high-speed imaging (HSI) approach complemented by particle tracking velocimetry (PTV) techniques, which enabled the visualization of flow dynamics and real-time tracking of droplet movements within the impeller. Their study delved into the kinematics and dynamics of oil droplets dispersed within water, encompassing examinations of geometric attributes, characteristic dimensions, trajectories, velocities, accelerations, and dominant forces. Subsequently, the same group presented numerical simulations in another manuscript (Perissinotto *et al.*, 2019a), wherein estimations of velocities, forces, pressure gradients, and rates of turbulent kinetic energy dissipation were contrasted with experimental data and CFD outcomes.

Furthermore, Perissinotto *et al.* (2020) extended their investigation to encompass an inverted dispersion scenario, involving water droplets dispersed in oil. All test cases maintained a dispersed phase concentration below 1.5% by volume. The rotational speeds spanned from 300 to 1500 rpm, while the continuous phase flow rates ranged approximately between 1.0 and 6.0 m^3/h. Specifically, the water-in-oil dispersion entailed water droplets within oil characterized by a viscosity of 20 cP, whereas the oil-in-water dispersion featured oil droplets within water with a viscosity of 220 cP. To enhance visual contrast, a dark dye was introduced to the dispersed phase in both scenarios, thereby accentuating differentiation between the impeller hub (appearing white) and the observed droplets (appearing black). A representation is presented in Fig. 2.16.

As a complement to the work of Perissinotto *et al.* (2019b), Cerqueira *et al.* (2023) developed a PTV algorithm for analyzing the behavior of oil droplets in two-phase oil-water dispersions in the impeller of a centrifugal pump. The PTV algorithm was based on deep learning techniques for image processing. The authors used a combined U-Net and CNN method for droplet detection. The former method generated a binary image and the latter detected valid

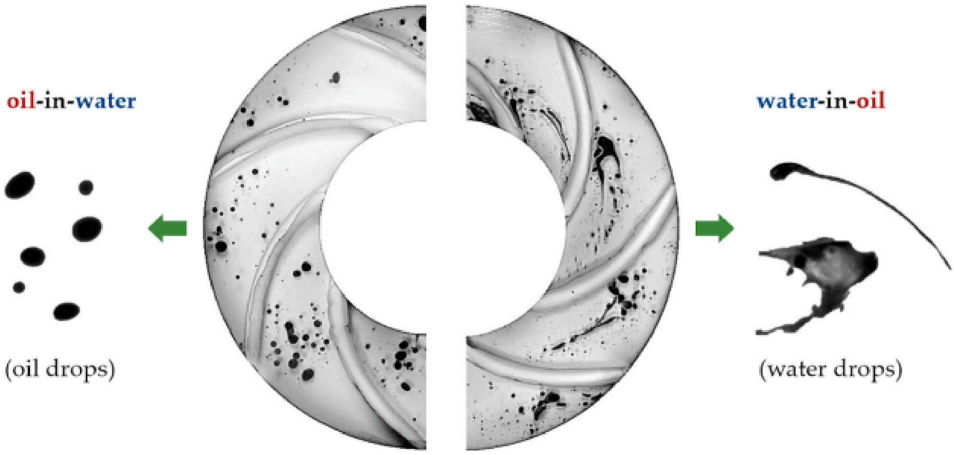

FIGURE 2.16 – Two-phase liquid-liquid dispersions in the impeller of a transparent prototype rotating at 600 rpm. The continuous phase is transparent and the dispersed phase is darkened with a black dye. The flow was visualized with HSI while the motion of liquid drops was analyzed with PTV method (Perissinotto *et al.*, 2021).

oil drop contours. After detection, labeled object velocimetry (LOV) was adopted to calculate the instantaneous velocity of the oil drop. A synthetic image generator based on a generative adversarial network (GAN) was then developed to evaluate the results of the U-Net, CNN and LOV models. The results of this work indicated that the proposed approach is able to calculate the correct size distribution even in situations where the oil volume fraction is high and overlap can become a problem.

The investigations referenced within this literature review, particularly within Secs. 2.4 and 2.5, present an overview of the research carried out with single-phase and two-phase flows inside centrifugal pumps. Within the ambit of the research conducted for single-phase flows, the literature exhibits considerable depth, encompassing endeavors that elucidate the flows morphological attributes, alongside studies that provide both quantitative and qualitative assessments of energy dissipation within the impeller. However, a notable gap within the existing body of literature on centrifugal pumps pertains to an analysis seeking to characterize the unstable turbulent flow and establish its correlation with the associated energy losses occurring within the pump impeller. In light of this unaddressed research gap, one of the primary objectives of this PhD thesis was to conduct a series of experiments utilizing the PIV technique, aimed at establishing a comprehensive relationship between turbulent flow patterns and the consequential energy dissipation phenomena.

From the information presented in Sec. 2.5, it is possible to verify that the investigation of the two-phase liquid-liquid flow inside centrifugal pumps is quite limited. Most of these studies seek to analyze the performance of pumps in operation with the presence of dispersions composed of water and oil. The characterization of these dispersions is carried out with microscopy and endoscopy equipment, or probes based on ultrasound and laser. These equipments are suitable for measuring the diameter of small drops in emulsions, but they are not able to analyze the dispersed drops motion inside impellers or the flow field resulting from the interaction between the phases. Thus, analogously to the single-phase experiments, PIV data were collected for a two-phase oil-in-water (O/W) flow in order to verify the influence of the dispersed oil phase on the continuous aqueous phase.

3 Setup and experimental procedure

In this chapter, the design and implementation of a transparent centrifugal pump prototype engineered to facilitate PIV investigations will be described. The experimental bench used for conducting tests, along with the PIV system employed for optical access to the flow, will be introduced. Additionally, the procedures applied in both single-phase and two-phase flows within the centrifugal pump impeller under consideration will be outlined. Thus, initially, the geometric description of the centrifugal pump prototype will be presented, in addition to details on the materials used to manufacture the device. Subsequently, the circuit will be presented. The circuit components will be described, as well as the measuring instruments and the test matrix. The PIV optical measurement system used is then presented, followed by the procedures used to obtain the experimental measurements for single-phase and two-phase flows. The experimental apparatus used in this work was built at the Experimental Petroleum Laboratory (LabPetro), at the Center for Energy and Petroleum Studies (CEPETRO), on the campus of the University of Campinas (UNICAMP) in Brazil.

3.1 Transparent pump

To enable PIV measurements in the whole impeller, a prototype of a centrifugal pump with spiral volute was designed and manufactured out of a transparent material for flow visualization purposes. The impeller has a radial geometry with seven channels of constant height and low aspect ratio (about $h/D \approx 5\%$). The outer radius is $r_{\text{out}} = 55$ mm and inner radius $r_{\text{in}} = 22$ mm. Thus, the impeller has a geometry similar to that used by Monte Verde (2016) and Perissinotto (2023) in their experiments. The main impeller parameters are shown in Fig. 3.1 and Tab. 3.1.

The frontal plane of the impeller, known as the shroud, was manufactured polished acrylic material, characterized by a high degree of optical transparency. This design choice was made to facilitate entry of light in all channels of the impeller. The impeller blades were also fashioned from transparent acrylic using precision machining techniques. This particular configuration aimed to optimize the passage of light through all the channels within the impeller.

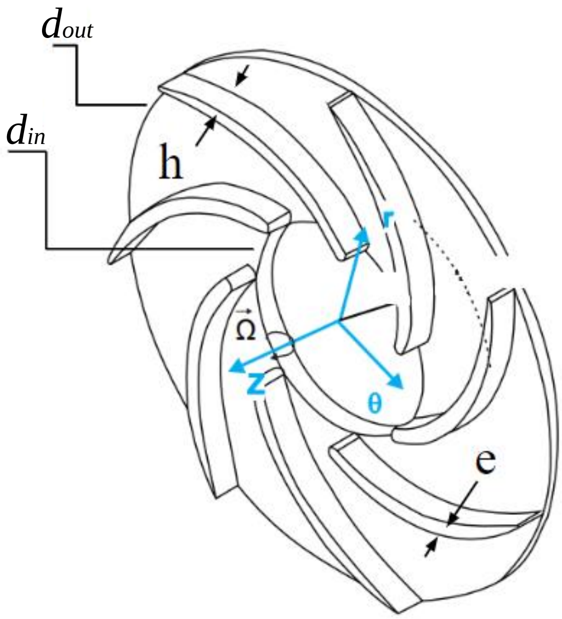

FIGURE 3.1 – Schematic illustration showing the impeller geometry.

TABLE 3.1 – Main geometrical attributes of the impeller.

Parameters	Sign	Values
Inlet diameter [mm]	d_{in}	44
Outlet diameter [mm]	d_{out}	110
Blade thickness [mm]	e	5.5
Blade's height [mm]	h	6.0

In order to mitigate the influence of diffuse reflections during experimental procedures, both the posterior plane of the impeller (hub) and the lower portion of the volute were fabricated from matte black anodized aluminum. This strategic choice was implemented to curtail the scattering of light and unwanted reflections, enhancing the overall image quality and clarity during experimentation.

Thus, the chosen arrangement for this centrifugal pump design ensures a discernible contrast in the images captured by the imaging apparatus. This is essential, particularly for instances where tracer particles, represented by their reflective characteristics (light color), need to be distinctly differentiated from the background, which, in this context, corresponds to the dark-colored pump bottom. A schematic representation and visual depictions of the pump's configuration can be observed in Figs. 3.2 and 3.3.

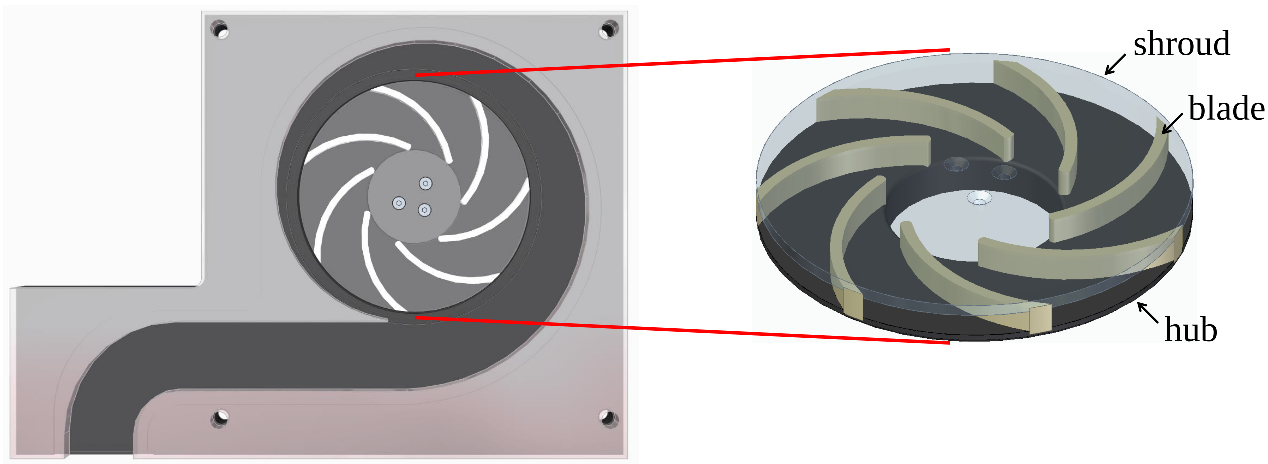

FIGURE 3.2 – Drawings of the pump stage highlighting the impeller (Fonseca *et al.*, 2023).

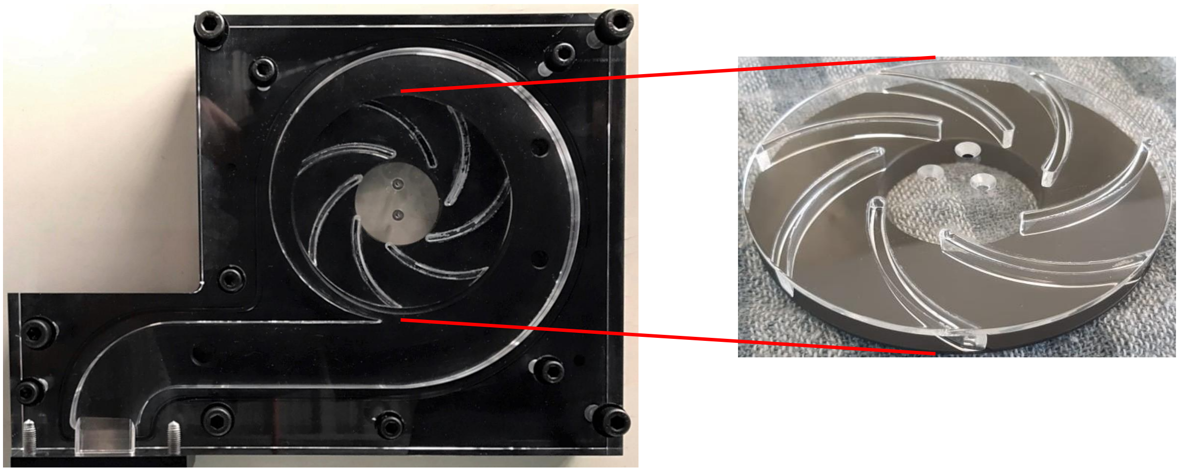

FIGURE 3.3 – Photographs of the pump stage, highlighting the impeller (Fonseca *et al.*, 2023).

As shown in Fig. 3.4, the prototype incorporates dual inlets designed to accommodate two distinct fluid mediums, thereby enabling the operation with liquid-liquid mixtures. The strategic positioning of entry and exit points for these fluids has been meticulously chosen to ensure non-interference of the camera in the test section.

In detail, the continuous phase enters the pump stage through four intake ports placed on the side of the pump body. The liquid then flows to the impeller inlet, traverses the channels, and finally goes to the volute before leaving the pump. The outflow direction is perpendicular to the axis of the pump shaft.

Conversely, in instances where a dispersed phase, coexisting with the continuous medium, is requisite, introduction of this secondary phase is via a threaded connection affixed above an injection chamber. The dispersed phase traverses the central shaft, extending to its extremity wherein an assembly of seven holes symmetrically positioned, await. Each orifice performs the task of injecting the dispersed medium into one of the impeller's seven channels. It is pertinent to emphasize that upon injection, the dispersed phase assumes a droplet-dispersed configuration.

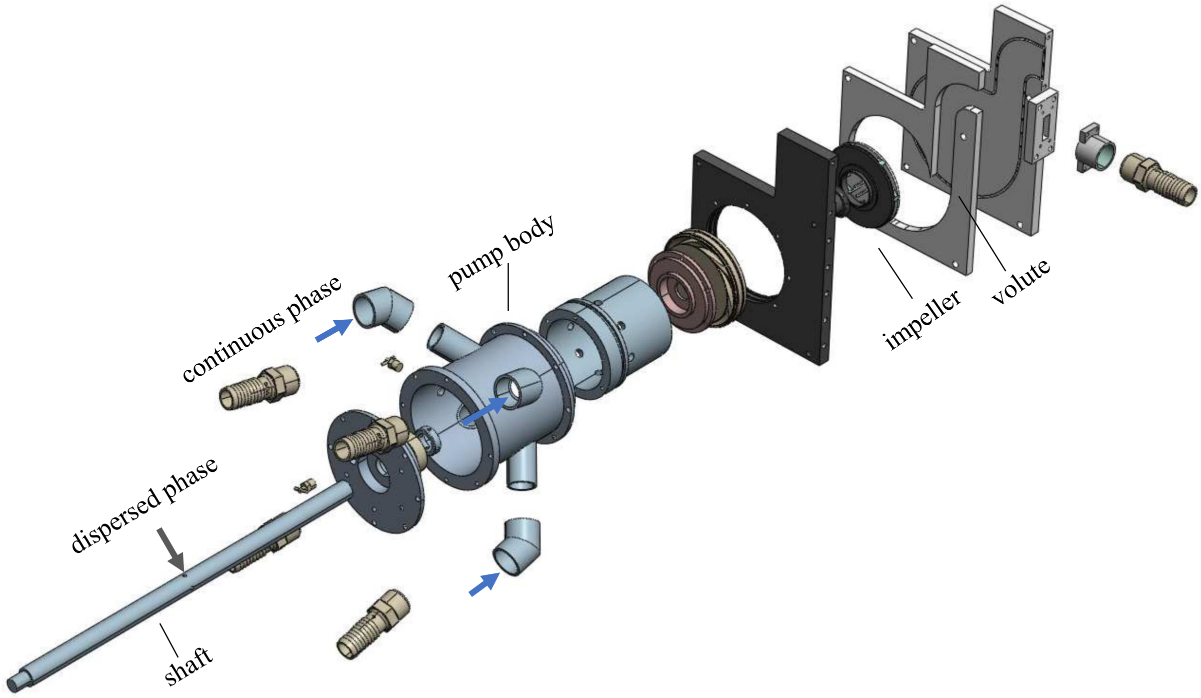

FIGURE 3.4 – Pump prototype exploded view.

3.2 Experimental test rig

The layout of the experimental test rig is depicted in Fig. 3.5. As can be observed, the setup is essentially composed of a water flow line with a tank, a booster pump, valves and instruments to control and measure the temperatures (T_{in} and T_{out}), water mass flow rate ($\dot{m}_w$), oil mass flow rate ($\dot{m}_o$), pressure in the suction region of the transparent pump (P_{in}), pressure increment generated by this pump (ΔP_{pump}), and rotational speed of its closed radial impeller ($\mathcal{N}$), which moves together with the shaft.

As illustrated in Fig. 3.5, in the continuous phase circuit, the booster pump forced the fluid transfer from the reservoir to the designated test line (indicated by orange lines), effectively counteracting any losses incurred through the pipeline and associated components. The frequency inverter played a pivotal role in modulating the rotational speed of the booster pump, thereby indirectly regulating the pressure at the entrance of the prototype pump. The fluid subsequently traversed through the Coriolis flowmeter and optionally through the heat exchanger. Following this, transducers gauged both the pressure and temperature of the fluid that ultimately ingress the prototype pump.

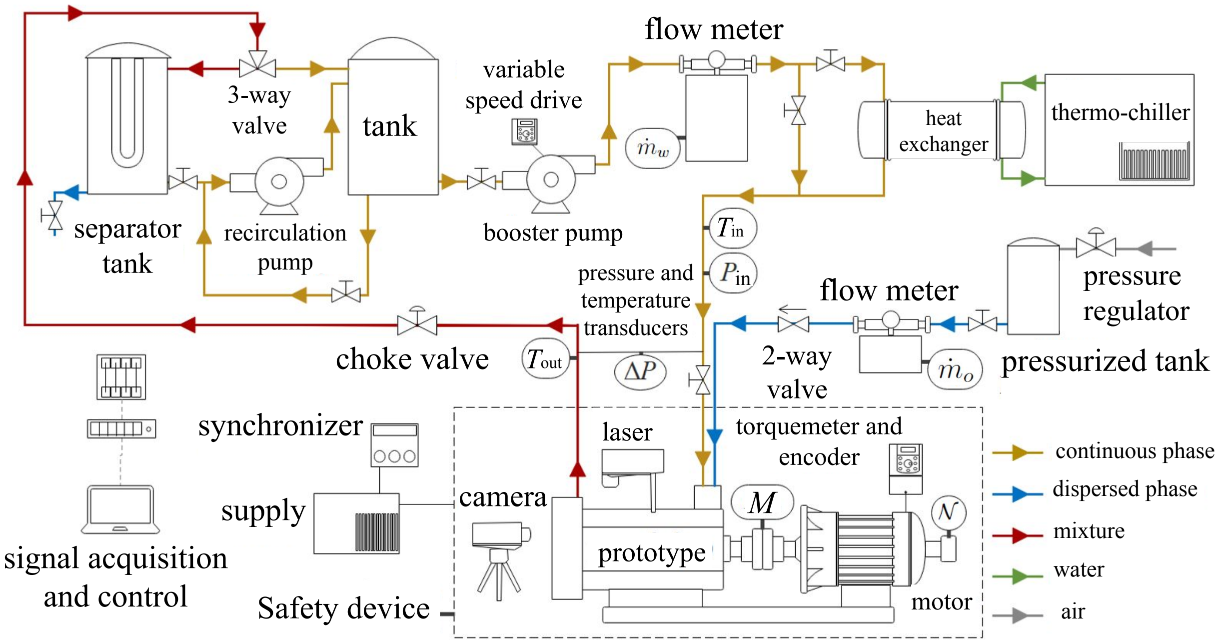

FIGURE 3.5 – Layout of the experimental test rig.

It is worth mentioning that the transparent pump was designed to provide the pressure increment produced only by the impeller (ΔP_{imp}) without influences from the vaneless diffuser or components attached to the pump casing. The pump has measuring points connected to the impeller eye (inlet) and impeller-volute boundary (outlet) so that the pressure sensors are able to obtain a measure of ΔP_{imp} neglecting other parts located upstream or downstream of the impeller.

The test rig also provides a measurement of the torque applied by the electric motor to the pump shaft (M_{pump}). This shaft moves the motor-pump set, composed of transparent pump, electric motor, bearings and mechanical seals. Thus, M_{pump} is the torque associated with the entire motor-pump set, considering all the parts mounted on it. As a result, when analyzing the impeller individually, the torque in this rotating part (M_{imp}) must be estimated indirectly.

To estimate M_{imp}, an extra experiment is executed: the pump is operated without any liquid inside, in a procedure denominated as "dry running" (Perissinotto *et al.*, 2023). In this condition, the measurement from the torque meter (M_{dry}) disregards the torque applied to the shaft due to the presence of fluid in the impeller. In other words, the torque M_{dry} addresses only the torque associated with the other components (motor-pump coupling, bearings, seals). Through a simple subtraction, it is possible to obtain the torque on the impeller: $M_{\text{imp}} = M_{\text{pump}} - M_{\text{dry}}$.

The dispersed phase line functioned as a conduit for introducing an additional fluid into the prototype pump, facilitating the creation of a two-phase liquid-liquid flow. This secondary liquid was initially contained within a pressurized tank, situated beneath a compressed air camera whose pressure was under the governance of a proportional regulator. Under these conditions, the air pressure assumes function for governing the liquid flow rate, given their directly proportional relationship. As the liquid departs from the reservoir, it traverses through both the flow meter and an *on/off* solenoid valve, culminating at the transparent prototype pump, where it mixtures with the continuous phase. Subsequently, the flow passes through the prototype pump, while the encoder and torquemeter perform measurements relevant to the rotation speed and torque. At this point, fluids can be visualized and measured using the PIV method.

In conjunction with the previously delineated components, the experimental setup incorporates an array of fundamental hydraulic elements, including but not limited to elbows, sleeves, flanges, unions, and valves. The entire piping network, along with its accessories, primarily utilizes CPVC, a thermoplastic known for its outstanding resistance to high pressures and temperatures.

3.2.1 Measuring instruments

The continuous phase mass flow rate ($\dot{m}_w$) was acquired through the utilization of a strategically placed Coriolis-type flow meter (Emerson - MicroMotion F200) between the outlet of the booster pump and the inlet of the prototype pump. Concurrently, within the framework of the injection system, the mass flow rate corresponding to the dispersed phase ($\dot{m}_o$) was established using an additional Coriolis type meter (Emerson - MicroMotion D6). By possessing both the mass flow rate ($\dot{m}$) and the specific mass (ρ) for a given fluid, the computation of the volumetric flow rate (Q) becomes achievable, thereby enabling its integration into the pump performance curves.

Angular position (θ) and angular speed (Ω) were measured via an encoder (IFM Electronic - RUP500), integrated with the pump shaft. This combination of parameters facilitates the expression of Ω in terms of impeller rotation ($\mathcal{N}$), making it a fundamental element for calculating angular speed, as further explained in Sec. 2.1.2.

The pressure at the inlet of the prototype pump ($P_{\text{in,pump}}$) was assessed through employment of a gauge pressure transducer (Emerson - Rosemount 2088). Moreover, the incremental pressure imparted by the pump to the fluid (ΔP) is quantified via a differential pressure transducer (Emerson - Rosemount 2051). During the experimental phase, it was imperative to maintain pressure at a consistent level to obviate pump cavitation. Measurement inlet (T_{in}) and outlet (T_{out}) temperatures of the prototype was executed via two resistance thermometers (ECIL - TS Series). For a thorough understanding of the instruments employed, including calibration and uncertainty analysis, please refer to Perissinotto (2023).

The analog output signals from these instruments were acquired through a *National Instruments* system, and the measured data were monitored and stored by a LabVIEW™ supervisory control program initially developed by Perissinotto (2023) and then adapted for this PhD thesis. The pressure transducers are mounted at the pump inlet and outlet, and the impeller rotation speed is controlled by a variable frequency drive system. The flow rate through the impeller is adjusted by setting the rotational speed of the booster pump and the opening or closing of the discharge valve (choke valve) assembled at the pump outlet. All instruments present uncertainties lower than 0.5% of the measured values.

3.2.2 Test matrix

Single-phase flow

In this study, PIV measurements for single-phase flow were performed at three fixed rotational speeds ($\mathcal{N}$) and three water flow rates (Q_w) for each $\mathcal{N}$. The water flow rate is expressed relative to the pump's best efficiency point (Q_{BEP}), denoted by Q^*. The Reynolds number was calculated based on both the impeller's angular speed and the hydraulic diameter of the impeller channel. Specifically, the Reynolds number based on angular velocity, Re_Ω, was determined using the rotational speed and the impeller's outer diameter. Conversely, the Reynolds number based on the hydraulic diameter, Re_c, was derived from the average flow velocity obtained from the PIV measurements and the hydraulic diameter of the impeller channel. The experimental matrix is detailed in Tab. 3.2.

The experimental conditions encompassed a range of $\mathcal{N}$ set at 300, 600, and 900 rpm along with nine distinct flow rates. Flow rates were quantified using a Coriolis flow meter, primarily capturing mass flow rates ($\dot{m}$), which were subsequently converted into volumetric flow rates ($Q = \dot{m}/\rho$). It is worth noting that throughout the experiments, the water remained at a constant temperature of T = 25°C, with corresponding fluid density of ρ = 997 kg/m^3. Additionally, the dynamic viscosity of the fluid at this temperature was approximated as μ = 9×10^{-4} Pa·s.

TABLE 3.2 – Test matrix of single-phase experiments.

$\mathcal{N}$ [rpm]	Re_Ω	Q_w [m^3/h]	$Q^* = Q_w/Q_{BEP}$	Re_c
300	3×10^6	0.225	0.3	1,896
		0.75	1.0	6,312
		1.125	1.5	9,484
600	7×10^6	0.45	0.3	3,787
		1.5	1.0	12,633
		2.25	1.5	18,949
900	1×10^7	0.66	0.3	5,545
		2.2	1.0	18,503
		3.33	1.5	28,023

The specified flow rates adopted in the experimental matrix (Tab. 3.2) were determined via preliminary assessments designed to characterize the pump's operational performance. The initial computation of pump head (H_{pump}) and efficiency ($e_{ff,\text{pump}}$) was derived from instrument measurements. Subsequently, the flow rate corresponding to BEP was determined for all rotational speeds. Figure 3.6 illustrates the range of flow rates examined in this research, spanning from a condition near pump shut-off (with higher pump head and lower flow rate) to a condition resembling open-flow (with lower pump head and higher flow rate).

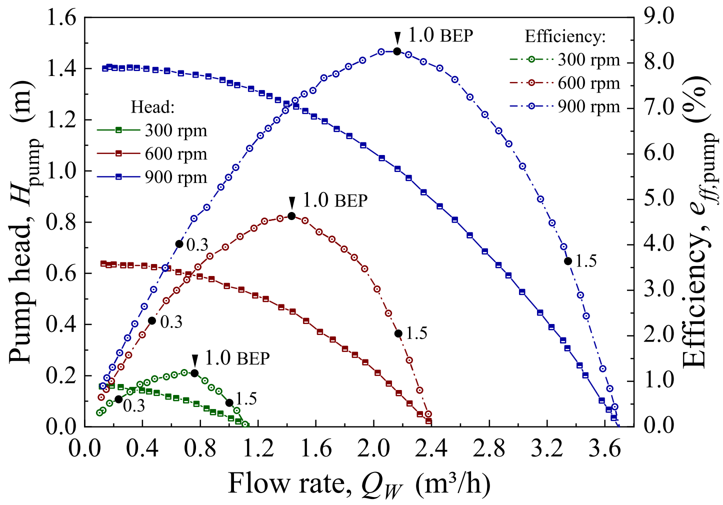

FIGURE 3.6 – Performance curves of the pump prototype (Fonseca *et al.*, 2023).

As depicted in Fig. 3.6, the pump exhibits an efficiency range of approximately 1% to 8% across the investigated rotational speeds, which are notably lower in comparison to typical commercial pumps. The diminished efficiency, denoted as $e_{ff,\text{pump}}$, can be attributed to frictional losses occurring within the mechanical components situated in the transmission system of the motor-pump assembly, as detailed in Perissinotto (2023). The pump assembly incorporates five bearings and three mechanical seals, each contributing to energy dissipation through friction. The total torque required to mobilize all these elements is quantified using a torque meter.

However, it is essential to emphasize that the relatively low efficiency of the prototype does not hinder the objectives of this study. The pump was originally designed for flow visualization purposes, and the incorporation of bearings and seals on the shaft, while diminishing efficiency, does not compromise the functionality of the apparatus. As a result, the machine continues to yield performance curves consistent with those of a centrifugal pump.

Two-phase flow

Two-phase flow tests within the centrifugal pump were carried out to analyze mineral oil-in-water mixtures. The mineral oil used in PIV experiments is commercially available in Brazil under the chemical designation "hydrogenated white oil USP grade." As outlined in the safety data sheet, this oil is transparent, colorless, and non-flammable, with low solubility in water.

For the two-phase tests, a smaller experimental matrix was adopted, constrained to a single rotation ($\mathcal{N} = 300$ rpm) and water flow rates below the BEP ($Q_w < 0.75$ m^3/h). Simultaneously, oil was added to the continuous water phase at a constant mass flow rate ($\dot{m}_o = 2.0$ g/s). At the low oil-in-water fractions employed in this study, the pump performance did not undergo significant variations. Consequently, the BEP was the same for both single-phase water and two-phase oil-in-water flow. These performance tests were carried out prior to the development of the test matrix, outlined in Tab. 3.3.

The decision to conduct two-phase experiments at lower rotation speeds and reduced flow rates is based on the size of oil droplets. The literature reveals that pump rotation and flow rate influence droplet size, with the size of an oil droplet being inversely proportional to $\mathcal{N}$ and Q_w (Perissinotto *et al.*, 2019b). This behavior was confirmed through tests conducted to define the matrix in this study. When $\mathcal{N} > 300$ rpm and/or $Q_w > 0.75$ m^3/h, the droplets become so small in PIV images that their size becomes comparable to the size of light reflected by seeding particles, impairing the identification of both. Furthermore, at higher flow rates and rotation speeds, droplet breakage is so intense that the mixture rapidly transforms into an emulsion. Consequently, the oil-in-water mixture becomes cloudy and whitish within a few seconds of experiments. This results in the impossibility of continuing the tests, requiring interruption and resumption only when the mixture separates in the experimental line tank.

Table 3.3 – Test matrix of two-phase oil-in-water experiments.

$\mathcal{N}$ [rpm]	$\dot{m}_o$ [g/s]	Q_w [m^3/h]	$Q^* = Q_w/Q_{BEP}$
		0.225	0.3
300	2.0	0.375	0.5
		0.525	0.7

Preliminary rheological tests confirmed the Newtonian behavior of the oil used as the dispersed phase in the PIV experiments. This behavior, characterized by a linear increase in shear stress with shear rate, shows a viscosity range from 28 cP at 15°C to 8 cP at 45°C. Although the oil temperature was not rigorously controlled during the PIV experiments, it generally stayed within the 20 to 30°C range, aligning with the laboratory temperature. For ease of reference, a temperature of 25°C is considered, at which the oil's viscosity is approximately $\mu \approx 0.017$ Pa.s or $\mu \approx 17$ cP. The viscosity curve can be adequately represented by the exponential fit $\mu(T) = 3.78 + 57.4\ e^{-0.0576T}$, as illustrated in Fig. 3.7.

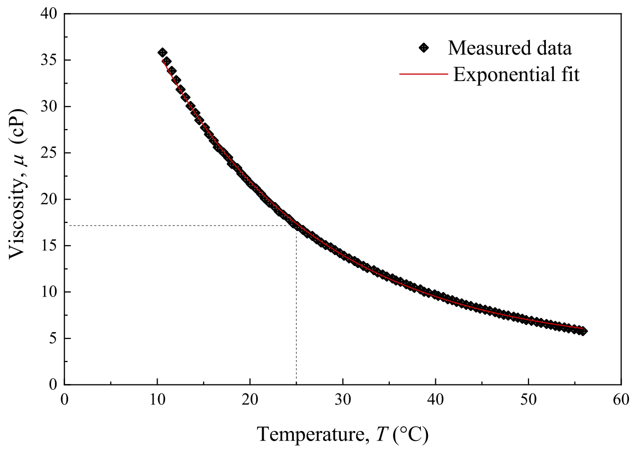

FIGURE 3.7 – Curve of oil viscosity as a function of temperature.

3.3 PIV setup

The experimental apparatus employed in this investigation encompasses the use of a *DualPower 30-1000* time-resolved PIV (TR-PIV) system from *Dantec Dynamics Inc.*, which was deployed for the purpose of visualizing and quantifying the fluid flow within the prototype pump within the context of this PhD thesis. The fundamental operational principles of this methodology are detailed in Sec. 2.2.

The PIV system deployed consists of a variety of components, ranging from simple accessories to highly sophisticated equipment with advanced technology. Table 3.4 provides a brief description of the main components that constitute the PIV system.

TABLE 3.4 – Detailed specifications of key components in the PIV system.

Component	**Brands and models**	**Characteristics**
Laser head	Dantec Dynamics (*DualPower 30-1000*)	Two cavities, wavelength 527 nm, pulsation frequency from 0.2 to 20 kHz, power 30 mJ per pulse at 1 kHz.
High-speed camera	*Phantom - VEO 640*	Monochromatic CMOS sensor, 12-bit depth, 72 GB internal memory, 2560x1600 pixel resolution at a maximum frame rate of 1400 frames per second.
Synchronizer	Dantec Dynamics (*High resolution sync.*)	4 inputs and 32 outputs, minimum pulse duration of 6 ns, minimum time between pulses 6 ns, 1 ns resolution.

As depicted in Tab. 3.4, the primary components of the system include a power supply, a pulsed laser generator, a synchronizer, a high-speed camera (*Phantom VEO640*), and the *DynamicStudio 7.4* software, which controls the PIV measurements. The system's standout feature is its capacity to emit high-frequency pulses with intense energy (up to 30 mJ at 1 kHz). This unique capability classifies the equipment as a time-resolved (TR-PIV) system, significantly expanding the scope of potential analyses and outcomes.

The pump prototype is illuminated from both sides laterally by a dual light guide system composed of lenses and mirrors, allowing for the adjustment of the position and thickness of the laser sheets. The mid-plane of the impeller, perpendicular to the pump shaft, was selected for all measurements. During the tests, the field of view covered the entire transparent stage to reveal an overview of flow structures. Fluorescent particles of PMMA doped with rhodamine-B dye were introduced into the fluid to serve as fluorescent tracers in the laser-induced fluorescence (LIF-PIV) technique. These particles have an average diameter of 35 μm.

The flow is illuminated by a double-pulsed laser (Nd:YAG type) with a wavelength of 532 nm, and the flow images are captured by a high-speed camera (CMOS sensor) with a spatial resolution of 2560 px × 1600 px, resulting in an acquired image with a 0.1 mm/px ratio. To set up the 2D2C-PIV configuration, the camera was installed perpendicular to the light sheets. A high band-pass filter for wavelengths above 545 nm was attached to the camera lens to filter out all light scattered by the interfaces, capturing only the light fluoresced by the seeding particles. Figure 3.8 depicts an illustrative scheme of the experiment (Fig. 3.8a) and a photograph of the experimental setup of the pump during a single-phase PIV test (Fig. 3.8b), respectively, emphasizing the laser illumination configuration.

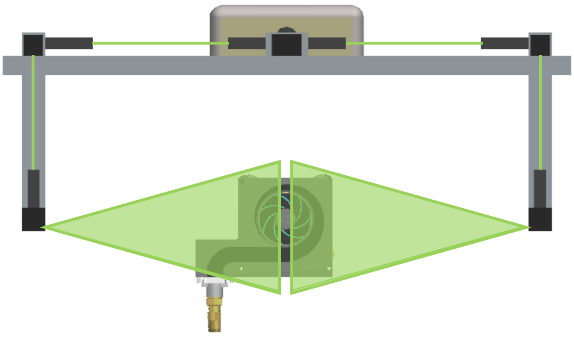

(A) scheme of the dual light guide system

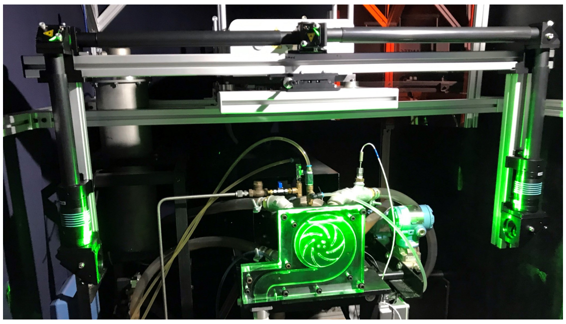

(B) photograph of the dual light guide system

FIGURE 3.8 – Experimental facility: PIV system illuminating the transparent pump during a PIV test (Fonseca *et al.*, 2023).

3.4 Procedure for single-phase tests

3.4.1 Pump performance test

At the beginning of the research, the performance of the centrifugal pump in different scenarios was focused on being evaluated. This step, as well as the second set of experiments (Sec. 3.4.2), consisted of two stages: i) preparation and ii) data acquisition. Below, the details are provided.

Preparation

The preparation stage of the experiments consisted of three steps, starting with checking the water level in the mainline tank. The amount of water was ensured to be above half the maximum capacity, adjusting it as needed by adding filtered water.

The two valves that controlled the flow between the mainline tank and the booster and recirculation pumps were then opened. Additionally, two valves at the inlets and outlets of the transparent prototype were opened, ensuring that the water flow was specifically directed.

A crucial aspect of this stage involved the control components being checked, which included the activation of the pumps' frequency inverters and confirmation that they were configured for remote mode of operation. The data acquisition infrastructure was also essential. The computer that controlled the experimental bench was turned on and the recognition of the acquisition modules was verified. Then, the LabVIEW^{TM} supervisory control program was opened to be prepared to collect the data generated by the experiments.

Data acquisition

The data acquisition to characterize the operational behavior of the prototype pump was conducted in accordance with a precise protocol. Initially, the desired rotation of the prototype pump was established using a frequency inverter through the LabVIEW^{TM} supervisory program.

Subsequently, the speed of the booster pump was adjusted, also controlled by a frequency inverter. The objective was to ensure that the water reached the suction of the prototype pump with a positive gauge pressure, while the pressure increase in the prototype pump remained at zero. This stage marked the beginning of the test and corresponded to the open-flow condition, characterized by maximum flow rate and zero head.

To ensure the stability of operating conditions, a period of ≈ 2 minutes was waited. After this interval, the program was activated to perform data acquisition and store it in a file, allowing for subsequent analysis.

Continuing, the supervisory system was operated to slightly close the choke valve in the return line. This was intended to restrict the flow and obtain a new flow rate, representing a new operating point with a flow rate below the open-flow condition.

The previous steps were repeated several times, varying the operating condition, until a flow rate of zero and the maximum head were reached, defining the shut-off condition.

Finally, the procedure was replicated for different rotation speeds of the prototype pump, allowing for a comprehensive characterization of its operational behavior under various conditions. The characteristic curve of the prototype pump operating under single-phase flow is depicted in Fig. 3.6.

3.4.2 PIV measurements of single-phase flow

To conduct PIV flow visualization tests, the previously established procedures for bench preparation were reiterated. These procedures, which had been previously utilized in pump performance tests, ensured the optimal condition of all components, including pumps and instruments, and the absence of air bubbles in the circuit.

Preparation

The first stage of preparation for the flow visualization tests involved activating the two general PIV circuit breakers, along with the uninterruptible power supply (UPS) and battery circuit breakers. On the laser source panel, the emergency button was deactivated, the key was turned to the "on" position, and the communication system was verified to be in remote mode.

Following this, the refrigerant fluid level was assessed using the display on the equipment's front, with the option to top up the reservoir using the manufacturer's original fluid, if needed. Afterward, a waiting period of five to ten minutes was observed for the laser crystals to reach the target temperature of 70°C.

The camera and synchronizer were activated, and a thorough inspection of cable positioning, lens alignment, tripod stability, and other system components was conducted.

Subsequently, the PIV system control computer was powered on, and the *Litron Control* program was launched to configure the frequencies and powers of the diode and laser emitters in the external mode. The *DynamicStudio* program was also initiated, with the necessary adjustments made for image acquisition, including the definition of parameters such as the time between pulses and the interrogation window.

Upon returning to *Litron Control*, the laser was activated, and the shutter was opened. Operating the laser at an attenuated power level of approximately 5%, the initial image acquisitions were conducted to ensure their quality. The power was gradually increased until the desired level of illumination was achieved, with special attention paid to possible significant light reflections. Subsequently, two frames from a sample of images were scrutinized for variations in brightness or an uneven light distribution. If these issues were detected, the realignment of the laser planes was carried out.

The quantity of tracers present in the images was also evaluated, and, if necessary, additional seeding particles were introduced into the water tank. To ensure a homogeneous mixture with the fluid, the seeding tracers were pre-dissolved in a beaker before being added to the water tank.

Data acquisition

Image acquisition using *DynamicStudio* software requires the adjustment of a set of parameters associated with the operation of the PIV system. These adjustments are made according to the desired acquisition mode.

The PIV system used in this research is capable of operating in two distinct modes. In the first mode, known as the “automatic mode,” the laser and camera are activated while the impeller rotates freely. In this configuration, the high acquisition frequencies of the TR-PIV system can facilitate the capture of many images in short time intervals, prioritizing the analysis of transient phenomena in instantaneous velocity fields.

In the second mode, called the “triggered mode,” obtaining a pair of images depends on the trigger provided by the encoder when detecting that the impeller has passed through a defined angular position (θ). Therefore, images are recorded with each complete revolution of the impeller, with the channels always in the same position, enabling the investigation of average velocity fields.

When using the encoder, a value must be defined for the triggering window, which consists of a time interval within which complete synchronization between the camera, laser, and encoder signals must occur.

The time between pulses (Δt) was the parameter that required the most effort and time in the determination process. Comprehensive PIV tests, involving the capture of 50 to 100 pairs of images, had to be exclusively executed to find the optimal Δt, whose significance was discussed in Sec. 2.2. If Δt is small, uncertainty increases because calculated velocity is inversely proportional to time; if Δt is large, there may be losses of particle pairs in the interrogation windows, for example.

The procedure adopted to configure Δt is described below and follows the guidelines presented in Perissinotto (2023). This procedure was repeated for each new experimental point, under each of the investigated operational conditions.

1. For a known fluid flow rate (Q_w) that passes through the impeller's smallest possible cross-sectional area (A_1), the expected maximum velocity $U_{\max} = n_0 Q_w / A_1$ is estimated in the channel. The factor n_0 is applied to account for possible irregularities in the impeller's velocity profile. (In this PhD thesis, $1.5 \leq n_0 \leq 3.5$).

2. Next, the size of the square interrogation window (X_{IW}) to be used in the processing is defined in pixel and millimeters. The aim is to limit the particle displacement to a fraction of this size, so a maximum displacement is defined as $\Delta X_{\max} = n_1 X_{IW}$. (In this PhD thesis, $n_1 = 0.25$).

3. Thus, a first pulse interval is calculated: $\Delta t_1 = \Delta X_{\max}/U_{\max}$. Then, a preliminary PIV test with 10 pairs of images is carried out using the obtained Δt_1. Based on a visual inspection of the raw images, the value of Δt_1 is classified as either valid or invalid. (If invalid, return to step 1 and change n_0).

4. Once the value of Δt_1 is confirmed, $\Delta t_2 = n_2 \Delta t_1$ and $\Delta t_3 = n_3 \Delta t_1$ are defined, where $n_2 < 1$ and $n_3 > 1$. Therefore, with three candidates for the best time between pulses, three PIV experiments must be conducted to acquire 50 to 100 pairs of images. The processing is done in two separate parts: first in the impeller and then in the volute.

5. The results of the processed tests are analyzed. The vectors provide real maximum velocities ($\mathbf{U}_{\max_i}$) that give rise to new time intervals ($\Delta t'_i$) calculated as $\Delta t'_i = \Delta X_{\max}/|\mathbf{U}_{\max_i}|$. In total, three values of $\Delta t'_i$ are computed for the impeller and another three values of $\Delta t'_i$ are determined for the volute.

6. These values of $\Delta t'_i$ are compared to each other, looking for similarities and differences. If convergence is observed, an optimal value for the pulse interval for the impeller, Δt_{imp}, and another for the volute, Δt_{vol}, are defined. (However, if no convergence is observed, return to step 4 and modify n_2 and n_3. In this PhD thesis, $n_2 = 0.5$ and $n_3 = 1.5$ were used in most experimental points).

7. Finally, the definitive pulse interval is calculated as the weighted average of the ideal intervals for the impeller and the volute: $\Delta t = (n_4 \Delta t_{\text{imp}} + n_5 \Delta t_{\text{vol}})/3$. (In this PhD thesis, to prioritize the rotating element, a higher weight was assigned to the impeller, so $n_4 = 2.0$ and $n_5 = 1.0$ were used).

The single-phase experiments in this study employed the two acquisition modes: "triggered mode" and "automatic mode". In the triggered mode, PIV measurements involved capturing 3,000 pairs of flow images. This substantial number of image pairs was necessary to ensure the convergence of turbulent flow field calculations. The acquisitions in this mode were conducted at a frequency of 200 Hz. On the other hand, in the automatic mode (double-frame TR-PIV), a frequency of 700 Hz was employed, and a total of 2,000 pairs of flow images were captured.

3.5 Procedure for two-phase tests

In a manner similar to the procedures conducted for obtaining measurements of single-phase flow, this section will be subdivided into two parts: pump performance tests and PIV measurements for two-phase flow.

3.5.1 Pump performance test

The performance tests of the centrifugal pump, operating with two-phase oil-in-water flow, were conducted following the initial procedures outlined in Sec. 3.4.1. After the verification of experimental components, the necessary steps were initiated.

Preparation

Initially, the valve of the compressed air circuit was manually opened, with verification of the operational status of the air pressure regulator and inspection of hose connections to ensure system integrity.

Subsequently, the valve located at the bottom of the oil tank was manually opened. Simultaneously, in the LabVIEW^{TM} supervisory program, the 2-way *on/off* valve was positioned in the open position, initiating the process.

The PID controller of the supervisory program was then activated to commence the injection of oil into the prototype pump, establishing a safe maximum limit for the air pressure in the tank and ensuring operation within safe parameters.

An intermediate oil flow rate was introduced during the pressurization of the tank. In this process, a visual inspection of the pump stage was conducted to confirm the effective injection of droplets, while waiting for the complete elimination of any air bubbles. Finally, the PID controller of the supervisory system was again activated to cease the oil injection, concluding the testing cycle.

Data acquisition

The data acquisition process to characterize the operational behavior of the prototype pump under two-phase oil-in-water flow followed the same protocol presented in Sec. 3.4.1. In alignment with the steps outlined in the single-phase flow procedure, the LabVIEW^{TM} supervisory program was utilized to define the desired speed for the prototype pump.

Subsequently, adjustments were made to the rotation of the booster pump using a frequency inverter, ensuring maximum water flow and maintaining zero pressure increase, thus defining the open-flow condition.

The PID controller within the LabVIEW^{TM} program was then activated to set the desired oil flow rate. Following this, the three-way valve in the return line was manipulated, diverting the oil-water mixture to the emulsion separation tank. After ≈ 2 minutes, the LabVIEW^{TM} program was executed, and the data acquisition was performed and stored in a file.

Continuing within the LabVIEW^{TM} supervisory system, oil injection was stopped, and the

3-way valve was reverted to its original position (see Fig. 3.5).

Following this, the choke valve in the return line was closed, constraining the mass flow rate to achieve a new water flow rate. This process was repeated until the pump characteristic curve for two-phase flow was established, from open-flow to shut-off condition, in which the water flow rate is minimum and the pressure increment is maximum.

3.5.2 PIV measurements of two-phase flow

The preparation steps for PIV measurements of two-phase flow, the methodology used to determine the time between pulses (Δt), and the image acquisition process followed the same guidelines presented for single-phase flow (Sec. 3.4.2). However, image acquisitions of the two-phase flow using the *DynamicStudio* software were carried out only in "automatic mode" to simplify the discrimination and tracking of dispersed drops in the flow.

To enhance light reflection in the oil drops and facilitate their identification, a white dye was added to the oil. The white dye also increased the contrast of the dispersed droplets against the dark background of the prototype pump, facilitating the investigation of the dispersed phase using PTV tools. This specific analysis for the dispersed phase was not carried out, as it is outside the scope of this doctoral work. However, the raw images generated in the work are available for future studies that could focus on evaluating the dynamics of these droplets.

Thus, a candle dye available in Brazil under the commercial name Saramanil was used to dye the oil, at a ratio of 1.0 g of dye for every 1.0 kg of oil. The presence of the dye, at a concentration of 0.1% by weight, did not significantly alter the physicochemical properties of the oil, as evaluated in additional tests conducted at the Flow Assurance Laboratory in CEPETRO.

Figure 3.9 presents a schematic of the PIV measurement system operating with two-phase flow (Fig.3.9a), and a raw PIV image of the two-phase oil-in-water flow in the centrifugal pump (Fig.3.9b, where oil droplets doped with white dye are visible).

As previously discussed, the two-phase experiments in this study exclusively utilized the automatic acquisition mode (dual-frame TR-PIV). The acquisitions were performed at a frequency of 700 Hz, capturing a total of 12,000 images for each experimental condition (Tab. 3.3), divided into three files. The substantial number of images captured for two-phase flow is attributed to their dual purpose: training neural networks and later describing the physics of flow under two-phase conditions.

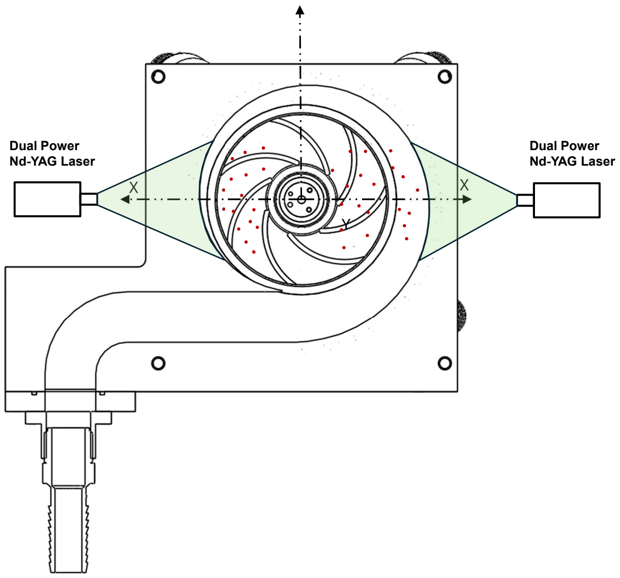

(A) scheme of the PIV measurement with two-phase flow

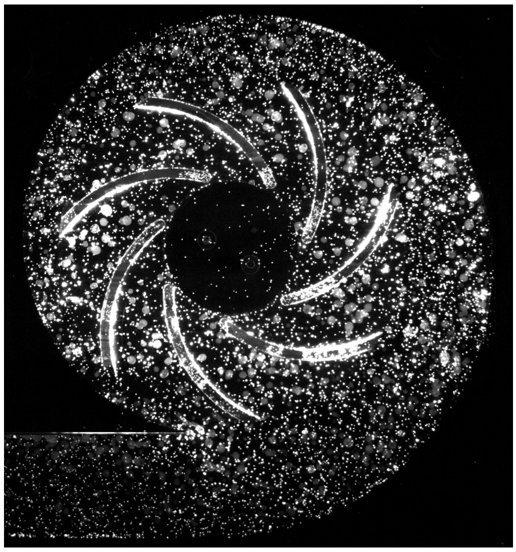

(B) raw PIV image of the two-phase oil-in-water flow

FIGURE 3.9 – PIV image acquired during two-phase tests.

4 Data processing

This chapter provides an overview of the procedures employed in processing PIV data. Section 4.1 provides a detailed account of single-phase data processing, specifying the image processing methodology, as well as the use of the cross-correlation technique. In Section 4.2, we explain the methods used to process two-phase data. This section presents the application of the deep learning U-Net technique, which was used in the detection and characterization of oil droplets in water.

4.1 Single-phase data processing

After the PIV data acquisition step following the procedure outlined in Sec. 3.4.2 within the *DynamicStudio 7.4* software, algorithms were developed to execute the pre-processing, processing, and post-processing stages of the data. These algorithms were in-house developed using the Matlab® and Python™ languages. Below, we provide a description of the procedures for creating the utilized codes.

The pre-processing stage begins with calibration, where a mathematical relationship between pixels and millimeters is established. Following this, MatLab®-generated masks are applied to the calibrated images to define the positions of the blades and the center of the impeller. Given that the research exclusively concentrates on the impeller, the primary objective of the masks is to exclude all extraneous areas, retaining solely the region of interest earmarked for analysis. Figure 4.1 demonstrates the application of a mask employed in this study to an unprocessed flow image.

After applying the mask, processing proceeds to eliminate the rotational motion of the impeller between frames of the same image pair. The procedure involves counterclockwise rotation of the image from the second frame, which opposes the displacement imposed by the angular speed (Ω) of the impeller (Liu *et al.*, 2021). This procedure provides instantaneous velocity fields with relative velocity vectors, $\mathbf{W}$, equivalent to using a rotating frame of reference

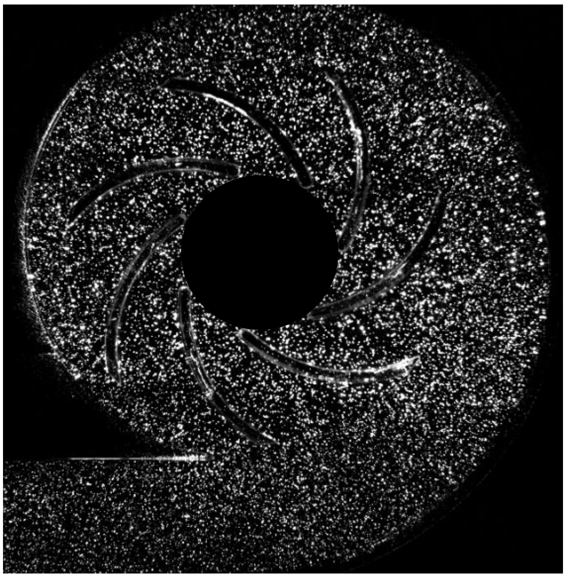

(A) PIV image before pre-processing

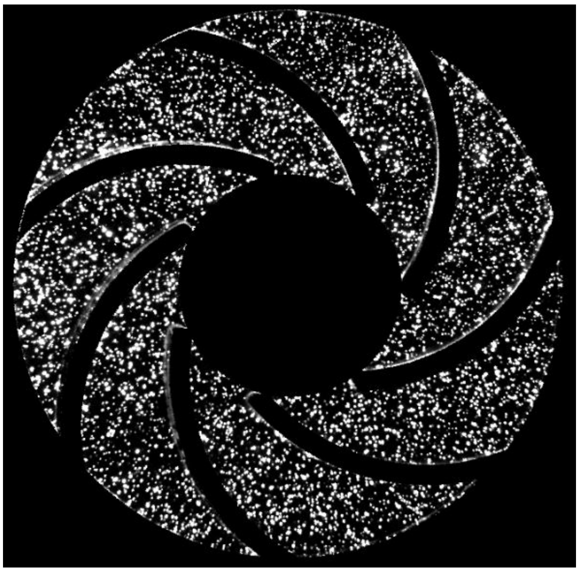

(B) PIV image after pre-processing

FIGURE 4.1 – Typical PIV images acquired during the tests (Fonseca *et al.*, 2023).

in the impeller. However, it is also possible to work with absolute velocity vectors, $\mathbf{U}$, within a fixed frame of reference. The difference between them lies in the angular velocity of the impeller, denoted as $\Omega \times \mathbf{r}$, where Ω and $\mathbf{r}$ represent vectors of angular speed and radial position.

The next step involves the application of min/max, arithmetic, and balancing filters with the purpose of enhancing images quality by reducing background noise and achieving a more homogeneous distribution of brightness in the bright areas. These filters increase the reliability of the calculations before employing PIV cross-correlation, which is used subsequently to calculate the instantaneous velocities within the interrogation windows of each image pair.

In order to conduct PIV measurements in turbulent flows, achieving the necessary spatial resolution to detect small-scale turbulence structures is paramount. To meet this requirement, the initial step involves minimizing the size of the interrogation windows where cross-correlation is computed.

We employed the adaptive PIV method (Scarano & Riethmuller, 1999) as the cross-correlation algorithm. This method determines the local displacement of each interrogation area based on a predictive flow pattern, which is inferred from a pair of previously examined images.

At the outset of the process, we assumed a lack of prior information about the flow pattern. Consequently, we uniformly set the initial predictor to zero, meaning no relative offset is applied. The size of the interrogation windows in this initial phase is determined following the one-quarter rule for in-plane movement (Raffel *et al.*, 2018).

Following this initial interrogation, the results from the coarser windows (indicated by solid line arrows and windows in Fig. 4.2) serve as predictors. To achieve higher resolution, we subdivided the windows in both dimensions and applied the predictor to adjust the window offset through straightforward substitution of the previous iteration's results.

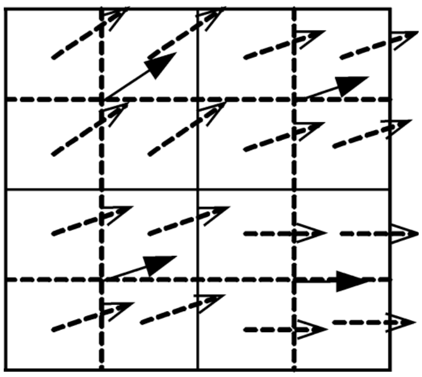

FIGURE 4.2 – Application of an interrogation result (solid line arrows) to build a finer predictor (dotted line arrows).

Consequently, in the subsequent stages, the one-quarter rule governing in-plane displacement no longer constrain the window size, allowing for improved image interrogation resolution.

Figure 4.3 displays two windows (4.3a) and (4.3b) extracted from two consecutive images. When estimating the displacement vector $\delta = (\delta x, \delta y)$, the interrogation area in the second image can be chosen with a relative offset (the gray area containing all the black-filled particles) to optimize the number of particle doublets.

It becomes evident that in the absence of such a strategy, the portion of particles contributing positively to constructing the signal peak remains confined to the gray patterned area. Consequently, the greater the displacement compared to the window's dimensions, the lower the signal-to-noise ratio in the correlation plane.

In this study, we performed the cross-correlation calculation using the *DynamicStudio* software, with initial and final interrogation regions set at 32 and 16 pixels, respectively. To achieve precise sub-pixel displacements, we incorporated Gaussian adjustments into the correlation peak. It is noteworthy that, despite the presence of an adaptive PIV processing module in the *DynamicStudio 7.4* program for velocity field calculations, we utilized in-house routines for pre-processing and optimizing the analysis of the PIV images obtained during the experiments.

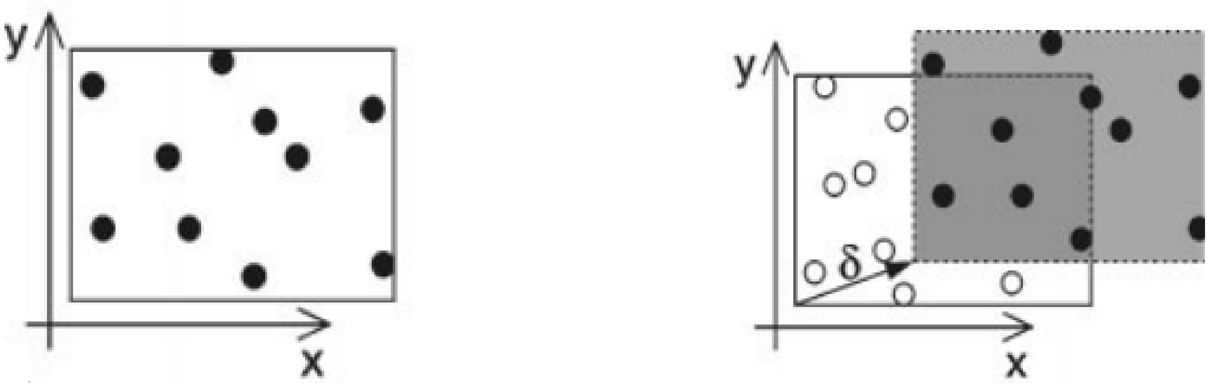

(A) image at time t (B) image at time $t + \Delta t$

FIGURE 4.3 – Principle of the window displacement (Scarano & Riethmuller, 1999).

The last step in processing involves determining the average of the instantaneous velocities. This calculation is performed using a known procedure, such as phase-ensemble averaging (Eq. 2.13), within an in-house code in MatLab®. Once the calculation of the average velocity field is complete, it is possible to export the data from MatLab® and import it into post-processing routines written in Python™. These routines were employed to create graphs and countour plots that enhance the clarity of the results.

Figure 4.4 presents an illustration of the adopted procedure and the respective programming languages used in each of the processes to obtain the results of single-phase flow.

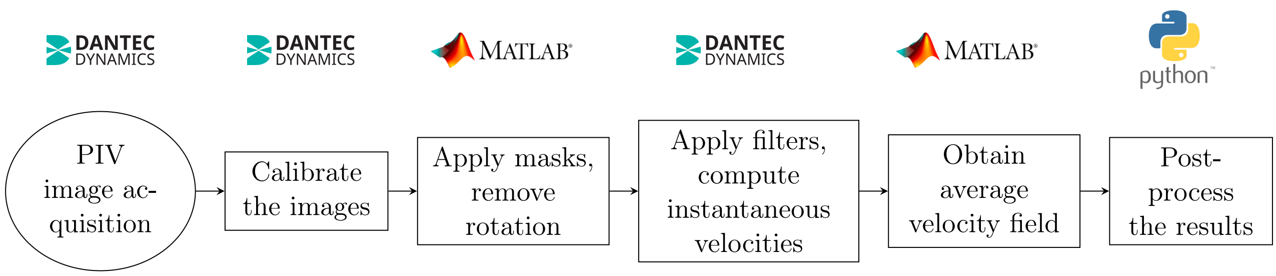

FIGURE 4.4 – PIV image processing steps for single-phase flow.

4.2 Two-phase data processing

In two-phase liquid-liquid flows, information about the dispersed phase is fundamentally important for characterizing the overall flow behavior. Therefore, it is crucial to collect experimental data capable of providing insights into local flow patterns, such as wakes and recirculation regions induced by liquid-liquid interactions. Furthermore, it is essential to provide average values for use in closure relationships, along with furnishing reliable data for the development and validation of CFD two-phase flow models.

To achieve this goal, the PIV technique has gained significant attention in recent years as a measurement technique for two-phase flows. This is attributed to its non-intrusive nature, reducing errors associated with flow probing—errors that are prominent in intrusive techniques.

The application of the PIV method in two-phase flows poses additional challenges due to the presence of interfaces between the phases, demanding increased effort compared to single-phase flows. This complexity is a notable hurdle in obtaining accurate measurements. To confront this challenge, our approach involves the integration of deep learning methods into image processing (Cerqueira & Paladino, 2021; Cerqueira *et al.*, 2023). This integration enhances the measurement precision for two-phase liquid-liquid flows within the centrifugal pump impeller.

Upon acquiring TR-PIV two-phase flow images (Sec. 3.5.2), a U-Net convolutional network is utilized to identify and accentuate the instantaneous contours of the drops in the flow images. This advanced image processing technique contributes to the accuracy and reliability of the data obtained in our study. The subsequent section of this work details the methodology employed for dispersed phase discrimination.

4.2.1 U-Net Model

The U-Net is a CNN architecture widely used in the field of image segmentation. It incorporates skip connections that facilitate the direct flux of information between corresponding encoder and decoder layers. This feature helps preserve spatial information during the downsampling and upsampling stages, thereby enhancing the network's ability to capture both global and local features. Furthermore, U-Net employs concatenation operations to merge feature maps, improving its capacity to capture complex patterns and enhance segmentation accuracy (Ronneberger *et al.*, 2015; Livne *et al.*, 2019).

The U-Net network goal here is to generate a binary mask highlighting oil droplets in TR-PIV images of the centrifugal pump impeller. This task can be viewed as a segmentation task, categorizing image pixels into two groups: one for the background and other for the foreground, representing the pixels occupied by visible oil droplets. In summary, the U-Net network processes input TR-PIV images, akin to those depicted in Fig. 4.5a, generating binary masks to eliminate droplets and yielding images according to those shown in Fig. 4.5b.

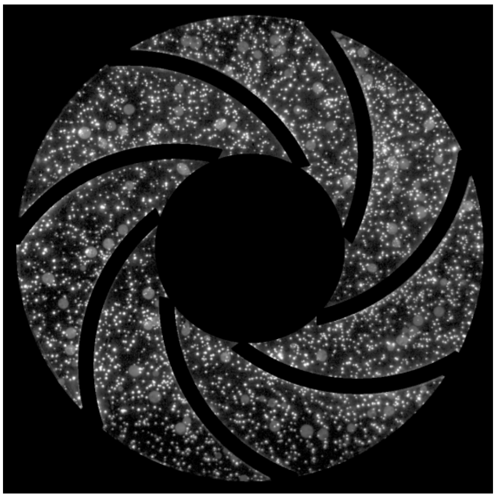

(A) PIV raw images of two-phase O/W dispersion

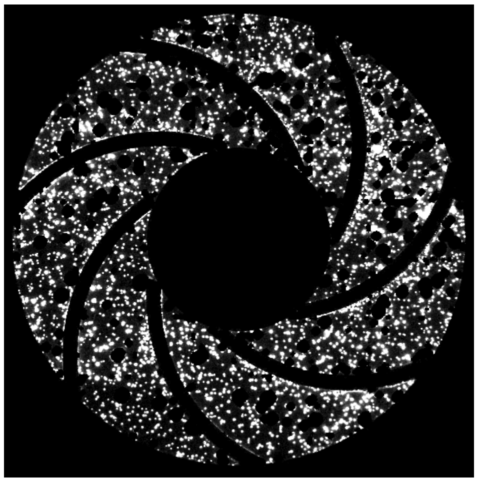

(B) deep learning-based processed image

FIGURE 4.5 – Comparison between a raw PIV image of the two-phase O/W flow and its processed version using a U-Net deep learning technique.

For training the U-Net convolutional network, the flow images obtained through PIV were labeled to construct the training datasets. The masks were manually generated using a simple graphical user interface (GUI) software developed by Cerqueira *et al.* (2023). This application allowed for approximating the contours of the oil drops as ellipsoids or, in some cases, as contours composed of a set of connected points. The GUI software incorporated a load/save module, enabling the storage of manually labeled droplet positions at any given time. This flexibility facilitated a quality check of the manual annotations, enabling the addition or removal of oil drops as needed. Table 4.1 illustrates the number of manually labeled images for each experimental condition.

Table 4.1 – Number of manually labeled masks to generate the U-Net model dataset.

$\mathcal{N}$ [rpm]	Q_w [m^3/h]	$Q^* = Q_w/Q_{BEP}$	U-Net images
	0.225	0.3	11
300	0.375	0.5	8
	0.525	0.7	8

The quality of the binary mask generated to mask the oil droplets in the flow depends on the architecture of the U-Net network. This architecture, in turn, relies on the weights and biases of the activation layers at each training stage of the network. The U-Net, with its contraption and expansion paths are illustrated in Fig. 4.6. A hyperparameter analysis, aimed at determining the optimal set of kernel sizes and the number of filters for each activation layer to minimize the U-Net loss function, is detailed in Cerqueira *et al.* (2023).

As depicted in Fig. 4.6, the primary architecture of the utilized U-Net network comprises 14 convolutional layers, along with 3 pooling, and 3 transposed convolution operators. The initial images obtained through TR-PIV possessed dimensions of 2560×1600 pixels. To address memory constraints during U-Net network training, these images were partitioned into 16 sub-images, each with dimensions of 384×384 pixels. Therefore, when generating the binary masks, it was necessary to regroup the output of the U-Net network into a single image.

In the current study, both the U-Net model and image processing algorithms were developed using the Python™ programming language. Image processing routines were implemented with the OpenCV library (Bradski, 2000). For the creation of the U-Net, the Keras framework (Gulli & Pal, 2017) with the Tensorflow backend (Abadi *et al.*, 2015) was employed. This development setup mirrors that utilized in Cerqueira's work.

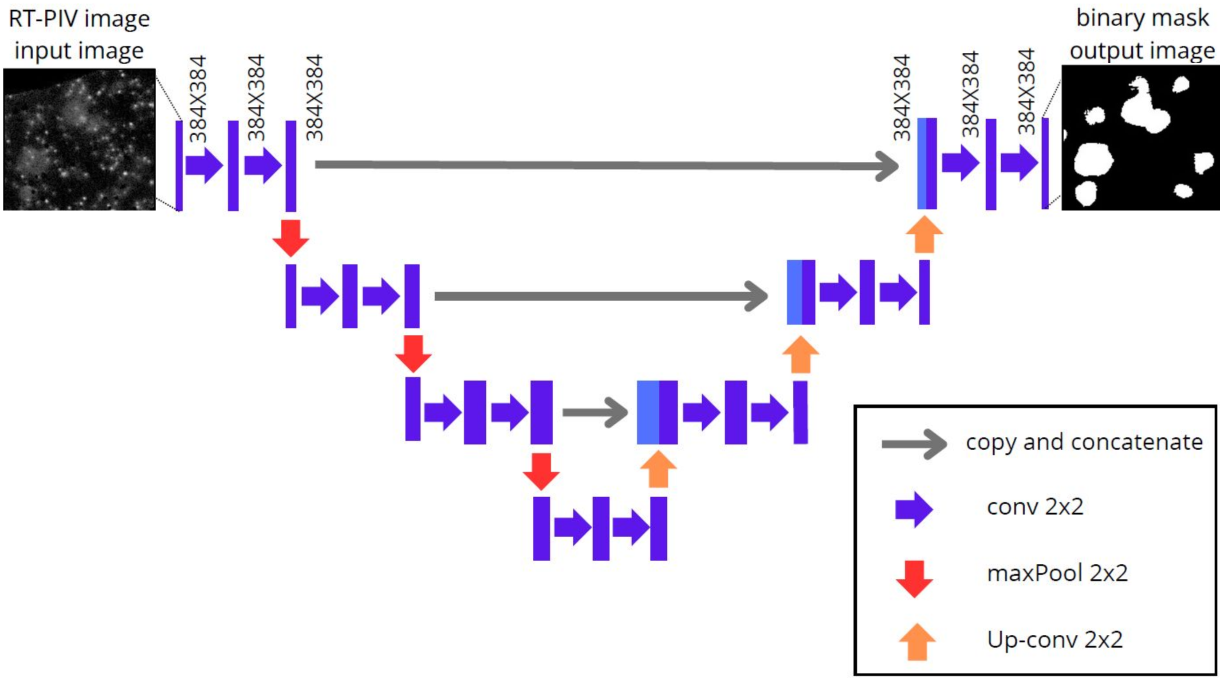

FIGURE 4.6 – U-Net architecture illustration. The U-Net shown is an encoder-decoder network with a contracting path (encoding part, left side) that reduces the height and width of the input images and an expanding path (decoding part, right side) that recovers the original dimensions of the input images. The arrows represent the different operations listed in the legend on the right. The image dimensionality (xy size) is indicated on the edge next to the boxes that represent the images.

5 Single-phase flow results

In this chapter, the results for the centrifugal pump impeller operating with single-phase flow will be presented[1]. The adoption of the experimental program described in Chapter 3 and the procedures outlined in Sec. 4.1 made it possible to obtain two sets of data: i) triggered mode and ii) automatic mode. The data obtained in the triggered mode were used to characterize average flow parameters, such as relative velocity, vorticity, turbulent kinetic energy (TKE), turbulence production and dissipation, as well as hydraulic losses in the impeller. The data obtained in the automatic mode (TR-PIV) were used to describe the unstable characteristics of the flow through a POD analysis.

5.1 Phase-ensemble averaged velocity fields

To investigate flow patterns within the centrifugal pump impeller, the instantaneous fields of absolute velocity were averaged through a phase-ensemble procedure. In this procedure, acquisitions are only performed when the impeller reaches a certain angular position (θ) during its rotational motion. Therefore, when observing the images, the observer notices that the channels and blades are always in the same position. In this work, the results presented for average flow fields are positioned at $\theta = 10°$, with the reference position $\theta = 0°$ corresponding to the angle at which the tip of one of the lowest blades is vertically aligned with the tip of the volute tongue. This position was calculated using a rotary encoder. The phase-ensemble averaged absolute velocity was determined using Eq. (5.1):

$$\langle \mathbf{U} \rangle = \frac{1}{N} \sum_{i=1}^{N} \langle \mathbf{U}_i \rangle \tag{5.1}$$

The relative velocity was obtained by subtracting the absolute velocity from the tangential term due to the impeller motion in the velocity triangle (Gülich, 2008):

$$\langle \mathbf{W} \rangle = \langle \mathbf{U} \rangle - \Omega \mathbf{r} \tag{5.2}$$

[1]This chapter is based on the results presented in Fonseca *et al.* (2023, 2024).

where Ω represents the angular speed and $\mathbf{r}$ is the radial position of the velocity vector in relation to the impeller center.

The results of the fields of phase-ensemble averages of the relative velocity and streamline plots are shown in Fig. 5.1 for fixed pump impeller rotational speeds ($\mathcal{N}$) of 300, 600 and 900 rpm under the different flow rates (Q^*) of 0.3, 1.0 and 1.5, as indicated in Tab. 3.2. The impeller rotation direction is clockwise, and the relative velocities presented have been normalized by the blade tip speed $\langle W^* \rangle = \langle W \rangle / U_{tip}$ (Keller *et al.*, 2014).

As can be seen from Figs. 5.1b, 5.1e and 5.1h, at the BEP ($Q^* = 1.0$) the streamlines follow the curvature of the blades without significant flow separation for the three investigated rotational speeds. Low velocity zones develop on the pressure sides of the blades, generating an pressure gradient, which suggests that the fluid is displaced towards the suction sides. As a consequence, we observe the "jet-wake" phenomenon in the suction blades of all impeller channels. Furthermore, due to the blade curvature, the flow near the impeller center is dominated by rotational effects. As the fluid moves towards larger radii, the Coriolis force increases and the fluid is pushed in the opposite direction, towards the pressure side. As a result of this phenomenon, we can identify very uniform velocity fields in the impeller exit region.

As the flow rate increases to $Q^* = 1.5$ (Figs. 5.1c, 5.1f and 5.1i), the formation of small flow instabilities is detected on the pressure side of the blades in different radial positions of the impeller, which is probably due to the detachment of the boundary layer caused by an adverse pressure gradient. In addition, the presence of intense jets on the suction blades is also observed, as the streamlines are distorted and acquire a shape comparable to half a counter-clockwise vortex.

In the condition corresponding to the lowest flow rate, $Q^* = 0.3$ (Figs. 5.1a, 5.1d, and 5.1g), it is possible to identify that the fluid near the suction blade is diverted to the pressure blade, causing a change in the stagnation point as a consequence of the unbalance of apparent forces. Subsequently, a significant reduction in velocity is detected, resulting in recirculation zones next to the suction blades. It is observed that this vortex generation mechanism is closely linked to regions where the fluid outlet area is reduced by the solid walls in the volute spiral, especially on the left side of the pump stage. Meanwhile, the channels farther from it present a flow topology without this type of structure. The most relevant differences are observed between channels 1 and 5, according to Fig. 5.1a. This nomenclature considers 1 to be the channel closest to the volute tongue, and then the number assigned to each channel increases counterclockwise, until 7.

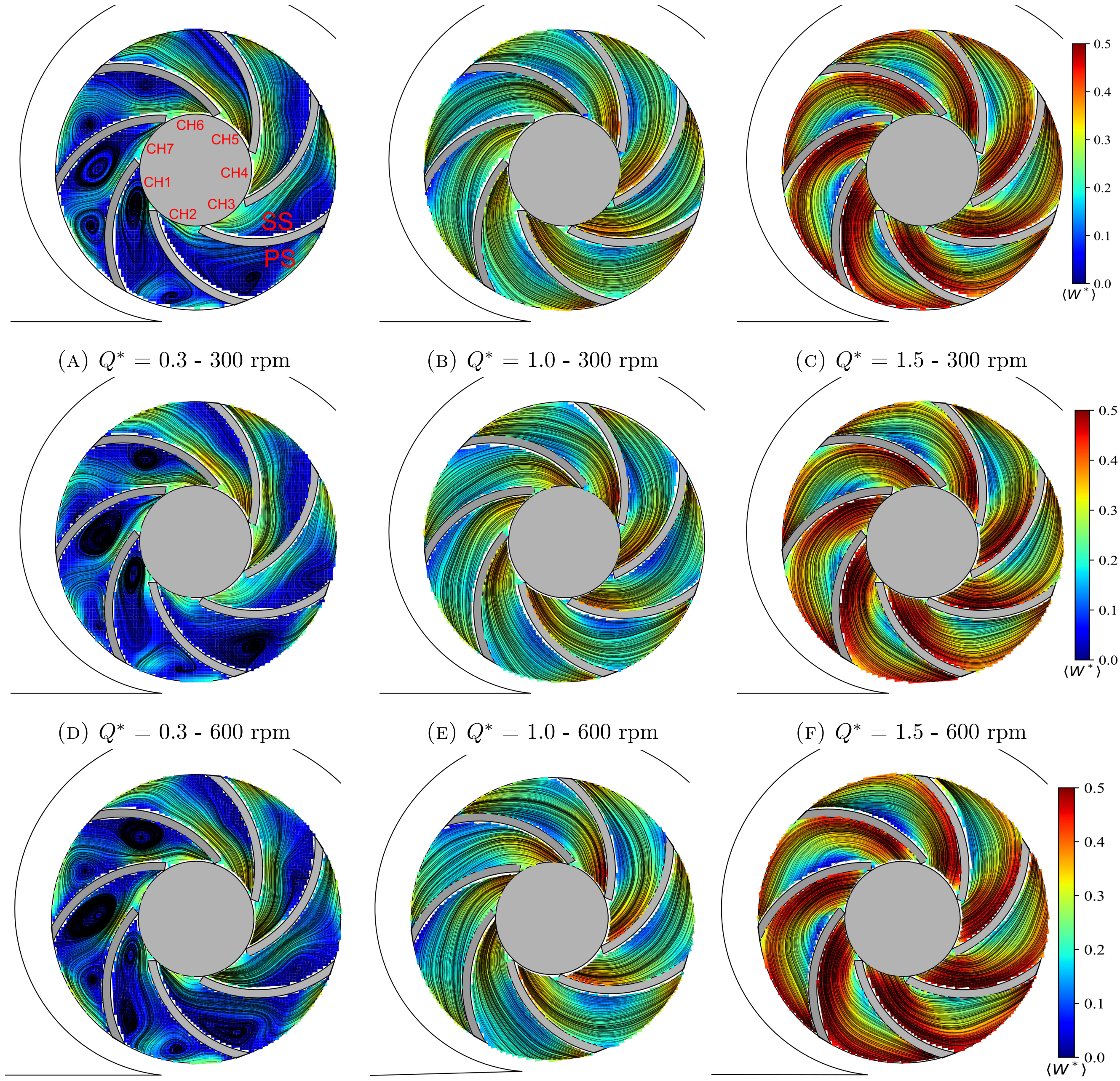

(A) $Q^* = 0.3$ - 300 rpm (B) $Q^* = 1.0$ - 300 rpm (C) $Q^* = 1.5$ - 300 rpm

(D) $Q^* = 0.3$ - 600 rpm (E) $Q^* = 1.0$ - 600 rpm (F) $Q^* = 1.5$ - 600 rpm

(G) $Q^* = 0.3$ - 900 rpm (H) $Q^* = 1.0$ - 900 rpm (I) $Q^* = 1.5$ - 900 rpm

FIGURE 5.1 – Streamlines from ensemble-average velocity field in the centrifugal pump impeller (Fonseca *et al.*, 2023).

In this context, Fig. 5.2 presents velocity profiles at different radii of the impeller [$0.5r_{\text{out}}$, $0.7r_{\text{out}}$, $0.9r_{\text{out}}$]. Furthermore, Fig. 5.3 illustrates blade-to-blade distributions of phase-averaged relative velocities for channels 1 and 5 along the same three radial positions. Both sets of results are provided for all three flow rates at a constant rotational speed of 600 rpm. On the x-axis of the graphs (Fig. 5.3), the circumferential position is normalized, $c^* = (c - c_{SS})/(c_{PS} - c_{SS})$, where $c^* = 0.0$ corresponds to the surface of the suction blade (SS) and $c^* = 1.0$ represents the surface of the pressure blade (PS) within each channel.

Upon conducting a comparative analysis between channels 1 (Figs. 5.3a, 5.3c, 5.3e) and 5 (Figs. 5.3b, 5.3d, 5.3f), pronounced distinctions emerge, mainly at $Q^* = 0.3$ condition. In the channel situated closest to the volute tongue (channel 1), under low flow rates, it becomes evident that the inflection regions of the velocity curves coincide with the zones where vortices manifest themselves (refer to Fig. 5.1). It is worth noting that this behavior assumes a more pronounced character when dealing with smaller impeller radii. Nevertheless, at the design ($Q^* = 1.0$) and highest flow rate ($Q^* = 1.5$) conditions, the velocity distribution trends exhibit remarkable similarity, especially in the channel farthest from the volute tongue (channel 5). For both channels, we can also observe that the magnitude of the relative velocity increases as the flow rate increases. The underlying cause of this phenomenon, as expounded upon by Perissinotto *et al.* (2023), stems from the relationship between the flow rate and radial component of the relative velocity vectors.

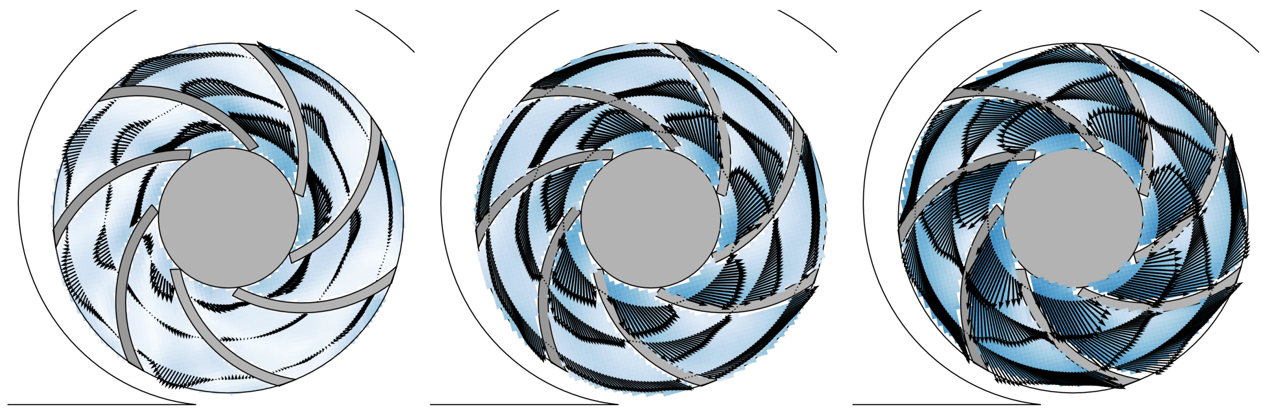

(A) $Q^* = 0.3$ (B) $Q^* = 1.0$ (C) $Q^* = 1.5$

FIGURE 5.2 – Velocity profiles in the centrifugal pump impeller at 600 rpm (Fonseca *et al.*, 2024).

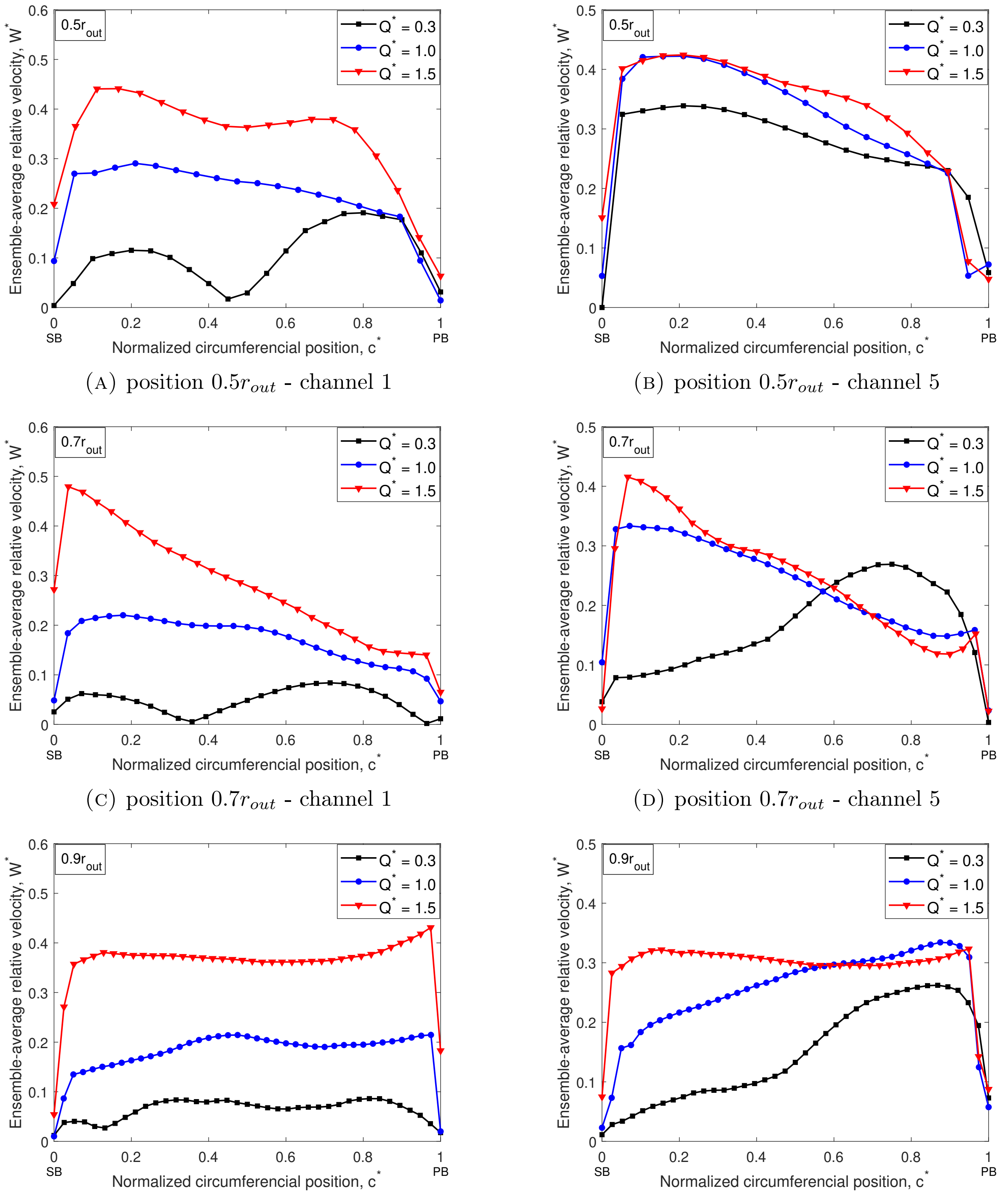

(A) position $0.5r_{out}$ - channel 1

(B) position $0.5r_{out}$ - channel 5

(C) position $0.7r_{out}$ - channel 1

(D) position $0.7r_{out}$ - channel 5

(E) position $0.9r_{out}$ - channel 1

(F) position $0.9r_{out}$ - channel 5

FIGURE 5.3 – Profiles of normalized relative velocity in two channels of the impeller (Fonseca *et al.*, 2024).

5.2 Phase-ensemble averaged vorticity fields

As PIV enables the acquisition of a comprehensive velocity field, it offers the opportunity for further processing and computing the vorticity field. Given that the flow in our experimental setup is predominantly two-dimensional, only the out-of-plane component of the vorticity can be computed, and the phase-averaged out-of-plane component is defined as:

$$\omega_3 = \frac{\partial \langle W_2 \rangle}{\partial x_1} - \frac{\partial \langle W_1 \rangle}{\partial x_2} \tag{5.3}$$

To compute the partial derivatives of the relative velocity components, centered finite difference formulas were used. Subsequently, in accordance with the approach introduced by Keller *et al.* (2014), we define a normalized vorticity, denoted as ω^*, by dividing the vorticity ω_3 by the impeller's solid rotation, characterized by an intensity of 2Ω.

Based on the analysis depicted in Figs. 5.1b, 5.1e and 5.1h it is apparent that the streamlines show a uniform distribution, indicating the absence of noticeable vortices when the pump operates under the design flow condition ($Q^* = 1.0$). This observation suggests that the flow within the impeller remains relatively stable. Nonetheless, as depicted in Figs. 5.4b, 5.4e and 5.4h, localized areas of positive vorticity arise near the rotor eye and the pressure blades, positioned in channels distant from the volute tongue. This occurrence can be attributed to the impeller rotational motion. When the flow rate diminishes to $Q^* = 0.3$, the average flow velocity within the impeller decreases and backflow near the volute tongue surfaces generates an irregular distribution of vortices induced by fluid viscosity, as discussed in Lu *et al.* (2022). The interaction between the rotating impeller and stationary volute gives rise to a substantial region of backflow and secondary flow, particularly at the tongue region. This interaction manifests as alternating regions of positive and negative vorticity values, as illustrated in the vorticity fields (Figs. 5.4a, 5.4d and 5.4g). Notably, the channels in close proximity to the tongue (adjacent to channel 1) exhibit a higher likelihood of generating irregular vortices, recirculation, and secondary flow. Finally, under the high flow rate $Q^* = 1.5$, the distribution of vorticity along the impeller exhibits a relatively uniform pattern across all channels. In this scenario, the central regions display positive vorticity, while the blade surfaces showcase negative vorticity, as depicted in Figs. 5.4c, 5.4f and 5.4i. As previously discussed, these conditions give rise to instabilities in the boundary layer of the blade surfaces, leading to flow separation and subsequently the formation of small-scale eddies.

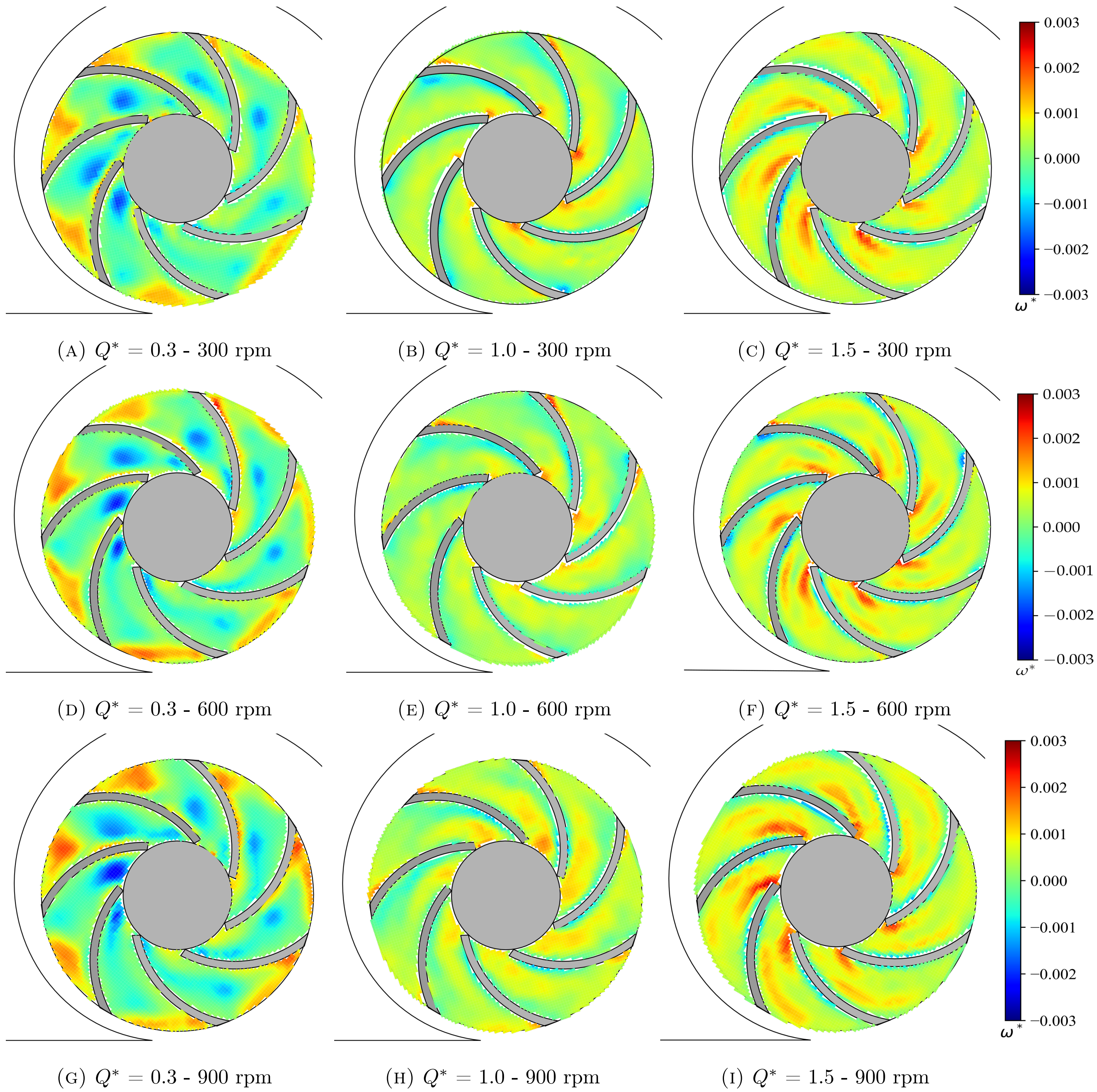

(A) $Q^* = 0.3$ - 300 rpm (B) $Q^* = 1.0$ - 300 rpm (C) $Q^* = 1.5$ - 300 rpm

(D) $Q^* = 0.3$ - 600 rpm (E) $Q^* = 1.0$ - 600 rpm (F) $Q^* = 1.5$ - 600 rpm

(G) $Q^* = 0.3$ - 900 rpm (H) $Q^* = 1.0$ - 900 rpm (I) $Q^* = 1.5$ - 900 rpm

FIGURE 5.4 – Normalized vorticity fields in the centrifugal pump impeller (Fonseca *et al.*, 2024).

For all impeller rotations analyzed ($\mathcal{N} = 300$, 600, and 900 rpm), the vorticity distribution is practically identical when considering the same flow rate in relation to the BEP. The main difference between flow conditions at the same non-dimensional flow rate for different rotations lies in the magnitude of vorticity (ω_3), which follows the trend of increasing rotation $\mathcal{N}$ and velocities $\langle U_1 \rangle$ and $\langle U_2 \rangle$.

5.3 Phase-ensemble averaged TKE fields

Turbulent kinetic energy is crucial for analyzing the energy distribution within a flow field. In 2D2C-PIV measurements, only the x and y components of the velocity fluctuations are captured. Consequently, TKE is calculated using these two components according to Eq. (2.21), which is reproduced here for the reader's convenience:

$$k_{2D} = \frac{1}{2}\langle u_i u_i \rangle$$

The results for the phase-ensemble averaged turbulent kinetic energy are presented in Fig. 5.5 normalized by the blade tip velocity $K^*_{2D} = K_{2D}/U^2_{tip}$. Figure 5.5 reveals that the highest turbulence values are detected at the lowest flow rate condition, $Q^* = 0.3$ (Fig. 5.5a, 5.5d and 5.5g), especially near the impeller exit. This fact occurs because when the fluid flows through the impeller, not only rotational energy is provided to it, but also the volute itself imposes a geometric restriction. Thus, the highest values of K^*_{2D} are located at the leftmost impeller, in channels 1, 6 and 7, which are close to regions where the volute radius is small. Exiting the impeller, the fluid impinges the volute wall and suddenly changes its direction, this fact resulting in the formation of recirculation zones in the impeller channels. In addition, the flow exiting the impeller in channels 1 and 2 is affected by the presence of the volute tongue. In this region, as the fluid exits the impeller, it faces a sudden change of direction due to the sharp surface of the tongue tip, which promotes recirculation. Those two effects combined result locally in regions with intense turbulent kinetic energy.

In opposition, for the design condition ($Q^* = 1.0$ Figs. 5.5b, 5.5e and 5.5h) the TKE production has much lower values. The limited K^*_{2D} values are associated with the uniformity of the flow field, since centrifugal pumps working at the BEP tend to have well-organized velocity fields without flow detachment zones. This is a consequence of well-balanced forces governing the fluid behavior in the impeller at the design point.

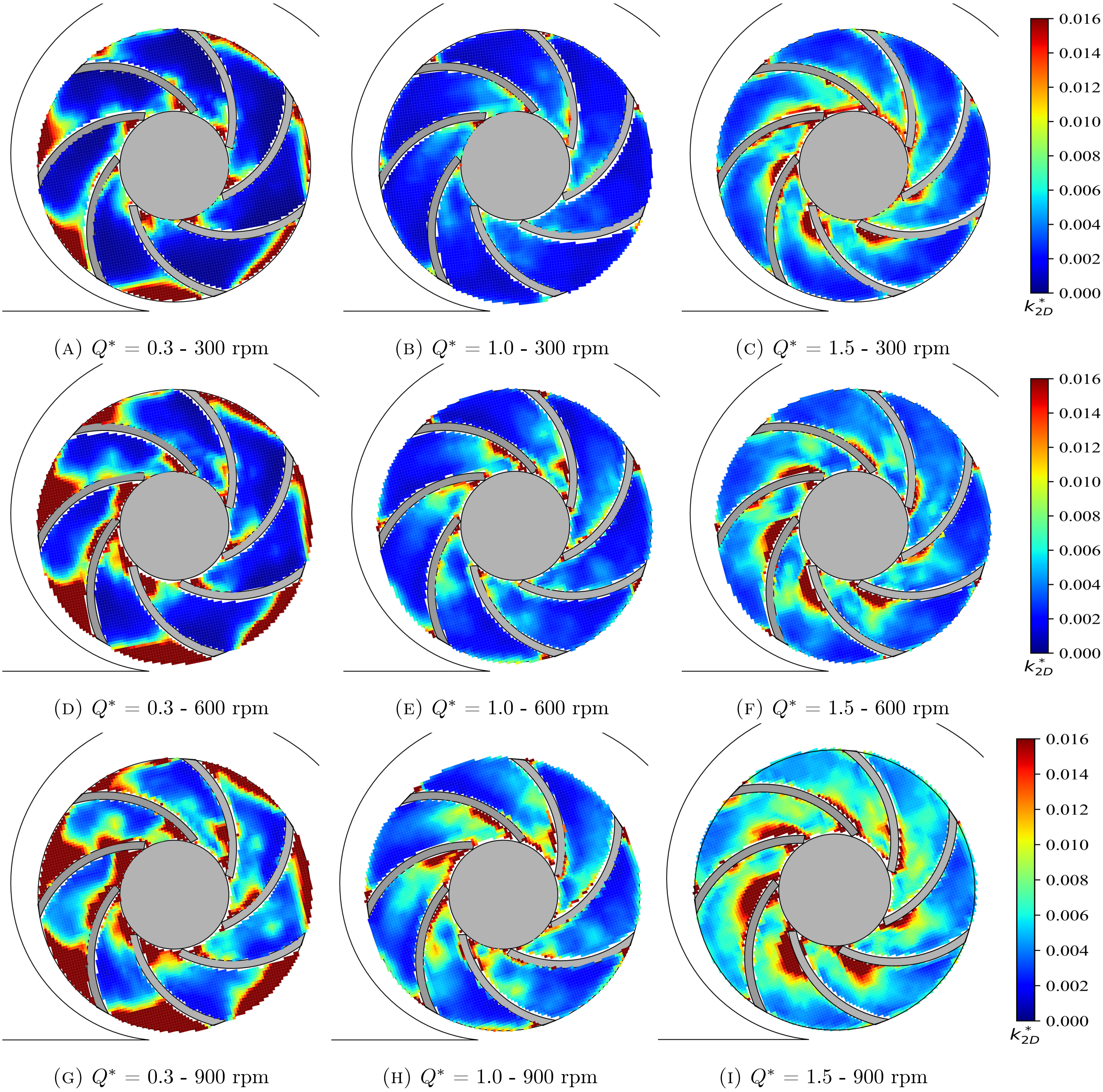

(A) $Q^* = 0.3$ - 300 rpm (B) $Q^* = 1.0$ - 300 rpm (C) $Q^* = 1.5$ - 300 rpm

(D) $Q^* = 0.3$ - 600 rpm (E) $Q^* = 1.0$ - 600 rpm (F) $Q^* = 1.5$ - 600 rpm

(G) $Q^* = 0.3$ - 900 rpm (H) $Q^* = 1.0$ - 900 rpm (I) $Q^* = 1.5$ - 900 rpm

FIGURE 5.5 – Normalized fields of ensemble-average turbulent kinetic energy in the centrifugal pump impeller. Adapted from Fonseca *et al.* (2023).

For higher flow conditions (such as $Q^* = 1.5$, Figs. 5.5c, 5.5f and 5.5i) we observe that regions with high values of turbulent kinetic energy are found near the pressure surfaces of the blades. As discussed in Sec. 5.1, these regions are characterized by low average velocities, which suggests the occurrence of flow detachment events.

Additionally, it is evident that, for all assessed cases, there is a generation of turbulent kinetic energy in proximity to the impeller inlet, extending along the suction blades. This phenomenon can be attributed to the turbulence induced by the pre-rotation of the flow. As the fluid exits the pump casing and enters the impeller eye, it undergoes a rapid change in direction. This abrupt redirection results in the generation of turbulence in the vicinity of the impeller inlet. Moreover, it is observed that an increase in rotation corresponds to an augmentation in turbulent kinetic energy values for a same flow rate relative to the BEP. Nevertheless, the TKE distribution over the impeller plane exhibit similarity when assessed under the same flow rate for varying rotations.

5.4 POD analysis

Physical quantities of turbulent flows can be divided into time-averaged and fluctuation quantities, the latter consisting of periodic and stochastic parts. The periodic part represents the large-scale coherent structures, while the stochastic part represents the small-scale turbulence (Yuan *et al.*, 2021). The POD method is as an effective tool to identify the fluctuation part, in which two key quantities are obtained: the eigenvalues (λ_k) and the modes (ϕ_k). The modes represent different structures of the flow field, and the eigenvalues are related to the flow field energy.

In this work, the spatial modes as well as the temporal coefficients are numerically obtained. An in-house code was developed in Python™, based on Weiss (2019). The code reads the PIV instantaneous velocity fields and performs the modal decomposition of the flow using the POD snapshot technique, as indicate in the `algorithm` 1. The code is based on the numerical packages `scipy` (Virtanen *et al.*, 2020) and `numpy` (Charles *et al.*, 2020), and is available for download[2] together with post-processing scripts and experimental data from this work.

[2]`http://gitlab.com/rafacerq/snapshot-POD`.

5.4.1 Distribution of flow energy

Figure 5.6 shows the distribution of the turbulent kinetic energy ($\lambda_n / \sum_{i=1}^{N} \lambda_i$) associated with individual modes of the eigenvalues spectrum (LHS), and the cumulative energy ($\sum_{i=1}^{n} \lambda_n / \sum_{i=1}^{N} \lambda_i$, on the RHS) for the various rotational speeds and flow rates in the pump impeller. For the lowest flow rate ($Q^* = 0.3$), 40 to 50% of the turbulent energy of the flow is concentrated in the first and second POD modes for the three $\mathcal{N}$ investigated here. For the design condition ($Q^* = 1.0$), the first two modes are responsible for 10% of the turbulent energy, with 60 modes being necessary to reach 50% of the total energy. Finally, for the highest flow rate ($Q^* = 1.5$), 20%, 9% and 12% of the cumulative energy are contained in the first two modes at rotation speeds of 300, 600 and 900 rpm, respectively. These distributions of energy level indicate that there is a significant redistribution to POD modes for different flow rates. However, the distribution of turbulent kinetic energy for a same flow rate in relation to the BEP is approximately the same for the different rotational speeds imposed on the impeller.

The rapid decrease in the energy levels for $Q^* = 0.3$ indicates that the first two modes may contain large-scale coherent structures of turbulent fields. Looking at the first few modes for this condition would be sufficient to identify dominant coherent motions. Furthermore, the third and fourth modes, which contain less energy, would represent the small-scale flow structure. As the modes continue to increase, the energy level changes little, so that it can be understood that the higher-order modes represent random fluctuations and noise in the turbulent field.

For the design ($Q^* = 1.0$) and higher ($Q^* = 1.5$) flow rates, the large-scale and coherent flow structures become more incoherent and smaller. This suggests that the large-scale structures (with higher energy) are broken into small-scale structures (with lower energy), in a process known in turbulence theory as cascade effect (Pope, 2000).

As mentioned above, the distribution of turbulent energy is approximately independent of the pump rotation speed, being a function only of the flow rate. This observation is confirmed in Figs. 5.1, 5.4, and 5.5, where we can see that the flow topology is very similar for 300, 600, and 900 rpm, with differences only in the magnitudes of the values. Hence, the next sections will focus only on the intermediate rotational speed $\mathcal{N} = 600$ rpm, while other rotations will be suppressed since they do not add new information to the discussions. Nevertheless, the analysis was performed for 300 rpm and 900 rpm as well, and we noticed that the results are roughly the same.

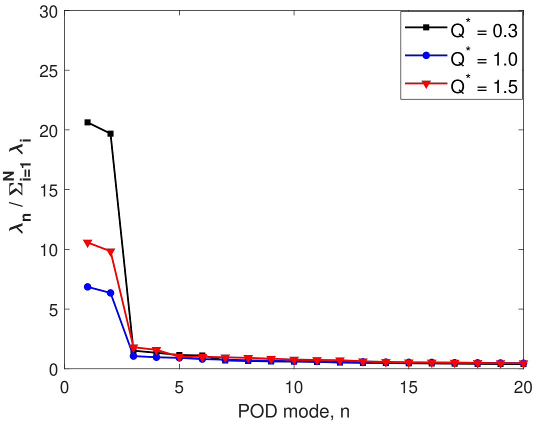

(A) normalized energy of the modes - 300 rpm

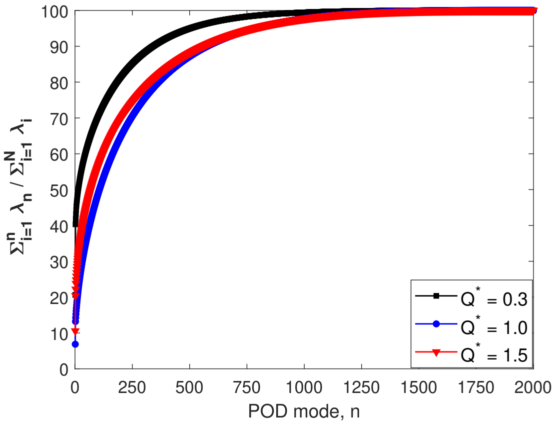

(B) cumulative energy of the modes - 300 rpm

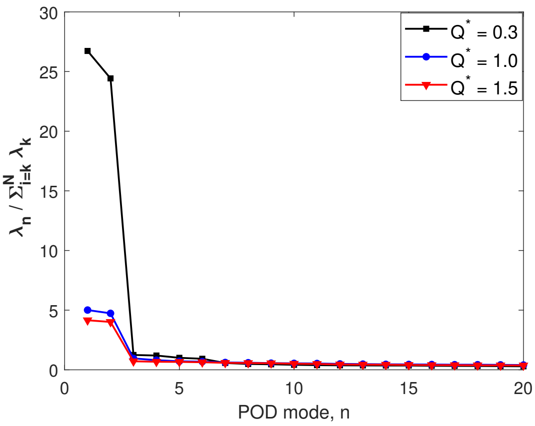

(C) normalized energy of the modes - 600 rpm

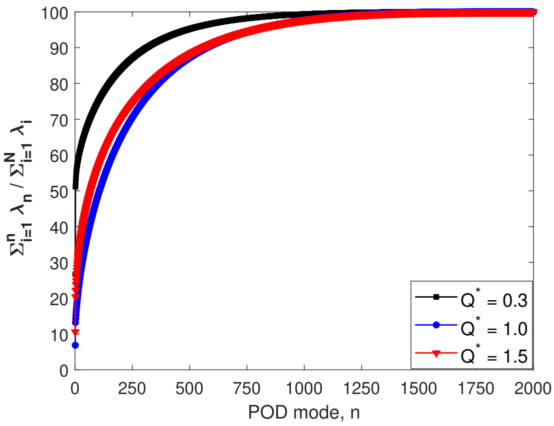

(D) cumulative energy of the modes - 600 rpm

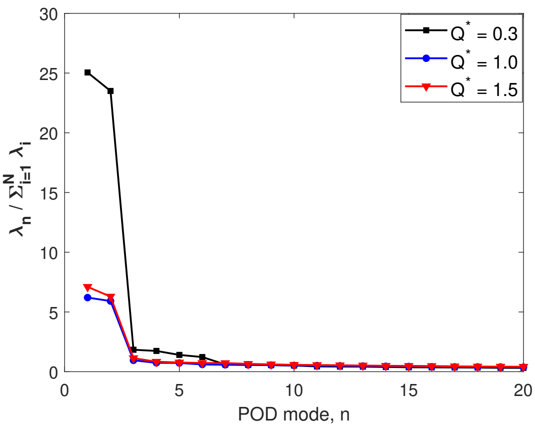

(E) normalized energy of the modes - 900 rpm

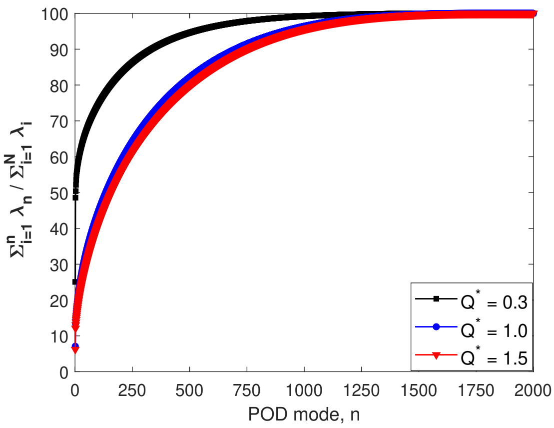

(F) cumulative energy of the modes - 900 rpm

FIGURE 5.6 – Energy distribution in the centrifugal pump impeller (Fonseca *et al.*, 2023).

5.4.2 Spatial characteristics

The spatial distribution of the first two POD modes is shown in Fig. 5.7 for the three studied flow rates at a rotation speed of 600 rpm. It can be observed that there is a coupling between the first two modes, with their spatial distribution revealing that these modes occur in pairs. Indeed, when comparing Fig. 5.7a with Fig. 5.7b, Fig. 5.7c with Fig. 5.7d, and Fig. 5.7e with Fig. 5.7f, we notice that the structure of both modes is the same, except for a shift in phase, as if mode 2 is rotated a certain angle relative to mode 1. This fact will be discussed in Sec. 5.4.3.

At the lowest flow rate ($Q^* = 0.3$), we observe regions with more intense reddish tones, where vortices or flow separation are found (Fig. 5.7a and 5.7b). This means that the velocity fluctuations in these regions tend to be correlated. From Fig. 5.1, we can see that the streamlines for this condition are completely misaligned in relation to the blades curvature, and, when analyzing regions far from the volute tongue, we notice that the flow that tends to separate. In the region near the volute tongue, large-scale vortices develop and rotate in the opposite direction with respect to the impeller motion, which is a effect resulting from the direct flow (related to the flow rate) and the counter-rotating flow (resulting from the fluid tending to keep its angular momentum, as discussed in Zhang *et al.* (2018)). These unsteady flow structures are detected by the POD method as coherent structures with a high energy level.

For the design condition ($Q^* = 1.0$), Fig. 5.1 revealed smooth streamlines and "jet-wake" zones. When analyzing the POD modes (Figs. 5.7c and 5.7d), we can observe that the velocity fluctuations for such a condition tend to be more correlated in regions where "jet-wakes" are present. However, these fluctuations are less correlated in comparison with those found at the lowest flow rate. As already discussed in Sec. 5.4.1, this is an indication that a large-scale flow with high energy is breaking into small-scale flow structures.

As the flow rate increases to $Q^* = 1.5$, we can see in Fig. 5.6 that the average values of the first two POD modes are approximately equal to those presented for $Q^* = 1.0$. These results are associated with the flow structures shown in Figs. 5.1. At the BEP condition, the streamlines are smooth and aligned with the curvature of the blades, so that the velocity fluctuations are very low. For $Q^* = 1.5$, however, the streamlines become inclined in the vicinity of the pressure blades, which generate velocity fluctuations interpreted here as a detachment of the boundary layer. These detaching streamlines are a consequence of small instabilities, which are characterized by structures of lower energy, represented in Figs. 5.7e and 5.7f as yellow and orange colors.

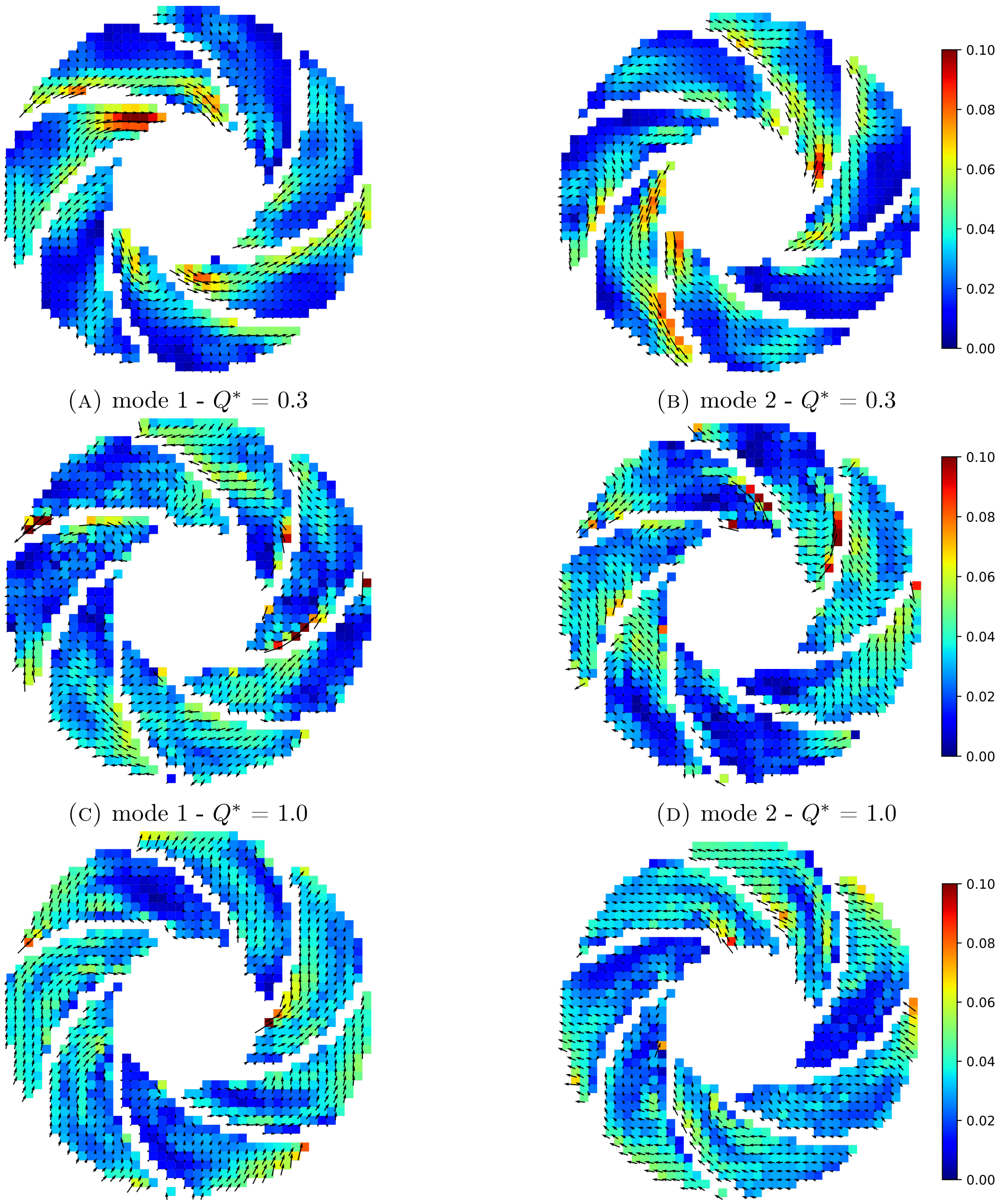

(A) mode 1 - $Q^* = 0.3$ (B) mode 2 - $Q^* = 0.3$

(C) mode 1 - $Q^* = 1.0$ (D) mode 2 - $Q^* = 1.0$

(E) mode 1 - $Q^* = 1.5$ (F) mode 2 - $Q^* = 1.5$

FIGURE 5.7 – Spatial distribution of the first and second modes at 600 rpm for different flow rates. Adapted from Fonseca *et al.* (2023).

The analysis is repeated for modes 3 and 4 in Fig. 5.8, for the same pump operating conditions.

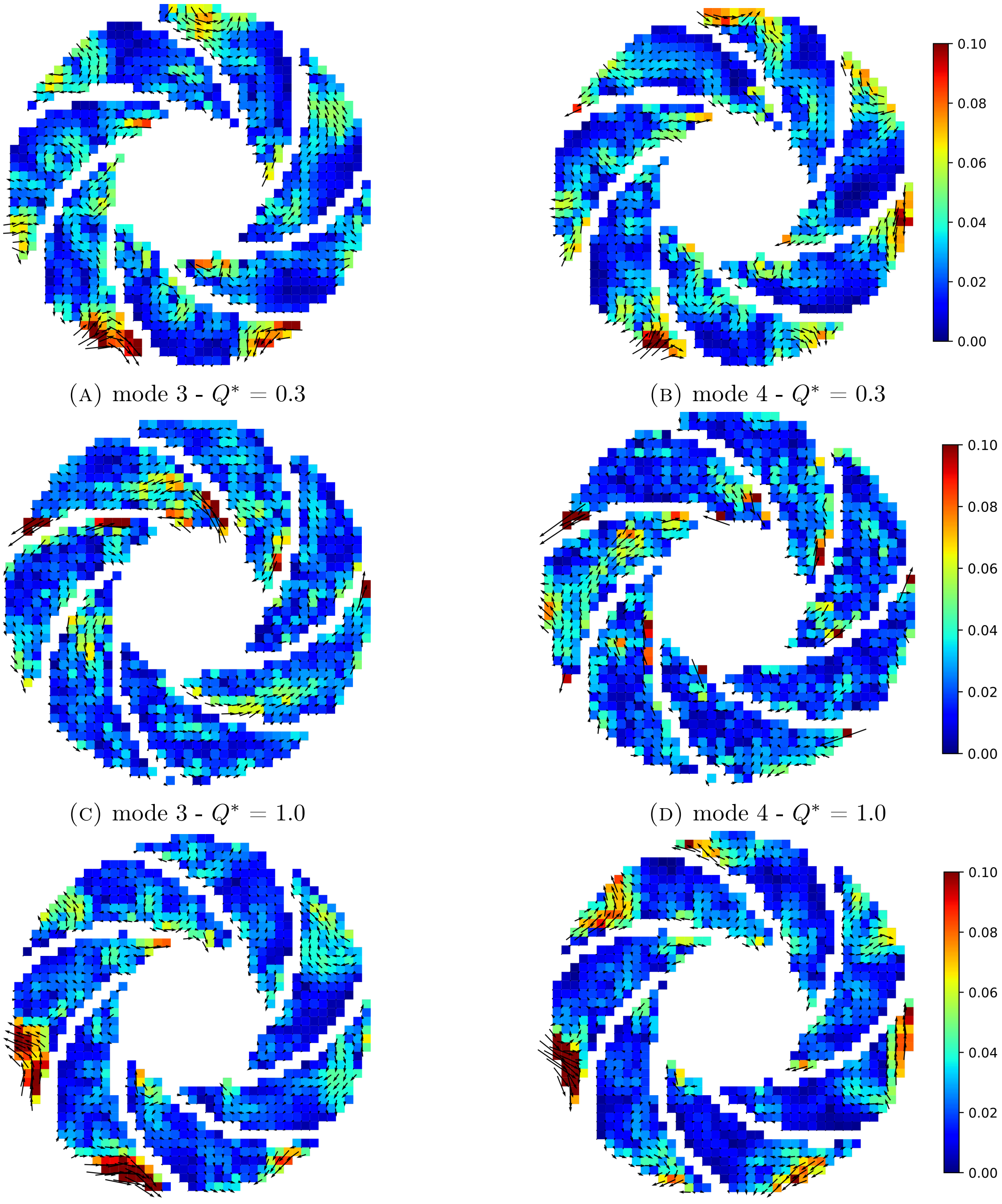

(A) mode 3 - $Q^* = 0.3$ (B) mode 4 - $Q^* = 0.3$

(C) mode 3 - $Q^* = 1.0$ (D) mode 4 - $Q^* = 1.0$

(E) mode 3 - $Q^* = 1.5$ (F) mode 4 - $Q^* = 1.5$

FIGURE 5.8 – Spatial distribution of the third and fourth modes at 600 rpm for different flow rates. Adapted from Fonseca *et al.* (2023).

The contours for $Q^* = 0.3$ in Fig. 5.8 show correlated zones of velocity fluctuation in the fluid leaving the impeller to the volute. In addition, we can also observe that modes 3 and 4 present characteristics of a vortex shedding flow pattern, process responsible for the unstable flow separation. Thus, these results indicate that modes 3 and 4, at this low flow rate, are associated with flow structures exiting the impeller as well as large-scale structures breaking into small-scale structures.

For the design condition, it is more difficult to associate the higher-order modes with a physical mechanism, since all the impeller channels of the centrifugal pump have zones with a low level of correlation between velocity fluctuations. Differently, for $Q^* = 1.5$, it is possible to identify flow structures similar to those found for the lowest flow rate, but with smaller scales. From mode 4 (Fig. 5.8f), regions of correlated velocity fluctuations in the vicinity of the impeller eye are also detected, indicating that the instabilities responsible for the boundary layer detachment are being captured by this POD mode.

In summary, as the rank of POD modes increases, the energy of velocity fluctuations decreases for all flow conditions studied in this paper. Modes 1 and 2 are responsible for larger-scale unstable flow structures, i.e., large vortices and "jet-wakes", whereas modes 3 and 4 are associated with smaller-scale unstable structures. Above that, the addition of more POD modes does not contribute significantly to the physics of the flow, as these higher modes are related to the noise, inherent in the PIV technique[3].

Although some physical mechanisms of the unstable flow in the studied centrifugal pump are related to the POD modes calculated in this work and align with previous literature (Zhang *et al.*, 2021; Chen *et al.*, 2022b, 2024), it becomes evident that directly interpreting these phenomena from Fig. 5.7 and 5.8 is challenging, except by considering the correlation level of $\mathbf{u}$. Due to its mathematical definition, POD is suitable for analyzing statistically stationary flows. Although widely used in fluid flow analysis, the method faces difficulties in the spatial characterization (POD modes, ϕ_k) of highly transient phenomena dominated by intermittent events of coherent structures. This results in modes that are difficult to physically interpret.

[3]See the videos in the supplementary material at `https://doi.org/10.1016/j.flowmeasinst.2023.102483`.

An example of this limitation is seen in the characterization of the transport of structures in dynamic stall, such as those occurring in a centrifugal pump (Krause *et al.*, 2005; Liu *et al.*, 2022; Feng *et al.*, 2021; Tang *et al.*, 2024). In these situations, the presence of a periodic field in the flow hampers the interpretation of the k-norm POD modes, as they essentially represent the oscillatory content of the data around the mean. Recent information on the limitations of POD modes in transient and intermittent flows can be found at Baj *et al.* (2015) and Souza *et al.* (2024).

5.4.3 Temporal characteristics

According to the previous section, there is a coupling between the pairs of POD modes. To further investigate this observation, the temporal characteristics of modes 1-2 and 3-4 for $\mathcal{N} =$ 600 rpm are determined in the present section. The temporal coefficients, frequency spectra, as well as phase diagrams between the pairs of modes are presented in Figs. 5.9, 5.10 and 5.11.

The analysis of the temporal coefficients of the first two POD modes for the three flow conditions confirms the similarities between the structures (Fig. 5.9a, 5.9c and 5.9e): both show periodicity with similar amplitudes of the peaks. This is an evidence that the modes represent a periodic structure of the water flow.

At $Q^* = 0.3$, the temporal coefficients for the first two modes have the same characteristics, except for a phase shift (Fig. 5.9a). In addition, a well-defined peak frequency corresponding to 10 Hz is identified for both modes (Fig. 5.9b), this being consistent with the rotation frequency of the pump impeller (600 rpm = 10 Hz). The distinct single peak indicates that there is a single flow phenomenon described by the first two modes at this flow rate. For the design (Q^* $= 1.0$) and highest flow rate conditions ($Q^* = 1.5$), we observe the same properties as those presented for $Q^* = 0.3$, but with a lower matching level. This is a consequence of the energy present in the first two modes of each case analyzed. From Figs. 5.9d and 5.9f, it is clear that the dominant frequency of modes 1 and 2 is still the pump rotation speed.

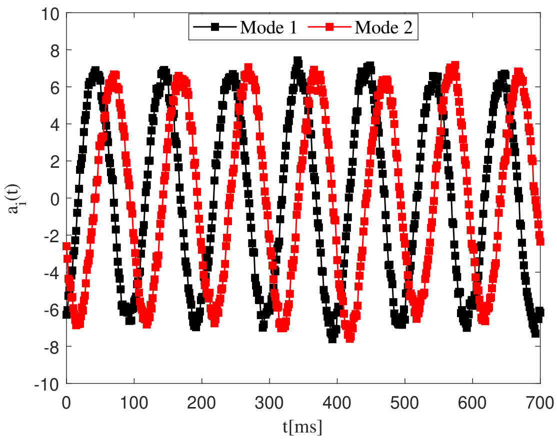

(A) time coefficients - $Q^* = 0.3$

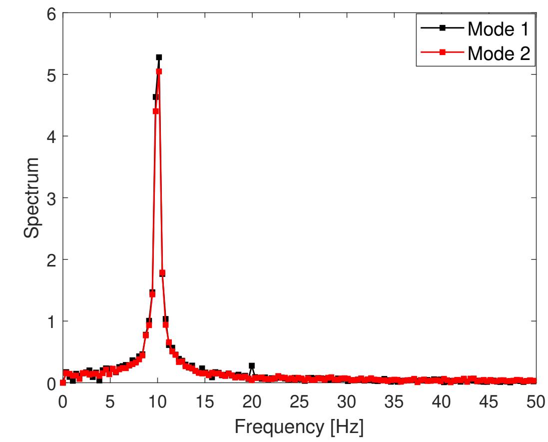

(B) FFT distribution - $Q^* = 0.3$

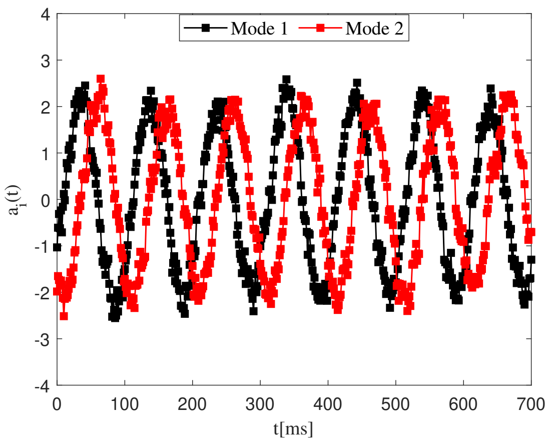

(C) time coefficients - $Q^* = 1.0$

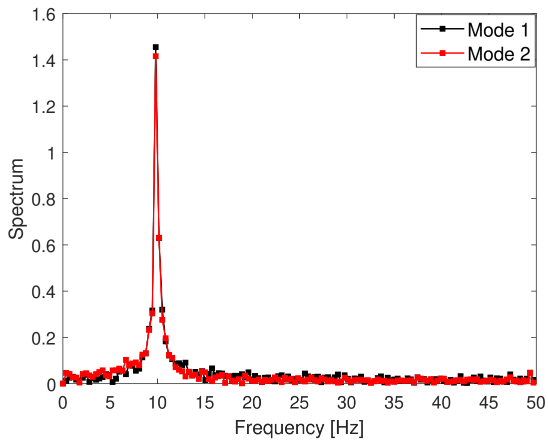

(D) FFT distribution - $Q^* = 1.0$

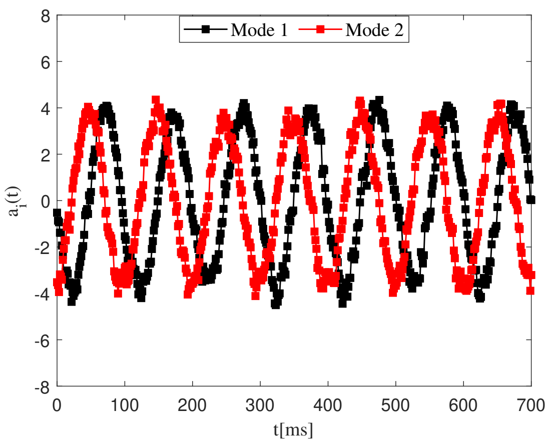

(E) time coefficients - $Q^* = 1.5$

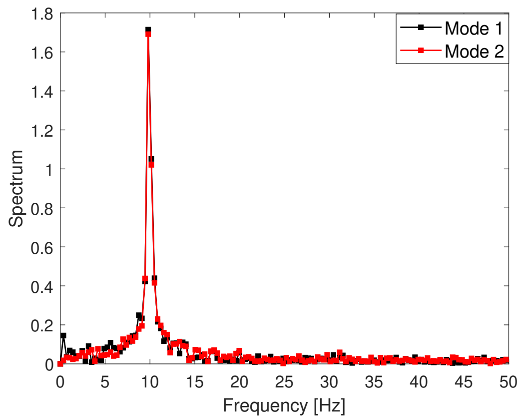

(F) FFT distribution - $Q^* = 1.5$

FIGURE 5.9 – time coefficients and FFT distribution of the first two modes at 600 rpm for different flow rates (Fonseca *et al.*, 2023).

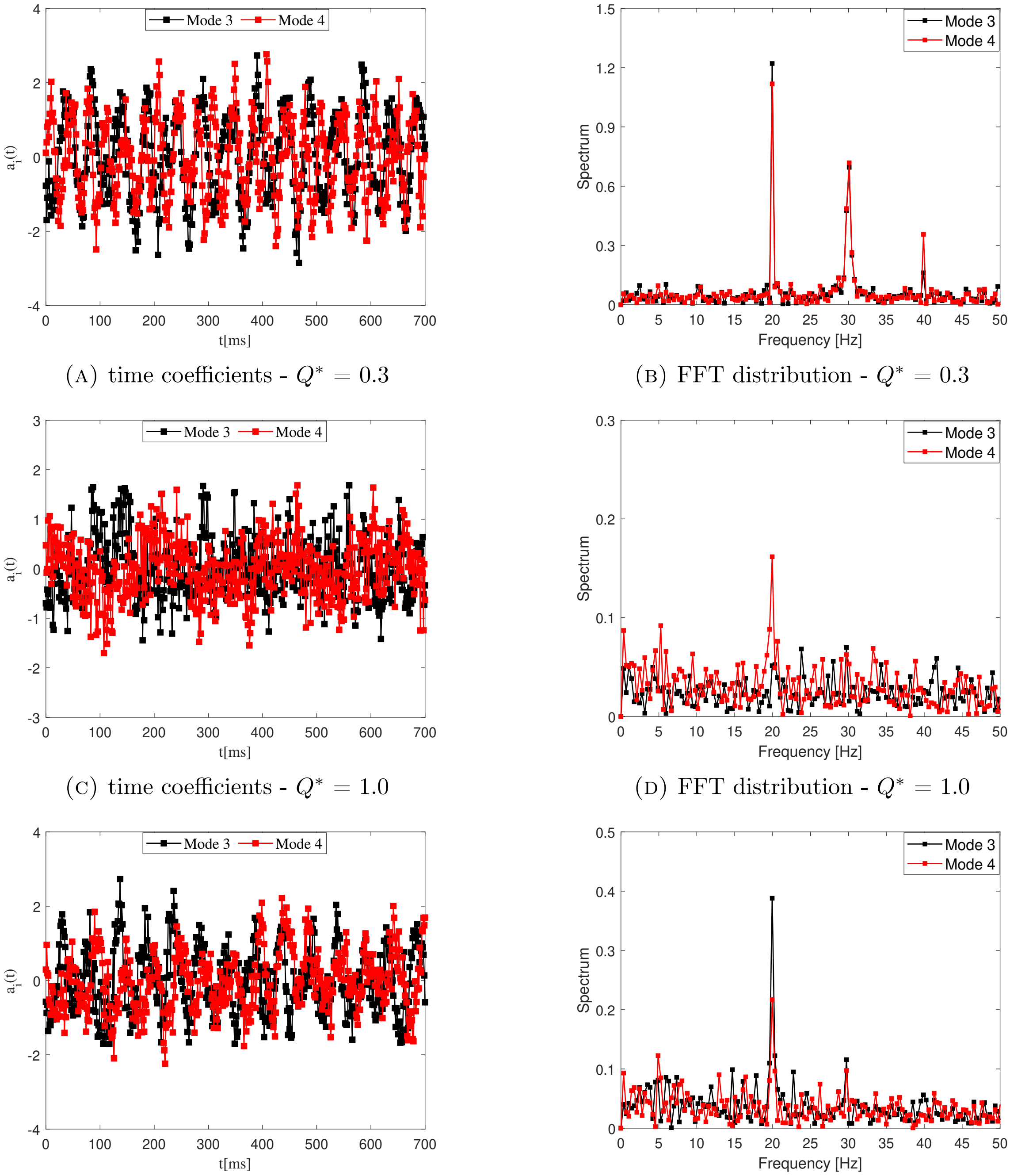

(A) time coefficients - $Q^* = 0.3$

(B) FFT distribution - $Q^* = 0.3$

(C) time coefficients - $Q^* = 1.0$

(D) FFT distribution - $Q^* = 1.0$

(E) time coefficients - $Q^* = 1.5$

(F) FFT distribution - $Q^* = 1.5$

FIGURE 5.10 – Time coefficients and FFT distribution of the third and fourth modes at 600 rpm for different flow rates (Fonseca *et al.*, 2023).

For modes 3 and 4, the distributions of temporal coefficients indicate that there is no correlation at the flow rates analyzed in this work (Fig. 5.10). However, we note that for $Q^* = 0.3$ modes 3 and 4 are the harmonics of modes 1 and 2, characterized by smaller energy spectra. These results suggest that large flow structures form at a frequency similar to the rotation speed of the pump impeller and then break up into smaller structures at a rate that corresponds to two impeller revolutions. Furthermore, for the design condition ($Q^* = 1.0$), the frequency spectra are noisy, and several peaks at relatively low amplitudes can be observed. For $Q^* = 1.5$, one peak can be seen at 20 Hz, which is also a harmonic of the first two modes. Such results again suggest that higher-order POD modes represent small-scale unstable flow structures in the centrifugal pump impeller, which are deriving from the cascade effect.

The different POD modes can also be analyzed through phase diagrams of temporal coefficients, as shown in Fig. 5.11. According to Semeraro *et al.* (2012), pairs of POD modes characterized by quasi-circular phase diagrams are comparable to Fourier modes, where the phase diagrams plots are perfect circles. Thus, POD pairing can be considered a criterion to assess the similarity between POD modes.

The phase diagrams of the first two modes for $Q^* = 0.3$, $Q^* = 1.0$ and $Q^* = 1.5$ are depicted, respectively, in Figs. 5.11a, 5.11b, 5.11c. We observe that for such flow conditions, the trajectory exhibits an circular behavior, similar to the one observed for vortex shedding behind a cylinder (Ma & Karniadakis, 2002). Thus, it is believed that the POD modes 1 and 2 represent vortical structures in the impeller, for which large-scale structures at low flow rates break up into small-scale structures when the flow rate increases and reaches the design point. This trend is shown in Fig. 5.6 and also by the scale of the axes that compose the phase diagrams in Fig. 5.11.

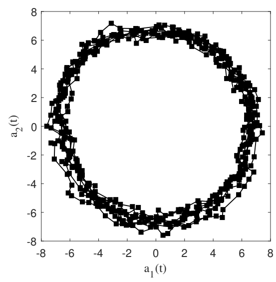

(A) $Q^* = 0.3$

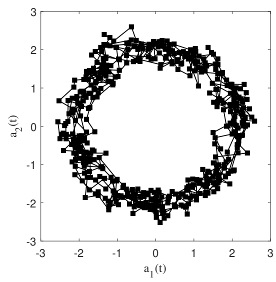

(B) $Q^* = 1.0$

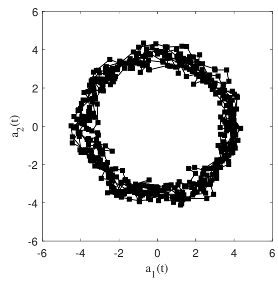

(C) $Q^* = 1.5$

FIGURE 5.11 – Phase diagram of the first two modes at 600 rpm for different flow rates (Fonseca *et al.*, 2023).

As with the analyses of POD spatial modes (Sec. 5.4.2), the literature on POD in centrifugal pumps confirms the relationship between temporal coefficients and the physical mechanisms present in the unstable flow in the centrifugal pump impeller. However, the velocity fluctuation used to compose the POD norm in this study, as well as in previous works (Zhang *et al.*, 2021; Chen *et al.*, 2022b, 2024), is extracted from a Reynolds decomposition, as presented in Eq. (2.15), reproduced below for the reader's convenience:

$$\mathbf{U}(\mathbf{x}, t) = \langle \mathbf{U}(\mathbf{x}, t) \rangle + \mathbf{u}(\mathbf{x}, t)$$

This approach for subsequent POD analyses is reasonable under the assumption that turbulence is the only source of fluctuations. However, in the context of a centrifugal pump, this assumption may not hold. Given the impeller's rotational motion, we expect to observe both coherent, well-organized large-scale motion and stochastic fluctuations at frequencies different from the impeller frequency. Failing to distinguish between these two phenomena can result in a notable overestimation of the stochastic component of the flow.

Thus, an alternative approach to overcome this limitation is proposed based on the work of Hussain & Reynolds (1970), where a triple decomposition of the following form is suggested:

$$\mathbf{U}(\mathbf{x}, t) = \langle \mathbf{U}(\mathbf{x}, t) \rangle + \tilde{\mathbf{u}}(\mathbf{x}, \theta(t)) + \mathbf{u}(\mathbf{x}, t) \tag{5.4}$$

In Eq. (5.4), $\mathbf{U}$ is the instantaneous velocity field, $\langle \mathbf{U} \rangle$ represents its average value, $\tilde{\mathbf{u}}$ is the phase-dependent part (with θ denoting the impeller phase angle), and $\mathbf{u}$ corresponds to the stochastic part of $\mathbf{U}$.

One way of decoupling $\tilde{\mathbf{u}}$ and $\mathbf{u}$ can be achieved by a procedure known as bin averaging (Cantwell & Coles, 1983):

$$\tilde{\mathbf{u}}(\mathbf{x}, \theta_0) = \mathrm{mean}_{\theta(t) \in \Psi} \{ \mathbf{U}(\mathbf{x}, t) - \langle \mathbf{U}(\mathbf{x}, t) \rangle \} \tag{5.5}$$

where Ψ is a phase bin bounded. Based on this approach, the phase value can be assigned to each snapshot of the centrifugal pump impeller. Thus, the idea is to gather and regroup the data into several subsets corresponding to different phase bands. By averaging within each of these bins, an estimate for $\tilde{\mathbf{u}}$ can be derived.

Therefore, a new estimate for stochastic fluctuation field can be given by:

$$\mathbf{u}(\mathbf{x}, t) = \mathbf{U}(\mathbf{x}, t) - \langle \mathbf{U}(\mathbf{x}, t) \rangle - \tilde{\mathbf{u}}(\mathbf{x}, \theta(t)) \tag{5.6}$$

Previous studies using the described methodology are being conducted with the working data presented in Fonseca *et al.* (2023). Further details about this new proposal can be found in Sec. 7.3.

5.5 Turbulence production

The flow kinetic energy equation clearly shows the important role played by turbulence production. The action of the averaged velocity gradients working against the Reynolds stresses removes the kinetic energy from the mean-flow and transfers it to the fluctuating velocity field.

As indicated in Eq. (2.23), the turbulence production is defined as:

$$\mathcal{P}_{ij} = -\langle u_i u_j \rangle \frac{\partial \langle U_i \rangle}{\partial x_j}$$

Figure 5.12 presents the production of turbulent kinetic energy measured in the axial mid-plane of the impeller and normalized to the impeller radius and blade tip velocity ($\mathcal{P}^*_{2D} = \mathcal{P}_{2D}/r_{\text{out}}U^3_{\text{tip}}$) at 600 rpm. As indicated in Fig.5.12b, turbulence production at the design point occurs mainly in the areas close to the impeller inlet and extends along the suction blades. This can be attributed to the turbulence generated by the pre-rotation of the flow, as discussed in Sec. 5.3. Additionally, the observation reveals turbulence production at the trailing edges of the blades, which is intimately linked to flow separation in these specific regions.

Under part-load conditions, $Q^* = 0.3$, we observe localized regions of intense turbulence production near the impeller inlet and outlet, as illustrated in Fig. 5.12a. In the inlet region, the generation of turbulent kinetic energy is associated with flow separation, whereas at the impeller outlet, the conversion of average flow into turbulence production is facilitated by the strong shear occurring between the existing vortices and recirculation zones, as indicated in Figs. 5.1d and 5.4d.

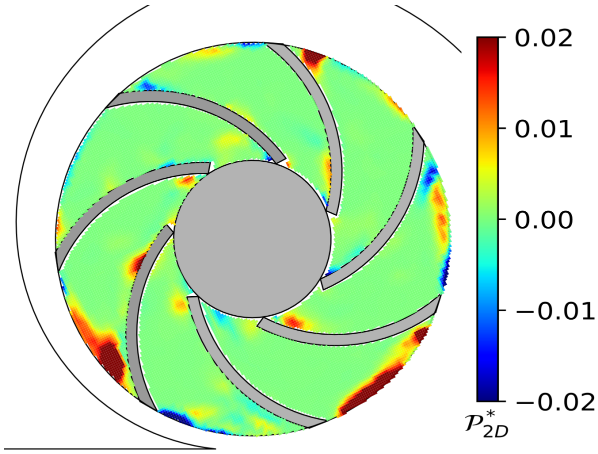

(A) $Q^* = 0.3$

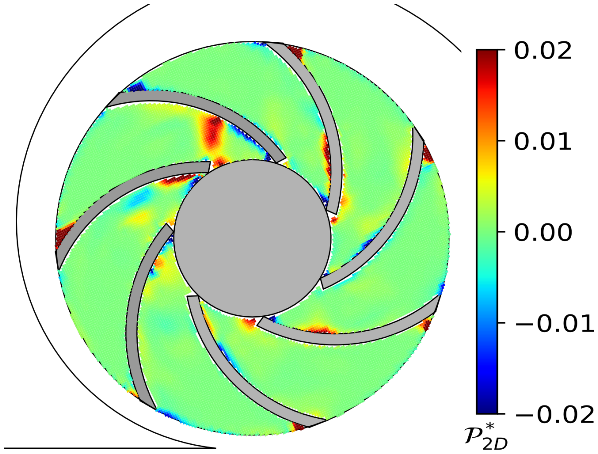

(B) $Q^* = 1.0$

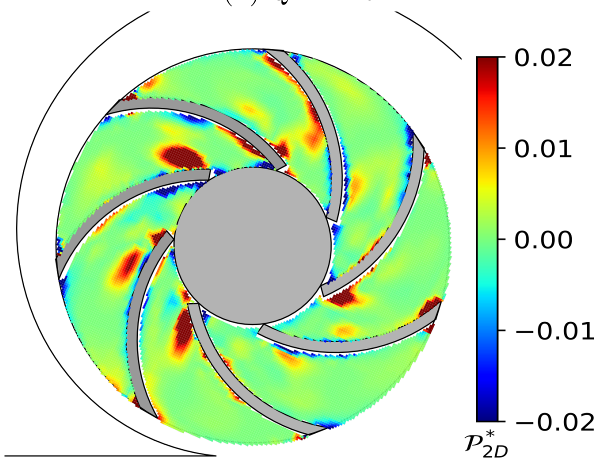

(C) $Q^* = 1.5$

FIGURE 5.12 – Normalized turbulence production in the centrifugal pump impeller (Fonseca *et al.*, 2024).

For $Q^* = 1.5$, Fig. 5.12c demonstrates that turbulence production is more intense on the surface of the blades, with peak values close to the entrance of each channel. This observation confirms the detachment of the flow on the blades under this flow condition, as previously indicated by the field in Fig. 5.5f. In addition, we can also detect turbulence production in peripheral regions in the channels closer to the volute tongue. This phenomenon is related to the vorticity released from the trailing edge of the blades and to the high viscous stresses that are expected in the region of the tongue.

Turbulence production can be physically understood as the product of an inertial force, $-\rho\langle u_j\rangle\partial_{x_j}\langle U_i\rangle$, and a velocity fluctuation, $\langle u_i\rangle$. When the inertial force and the fluctuating velocity are in opposing directions (i.e., $\mathcal{P}_{2D} > 0$), it signifies that the mean flow exerts an influence on the fluctuating velocity field, encouraging the conversion of mean flow into turbulent kinetic energy, consequently leading to increased flow energy dissipation. Conversely, when the product is negative (i.e., $\mathcal{P}_{2D} < 0$), it implies that fluctuations are influencing the mean flow (Cimarelli *et al.*, 2019).

As shown in Fig. 5.12, all impeller channels under the analyzed flow conditions exhibit opposite signs of turbulence production. This indicates an inverse energy cascade, with kinetic energy propagating in the opposite direction to the natural flux of the Richardson-Kolmogorov energy cascade. According to classical theory, turbulence is a three-dimensional phenomenon in which vorticity is teased out into finer and finer filaments, carrying its energy to smaller and smaller scales. However, Batchelor (1969) theory suggests that certain turbulent flows can exhibit "almost" two-dimensional characteristics.

According to this theory, known as quasi-two-dimensional turbulence (Davidson, 2015), this often occurs due to the intense stratification of the flow, which tends to suppress a component of the flow, allowing for the approximation of two-dimensionality based on geometry.

Considering the geometry of the centrifugal pump impeller analyzed in this study, which has a depth of 6 mm, it is believed that the reverse energy cascade process is due to the approximation of a quasi-two-dimensional turbulent flow behavior. This occurs because the pump's shallow height restrains the vertical expansion of the vortex filaments, promoting strong stratification and favoring the transfer of kinetic energy to larger scales rather than smaller ones.

5.6 Local turbulent dissipation rate

The turbulent dissipation rate in the impeller of the pump is calculated using Eq. (2.34) as previously mentioned. It is normalized by the angular speed and impeller diameter ($\varepsilon^* = \langle \varepsilon_{SGS} \rangle / \Omega^3 D^2$). The spatial derivatives required in Eq. (2.34) are computed using a central finite difference scheme. Additionally, the large-eddy PIV approach is employed, in which the subgrid-scale (SGS) stress is determined using the Smagorinsky model (see Sec. 2.3.2).

Before proceeding with the estimation of the dissipation rate from PIV measurements using the LES-PIV method, it is crucial to assess the validity of the dynamic equilibrium assumption. The Kolmogorov length scale (Eq. 5.7) is derived from the values of the overall dissipation rate $\langle \varepsilon \rangle$. This overall dissipation rate, in turn, is calculated using data on the impeller's hydraulic power, density, and volume occupied by the fluid inside the impeller, which can be approximated as a pipeline, i.e., a hollow cylinder (Eq. 5.8) (Perissinotto *et al.*, 2024a). The average values of the dissipation rate, normalized by the angular speed and impeller diameter, and the Kolmogorov scale are presented in Tab. 5.1 for the three flow rates studied in this work under a rotation of 600 rpm.

$$\langle \eta_k \rangle = \left(\frac{\nu^3}{\langle \varepsilon \rangle} \right)^{1/4} \tag{5.7}$$

$$\langle \varepsilon \rangle = \frac{P_{\mathrm{h,imp}}}{\rho \forall_{\mathrm{fluid}}} \tag{5.8}$$

TABLE 5.1 – Average normalized dissipation rate and Kolmogorov scale for each flow condition at 600 rpm.

Q^*	$\langle \varepsilon \rangle^* = \langle \varepsilon \rangle / \Omega^3 D^2$	$\langle \eta_k \rangle$ [μm]
0.3	6.58×10^{-3}	15
1.0	19.53×10^{-3}	11
1.5	26.0×10^{-3}	11

Thus, as indicated in the Tab. 5.1, the resolution of the PIV measurements does not approach the Kolmogorov scale, as expected, but would be supposed to be within the inertial sub-range. These magnitudes are comparable to those found in previous works applying LES-PIV (Sheng *et al.*, 2000; Gabriele *et al.*, 2009; Delafosse *et al.*, 2011).

As previously discussed in other works employing the LES-PIV method (Delafosse *et al.*, 2011; Verwey & Birouk, 2022; Xu & Chen, 2013; Laine *et al.*, 2023), the calculated value of the local dissipation rate is strongly influenced by the spatial resolution of the PIV measurements. In order to precisely estimate the turbulent dissipation rate, it would be necessary to work with a spatial resolution under the Kolmogrov legnth scale (Eq. 5.7), i.e. $\Delta/\langle n_k \rangle \approx 1$. However, our measurements are limited to fixed-size interrogation windows, a value that arises as a consequence of optimizing PIV variables such as seeding particle density per interrogation window, time between two consecutive image frames, and signal-to-noise correlation peak. These parameters were optimized for $\Delta = 3$ mm, following the guidelines discussed in Raffel *et al.* (2018).

As indicated in Fig. 5.13a, regions of high energy dissipation can be observed for the low flow rate condition, $Q^* = 0.3$. It is interesting to note that these regions correspond to locations of high vorticity in the impeller (Fig. 5.4d), which indicates that a portion of the energy generated in this condition is dissipated within the channels.

In contrast, for the design condition shown in Fig. 5.13b, considerably smaller values of turbulent kinetic energy dissipation are observed. This suggests that, due to the absence or reduced presence of vortex structures in the flow, turbulence dissipation is lower. Furthermore, we can observe that energy dissipation in this operating condition mainly occurs close to the blade surfaces, indicating that smaller-scale structures present in wall regions dissipate energy through a conversion process that starts from the larger turbulent scales and breaks down into smaller structures, ultimately transforming into heat.

For the condition $Q^* = 1.5$, we observe in Fig. 5.13c that the impeller eye registers a higher dissipation rate than that presented at $Q^* = 0.3$ and $Q^* = 1.0$. In addition, the dissipation rate seems to be higher on the pressure side of the blades than on the suction side for this flow rate. This particular phenomenon can be attributed to flow separation that occurs predominantly on the pressure side, as previously expounded (Fig. 5.4f and Fig. 5.12c). On the other hand, the suction side experiences relatively lower dissipation, possibly due to a more favorable flow pattern that mitigates the dissipation impact.

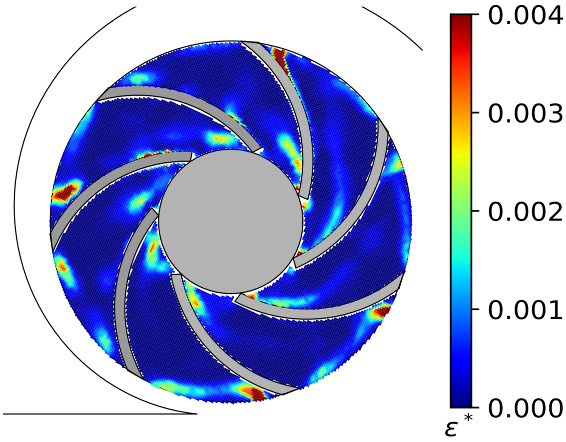

(A) $Q^{*} = 0.3$

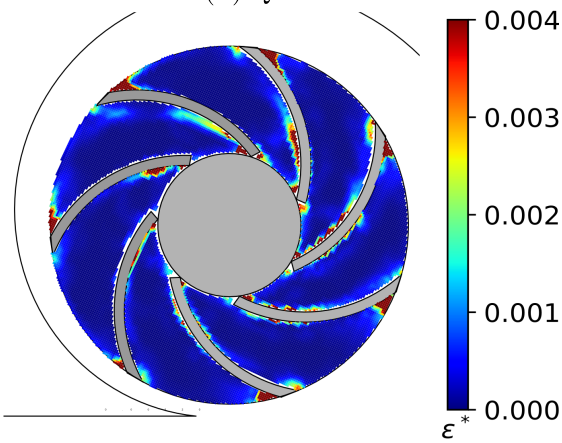

(B) $Q^{*} = 1.0$

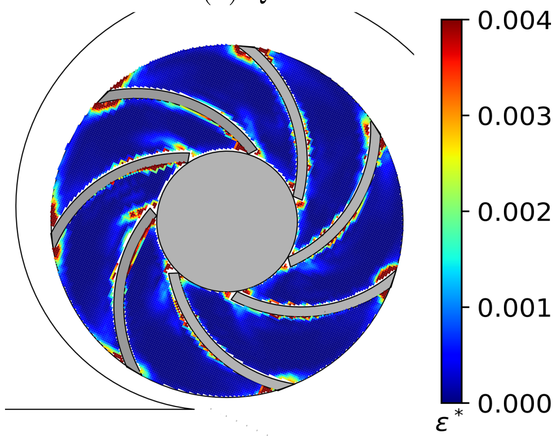

(C) $Q^{*} = 1.5$

FIGURE 5.13 – Normalized turbulent dissipation rate in centrifugal pump impeller (Fonseca *et al.*, 2024).

When comparing the global dissipation rate with the local dissipation rate resulting from the model presented in Eq. (2.34), we observed relative deviations of 53%, 76%, and 67% for the conditions of $Q^* = 0.3$, 1.0, and 1.5, respectively. These deviations can be attributed to the dependence on the spatial resolution of the interrogation windows and the consideration of isotropy adopted in the calculation of $\langle \varepsilon_{SGS} \rangle$. Specifically, the flow within centrifugal pump impellers is often characterized by centrifugal forces and non-uniform velocity profiles, as depicted in Fig. 5.3. These factors contribute to a non-isotropic turbulent flow, explaining the observed discrepancies in dissipation rates between the global and local estimations.

5.7 Loss analysis

In this section, two methods are presented to analyze the energy loss in the impeller. The first approach uses experimental data from impeller-focused performance measurements (Sec. 5.7.1). The second method employs the turbulent flow kinetic energy equation to extract qualitative impeller loss data (Sec. 5.7.2). The results of the analyses are presented in the following section (Sec. 5.7.3).

5.7.1 Conventional energy loss

According to Gülich (2008), energy losses in centrifugal pumps occur due to several factors, which can be categorized into hydraulic losses and mechanical losses. Hydraulic losses primarily result from the conversion of mechanical energy into heat and turbulence. Mechanical losses, on the other hand, are associated with frictional losses.

The energy loss equation in a centrifugal pump describes the relationship between the input energy and the various energy losses that occur within the pump (White, 2015), typically expressed in terms of power. However, we propose adapting this loss equation to address the impeller only:

$$L_1 = P_{\mathrm{in,imp}} - P_{\mathrm{h,imp}} \tag{5.9}$$

As observed, the first energy loss equation, in Eq. (5.9), depends on the input and hydraulic powers. These powers were defined for the entire pump in Eqs. (2.2) and (2.3), but they must be rewritten to a region of interest limited to the impeller:

$$P_{\mathrm{h,imp}} = \rho\ g\ H_{\mathrm{imp}}\ Q_w \tag{5.10}$$

$$P_{\mathrm{in,imp}} = \Omega\ M_{\mathrm{imp}} \tag{5.11}$$

In Eq. (5.10), the head is redefined to describe the head generated by the impeller, H_{imp}. It is possible to calculate this head experimentally by using the pressure gain measured between the impeller eye and the impeller-volute boundary, ΔP_{imp}, as reported in Sec. 3.2:

$$H_{\mathrm{imp}} = \frac{\Delta P_{\mathrm{imp}}}{\rho\ g} + \frac{\langle U_{\mathrm{out}} \rangle^2 - \langle U_{\mathrm{in}} \rangle^2}{2g} \tag{5.12}$$

Differently from H_{pump} (Eq. 2.1), the head H_{imp} (Eq. 5.12) must include the variation of kinetic energy from inlet to outlet, as the fluid velocity changes significantly in the impeller mainly due to the angular velocity, Ωr, proportional to the rotational speed and radial position. This kinetic term is thus a function of the magnitude of the absolute velocity of the liquid flowing near the impeller inlet, $\langle U_{\mathrm{in}} \rangle$, and outlet, $\langle U_{\mathrm{out}} \rangle$. Such velocities are directly determined through PIV measurements.

Figure 5.14 shows a drawing of the transparent pump indicating the points where ΔP_{imp} is measured during the experiments. The pressure sensor is placed on the points P_1 (physically connected to inner radius r_{in}, through the pump shaft, which has a hole in the center) and P_2 (near radius r_{out}, in the first quadrant, upstream of the interface between impeller and volute). In addition, when calculating the term $\langle U_{\mathrm{out}} \rangle^2 - \langle U_{\mathrm{in}} \rangle^2$ from PIV data, the velocity information is extracted at these same locations: the impeller eye (impeller inlet) and a point in the volute next to the impeller-volute boundary (representing the impeller outlet).

Regarding Eq. (5.11), the torque required to move the fluid-filled impeller, M_{imp}, is calculated from the difference between the torque measured at the motor-pump set at a regular operation (M_{pump}) and under a “dry running” condition (M_{dry}), as explained in Sec. 3.2. As a result, M_{imp} is determined experimentally as well:

$$M_{\text{imp}} = M_{\text{pump}} - M_{\text{dry}} \tag{5.13}$$

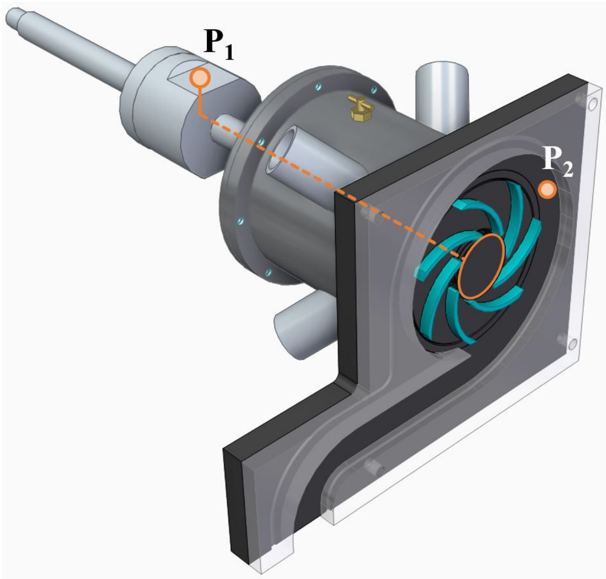

FIGURE 5.14 – Location of the differential pressure measurements (Fonseca *et al.*, 2024).

Nevertheless, there is another way to calculate the torque transferred from the impeller to the fluid: it can be estimated from the velocity fields obtained via PIV measurements. We can use the angular-momentum principle typically presented in the turbomachinery theory (White, 2015) to obtain the torque acting on a fixed control volume enclosing the impeller. For steady flow, it is possible to rewrite Eq. (5.10) to compute the hydraulic power from this torque:

$$P_{\text{h,imp}} \approx \Omega \int_{CS} \mathbf{r} \times \mathbf{U}\ \rho\ \mathbf{U} \cdot d\mathbf{A} \tag{5.14}$$

In this case, the static pressure is assumed to change radially within the impeller, remaining constant over the inlet and outlet surfaces, as discussed in Van Oudheusden (2013). Consequently, the torque generated by these pressure changes is neglected.

The calculation of $P_{\text{h,imp}}$ using Eq. (5.14) demands the absolute velocity vectors ($\mathbf{U}$) that cross the impeller control surfaces in radial positions ($\mathbf{r}$) corresponding to the inner and outer radii. These surfaces are divided into area elements represented by normal vectors ($d\mathbf{A}$). As the velocity vectors consist of discrete data, M_{imp} must be determined through numerical integration. In the present study, the calculations are executed in routines developed in Python™ programming language.

5.7.2 Turbulent-flow kinetic energy loss

To qualitatively assess energy loss within the pump impeller, this section's methodology focuses on analyzing the spatial distribution of this loss. This investigation relies on the turbulence kinetic energy budget equation, which relates alterations in turbulent flow energy and the underlying mechanisms that drive these changes. The model presented here seeks to evaluate losses in the pump impeller through an energy conversion analysis.

The turbulent-flow kinetic energy equation, assuming constant viscosity and density, can be expressed as follows:

$$\frac{D}{Dt}\left\langle \frac{1}{2}u_i u_i \right\rangle = -\frac{\partial}{\partial x_j}\left[\frac{\langle u_j p\rangle}{\rho} + 2\nu \langle u_i s_{ij}\rangle - 2\nu \langle u_i s_{ij}\rangle\right] - 2\nu \langle s_{ij} s_{ij}\rangle - \langle u_i u_j\rangle \bar{S}_{ij} \tag{5.15}$$

The first three terms on the right-hand side are in the flux divergence form. If Eq. (5.15) is integrated over the entire flow domain to determine the rate of change in global turbulent kinetic energy, these divergence terms can be transformed into a surface integral using Gauss theorem. Consequently, these terms do not contribute to a flow confined to a limited spatial region where $\mathbf{U} = 0$ at a sufficient distance. Thus, these terms solely redistribute energy from one region to another but cannot generate or dissipate it (Pope, 2000).

The fourth term results from the product of strain rate, denoted as s_{ij}, and viscous stress, $2\nu s_{ij}$. This term represents a loss of energy occurring throughout the flow, which characterizes the dissipation of turbulent kinetic energy due to viscosity. In this context, energy is transferred to the agent responsible for viscous tension, subsequently transforming it into kinetic energy of molecular movement, which takes the form of heat.

The turbulence production term originates from the interaction between turbulent stress and the mean strain rate field. This term represents an energy loss linked to the agent responsible for generating turbulent fluctuations, particularly the fluctuating field. As a consequence, this term typically results in a decrease in average kinetic energy and an increase in turbulent kinetic energy.

Thus, the second approach to estimating the energy loss in turbulent flow within the impeller involves summing integrals over the entire control volume, which encompasses the seven channels of the impeller. This sum includes both losses due to viscous dissipation and losses resulting from the production of turbulence, which are obtained through the PIV measurements in the impeller.

$$L_2 = \int_{CV} [\mathcal{P}_{ij} - \langle \varepsilon_{SGS} \rangle] \, d\forall \tag{5.16}$$

5.7.3 Energy loss results

The first method to estimate the energy loss in the impeller (L_1, Eq. 5.9) is dependent on H_{imp} and M_{imp}. The torque in the impeller, M_{imp}, is estimated from the torque measured in the pump shaft (Eq. 5.13). Measurements using the torque meter suggest that M_{dry} accounts for more than 85% of M_{pump}, meaning that most of the energy supplied by the electric motor to the pump shaft is lost in components such as bearings and seals. From this torque required to move the fluid in the impeller, the input power is finally calculated (Eq. 5.11).

In addition, the head (Eq. 5.12) is determined from the differential pressure measured during the tests and the average velocity evaluated in two locations of the pump stage. Figure 5.15 shows an example of ensemble-averaged velocity field of absolute velocity vectors, $\langle \mathbf{U} \rangle$, obtained via PIV for $Q^* = 1.0$. In the locations indicated by both black circumferences, the magnitudes of these vectors provide the kinetic term of H_{imp}. According to our data, this term represents from 10 to 20% of the impeller head, while the term due to pressure increment is more significant and corresponds to a number between 80 and 90% of H_{imp}, depending on the flow rate.

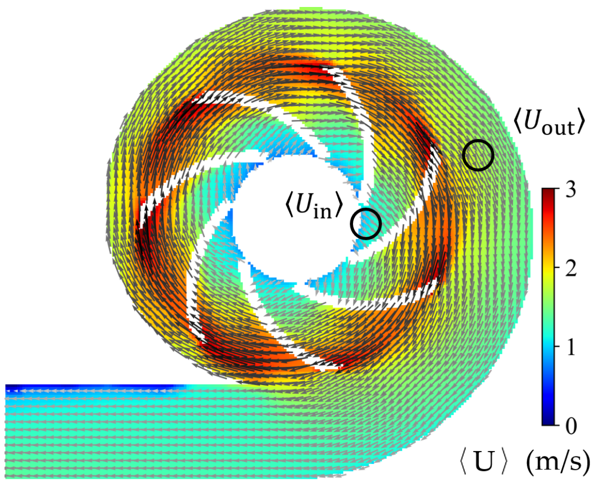

FIGURE 5.15 – Absolute velocity field for $Q^* = 1.0$. The black circles indicate regions where $\langle U_{\text{in}} \rangle$, $\langle U_{\text{out}} \rangle$ are evaluated (Fonseca *et al.*, 2024).

From the head H_{imp}, it is possible to calculate the hydraulic power effectively delivered to the fluid (Eq. 5.10). Nevertheless, this power can be estimated from the angular-momentum conservation principle, which employs absolute velocity fields extracted from PIV data (Eq. 5.14). Our results reveal that both methods provide similar values of $P_{\text{h,imp}}$, with relative differences lower than 20%.

Results for $P_{\text{h,imp}}$ and $P_{\text{in,imp}}$ are presented in Fig. 5.16, which contains curves of these powers as a function of the flow rate. As expected, the input power is higher than the hydraulic power ($P_{\text{in,imp}} > P_{\text{h,imp}}$). In the graph there are two hydraulic power curves, one for each calculation approach (Eq. 5.10 *versus* Eq. 5.14). These curves are very similar, regardless of the method used to obtain them, which means that the energy loss can be obtained from any hydraulic power curve. Hence, we prefer to calculate L_1 using the arithmetic mean of both $P_{\text{h,imp}}$ values to ensure a more accurate result. The results for L_1 determined through this procedure are shown in Tab. 5.2.

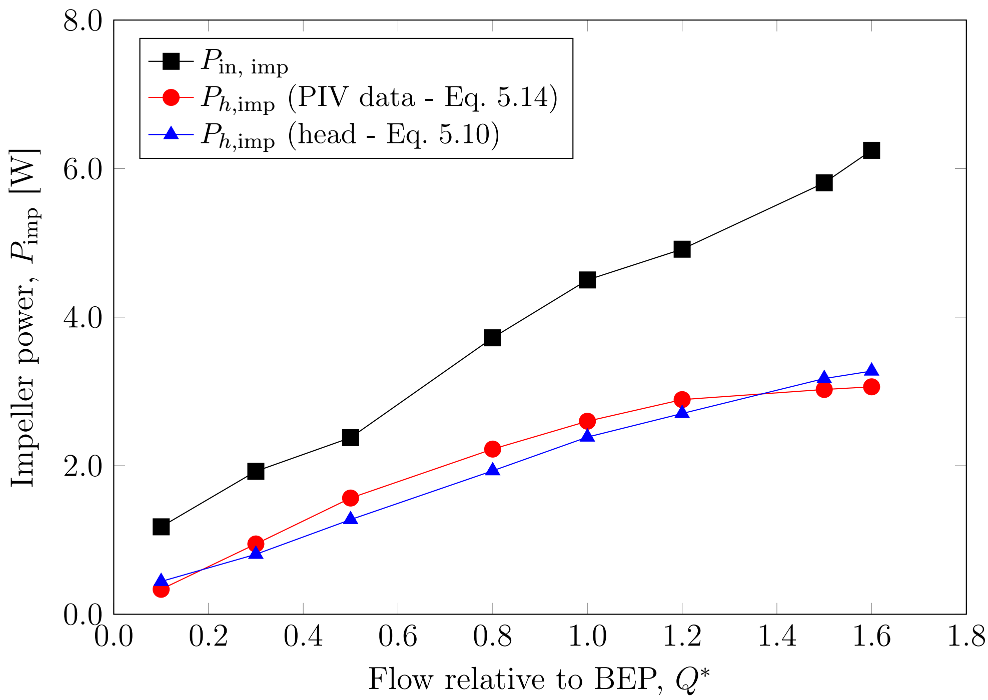

FIGURE 5.16 – Curves of imput and hydraulic powers in the impeller. Results valid for eight flow rates (Fonseca *et al.*, 2024).

TABLE 5.2 – Energy losses in the centrifugal pump impeller at different flow rates.

	L_1 [W]	$L_1^* = L_1/P_{\text{in,imp}}$	$L_2^* = L_2/P_{\text{in,imp}}$	$\sigma = [\text{abs}(L_2^* - L_1^*)/L_1^*] \times 100\%$
$Q^* = 0.3$	1.049	0.54	0.29	46%
$Q^* = 1.0$	2.010	0.45	0.21	52%
$Q^* = 1.5$	2.708	0.47	0.24	49%

The reader may question the fact that Fig. 5.16 present results for eight flow rates, while the test matrix of this work is limited to three flow rates. It is important to mention that additional experiments were performed exclusively to quantify ΔP_{imp} and M_{imp} directly from the instruments. The estimation of absolute velocities $\langle \mathbf{U} \rangle$, $\langle U_{\text{in}} \rangle$, $\langle U_{\text{out}} \rangle$ was based on results by Perissinotto (2023), which were obtained via PIV method applied on the same pump used in the present work.

As presented in Tab. 5.2, the absolute energy loss L_1 is directly proportional to the flow rate and ranges from approximately 1.0 to 2.7 Watts. These losses are attributed to various factors, including viscous effects, flow direction inconsistency with the blade angle, non-uniform flow, and other inefficiencies in the impeller (Gülich, 2008).

Table 5.2 thus shows that the absolute energy losses L_1 increase (decrease) as the flow increases (decreases). However, it can also be seen from Tab. 5.2 that the energy loss normalized by the impeller input power ($L_i^* = L_i/P_{\text{in,imp}}$) is lower for BEP condition ($Q^* = 1.0$) and higher for low flow rates ($Q^* = 0.3$). The relative deviation (σ) of L_2^* with respect to L_1^* was also investigated under different flow conditions: For the low flow condition, the relative deviation is 46%; as the flow rate increases to $Q^* = 1.0$, this deviation increases to 52%; and for the high flow condition ($Q^* = 1.5$), it assumes a value of approximately 49%.

The variation observed in the relative deviation can be attributed to the method used for loss calculations (L_1 or L_2) and the underlying flow structures at different flow rates. At the lowest flow rate ($Q^* = 0.3$), large-scale vortex structures are generated (Chen *et al.*, 2022b; Ni *et al.*, 2023), dominating the energy losses in the impeller. However, for the design condition and the highest flow rate ($Q^* = 1.5$), the flow is dominated by small-scale turbulent structures. Since the smallest turbulent scales included in the L_2 calculation are determined by a sub-grid scale model, discrepancies are expected between the values. Such disagreement in the results can be attributed to two factors: i) The Nyquist frequency imposed by the finite size of the interrogation windows, i.e., a grid cell of size Δ cannot resolve a flow structure smaller than 2Δ (Hsieh *et al.*, 2010). It means that the smaller-scale flow structures that are calculated from L_2 are more dependent on the resolution of the PIV mesh; ii) The calculated energy dissipation tends to be more prominent in the regions close to the walls (Chen *et al.*, 2023). As our PIV data are acquired at the mid-plane, information regarding the losses on the walls (next to shroud and hub) was not computed in the calculation of L_2.

Figure 5.17 presents the loss distributions obtained from L_2^* calculations at the different flow rates. It is evident that the L_2^* distributions within the impeller exhibit characteristics similar to the turbulence production fields. These results illustrate that a significant portion of the L_2 loss is attributed to the production of turbulent kinetic energy. For fully turbulent flow with high Reynolds numbers, the shear production term is generally larger compared to the dissipation term (Kundu & Cohen, 2008), which can explain the predominance of turbulence production in the loss distribution fields in the impeller.

At the BEP condition, $Q^* = 1.0$ (Fig. 5.17b), the energy delivered to the average flow field is converted into turbulent kinetic energy and later into losses mainly in the region close to impeller eye and surfaces of the blades. For the highest flow rate $Q^* = 1.5$ (Fig. 5.17c), the loss field exhibits a strong resemblance to that observed in the design condition. This outcome reinforces the notion that the flow field is directly associated with the obtained loss pattern. For conditions in which the flow rates are $Q^* > 1.0$, the dominant flow structures are characterized by small-scales. Consequently, the losses encountered in these conditions exhibit a similar pattern, owing to the similarity in flow structures (Fig. 5.1), both being comprised of smaller-scale structures (see Sec. 5.4).

Under the partial load condition $Q^* = 0.3$ (Fig. 5.17a), however, we observe a concentration of the largest L_2^* losses at the impeller's inlet and outlet regions. The conversion of energy into loss for this specific flow condition primarily arises from the intense shear formed between the recirculation zones in the pressure side and suction side of the blades (Figs. 5.1 and 5.4), as well as due to the shear flow near the impeller outlet due to differences in the angular speeds of impeller and volute (Fig. 5.15).

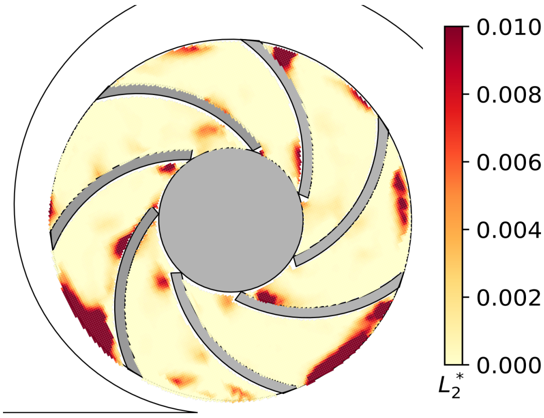

(A) $Q^* = 0.3$

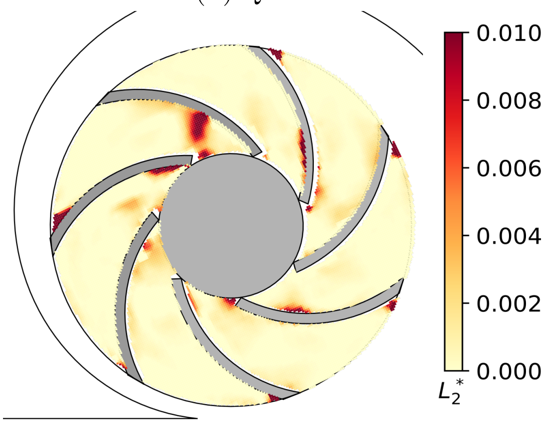

(B) $Q^* = 1.0$

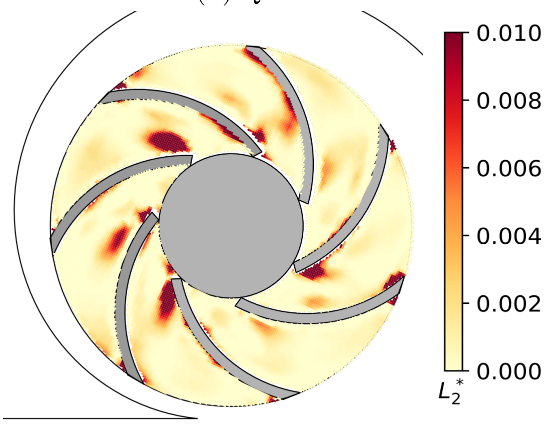

(C) $Q^* = 1.5$

FIGURE 5.17 – Energy loss contours (L_2^*) for different flow rates inside the centrifugal pump impeller (Fonseca *et al.*, 2024).

The analysis of the presented findings reveals a notable correlation between the turbulent flow field and energy losses within the centrifugal pump impeller.

6 Two-phase flow results

After acquiring data and results from the prototype centrifugal pump operating with single-phase water flow (Chapter 5), the experiments were expanded to include the analysis of the pump operating with two-phase mixtures of oil and water using the TR-PIV technique. Section 6.1 presents a new method for calculating the phase-ensemble average of TR-PIV acquisitions, in addition to investigating the impact of applying a deep learning method through neural networks on the flow field derived from TR-PIV measurements of two-phase liquid-liquid flow. Section 6.2 presents preliminary results on the influence of dispersed oil droplets on the flow fields of the continuous phase (water), utilizing the processing method introduced and validated in Sec. 6.1. These results encompass velocity fields the turbulent kinetic energy.

6.1 Comparison of flow fields with and without deep learning processing

The implementation of the PIV technique in two-phase liquid-liquid flows is not straightforward, requiring additional effort due to the presence of interfaces. These interfaces make such measurements significantly more intricate compared to single-phase flows. The primary challenge lies in distinguishing between the seeding particles that track the continuous phase and the dispersed oil droplets within this flow.

To overcome this challenge, a dynamic masking method is employed to mask the oil droplets from the TR-PIV image. This approach involves the development and training of a U-Net convolutional neural network (Sec. 4.2.1). The U-Net generates a binary mask, which is then utilized to remove the oil droplets from the image. The spectral random masking from Anders *et al.* (2019) is used to mask out the oil drops.

Figure 6.1 presents a sample TR-PIV image captured in the presence of oil droplets within the flow. These droplets are displayed in Fig. 6.1a, which compares a raw image taken without the laser illumination (left) and a raw PIV image with laser and tracers (right). Consequently, it is imperative to eliminate or mask these oil droplets from TR-PIV images. Failure to do so may result in frame-to-frame displacement of the oil droplets during the PIV cross-correlation process, thereby generating "spurious" velocity vectors. These vectors do not accurately represent the continuous flow where seeding particles are present. Furthermore, Fig. 6.1b illustrates the TR-PIV processing steps for the two-phase flow, emphasizing the dynamic masking process using the U-Net neural network and the PIV cross-correlation of these images, highlighting the process in a specific region of the pump impeller.

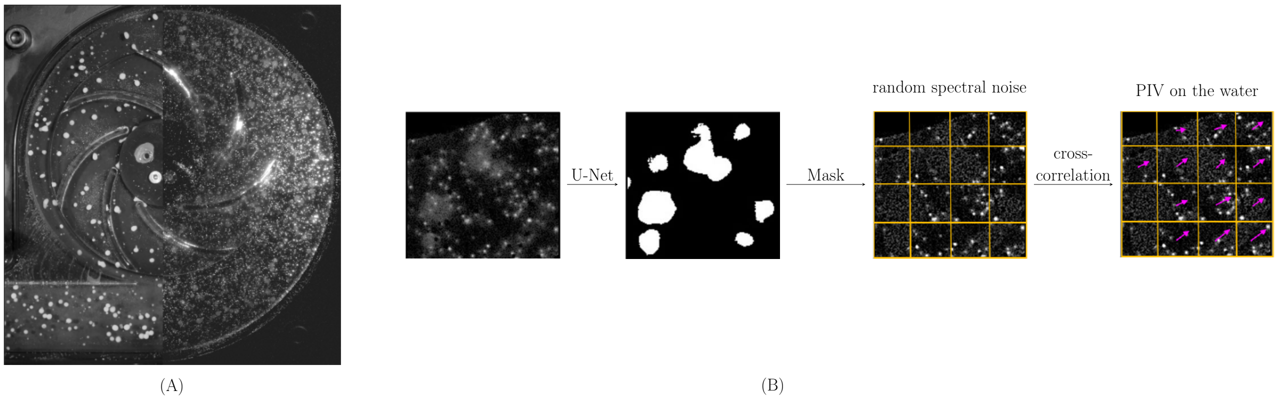

FIGURE 6.1 – (A) Left: high-speed camera image of the experimental apparatus and the produced dispersed oil-water two-phase flow. Right: raw image acquired during a TR-PIV acquisition; (B) Image processing steps of the U-Net technique.

As described in Sec. 3.5.2, PIV data acquisitions for two-phase flow were performed exclusively in automatic mode (double-frame TR-PIV). Due to the lack of symmetry in the centrifugal pump caused by the spiral volute, the average flow fields in each impeller channel depend on the angular position and are not acquired directly from TR-PIV measurements.

Therefore, an in-house MatLab® code was developed to calculate the average of TR-PIV acquisitions. This code, referred to as the "numeric rotary encoder," uses instantaneous fields that make up the average only for snapshots positioned between $8.75° \leq \theta \leq 11.25°$, with the reference position $\theta = 0°$ corresponding to the angle at which the tip of one of the lowest blades is vertically aligned with the tip of the volute tongue.

Based on the image acquisition frequency (700 Hz) and the rotational speed of the impeller ($\mathcal{N} = 300$ rpm), the impeller completes one full rotation every 140 frames. The impeller has a total of seven channels, so due to the periodicity of the geometry, one channel is in the same position every 20 frames. With a total of 4,000 images used for each experimental condition, 200 images were used to calculate phase-ensembled TR-PIV velocity fields.

To validate this methodology, we compared the average relative velocity fields obtained in automatic mode (Fig.6.2a) and triggered mode (Fig.6.2b) under the same operating condition of the pump ($\mathcal{N}$ = 300 rpm and $Q^* = 1.0$). As depicted in Fig. 6.2, the average flow characteristics exhibit strong similarity, with an average percentage error of 7% calculated from the average blade-to-blade velocity profile. With this reasonably low error, it can be concluded that the developed code for analyzing subsequent average flow fields derived from TR-PIV data performed satisfactorily.

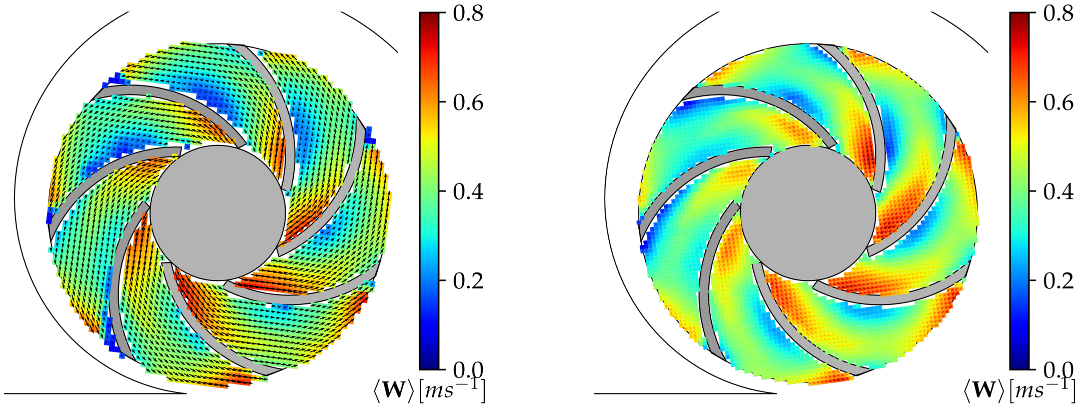

(A) time-resolved numeric encoder   (B) double-frame encoder

FIGURE 6.2 – Comparison of average relative velocity fields in single-phase water flow from PIV acquisitions using automatic mode and triggered mode.

Using the methodology presented, Fig. 6.3a displays the average relative velocity field without the dynamic masking procedure. In contrast, Fig. 6.3b shows the average velocity fields after applying dynamic masking. For comparison, Fig. 6.3c illustrates the average relative velocity field for the single-phase flow. These results are calculated for the condition of $Q^* = 0.3$ ($\mathcal{N} = 300$ rpm and $Q_w = 0.225$ m^3/h).

According to the results, not removing the oil droplets during PIV cross-correlation can cause velocity value discrepancies of up to 48% near the impeller inlet and outlet. In general, lower magnitude velocity fields remain unprocessed. As the oil droplets are "dragged" by the flow and move more slowly than the continuous phase, their spurious contribution results in lower velocity values in each interrogation window.

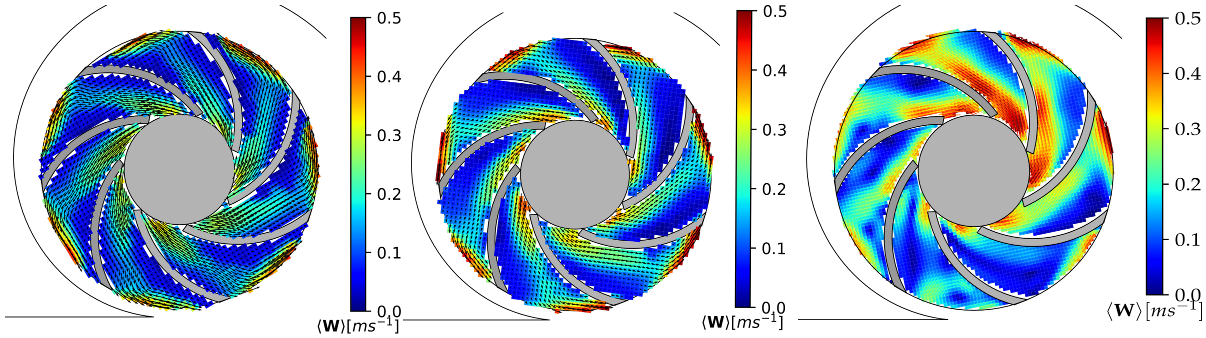

(A) result from raw PIV images (B) DL-based image processing (C) single-phase result

FIGURE 6.3 – Comparison of velocity fields with and without deep learning (DL) processing.

Furthermore, we can observe an inversion in the velocity values between the pressure and suction blades in cases without the dynamic masking procedure (Fig. 6.3a) compared to those after the application of dynamic masking (Fig. 6.3b). This inversion is due to the accumulation of oil droplets carried by the water flow on the suction blade, a consequence of recirculation zones within the continuous water phase flow (see Fig. 5.1). In the case depicted in Fig. 6.3a, since the oil droplets are not removed during the PIV cross-correlation step, they significantly contribute to spurious velocity values of the continuous phase. This occurs because the PIV cross-correlation algorithm detects frame-to-frame displacement of white pixels, which in these regions (suction blade) are occupied by oil droplets doped with white dye.

As discussed in Sec. 3.2.2, for the low oil-in-water fractions employed in this study, the pump head did not show significant variations. This is because the head depends on both the pressure term, which is the same for both single-phase and two-phase cases, and the kinetic energy of the mean flow, resulting in similar velocity fields of the continuous phase in both scenarios (single and two-phase flow). Figures 6.3b and 6.3c illustrate similar characteristics, differing only in the magnitude of velocity values. As previously discussed, this difference is attributed to the presence of the dispersed phase, which moves more slowly than the continuous phase. Based on this discussion, it is evident that the method using dynamic masking through the U-Net network has a solid physical basis and can be employed in subsequent analyses of the two-phase flow.

When analyzing the influence of the U-Net pre-processing method on the turbulent kinetic energy field of the two-phase flow, it is observed that, in the impeller inlet region, the failure to remove the dispersed droplets from the TR-PIV images causes turbulent regions, particularly in the circular injection section of the dispersed phase into the flow (Fig. 6.4a). When the dynamic masking method is applied (Fig. 6.4b), these turbulent structures are attenuated. In contrast, at the leading edge of the suction blade, after the masking is applied, the turbulent kinetic energy values are higher. Additionally, in the impeller outlet region, the failure to remove the dispersed droplets intensifies the turbulent kinetic energy zones. This can be attributed to the "trapping" caused by vortex structures of the continuous phase, which retain a set of droplets before they exit the impeller section into the volute. As the dispersed droplets remain in these regions, recirculating with the seeding particles, they spuriously contribute to the instantaneous velocity field and, consequently, to the turbulent kinetic energy.

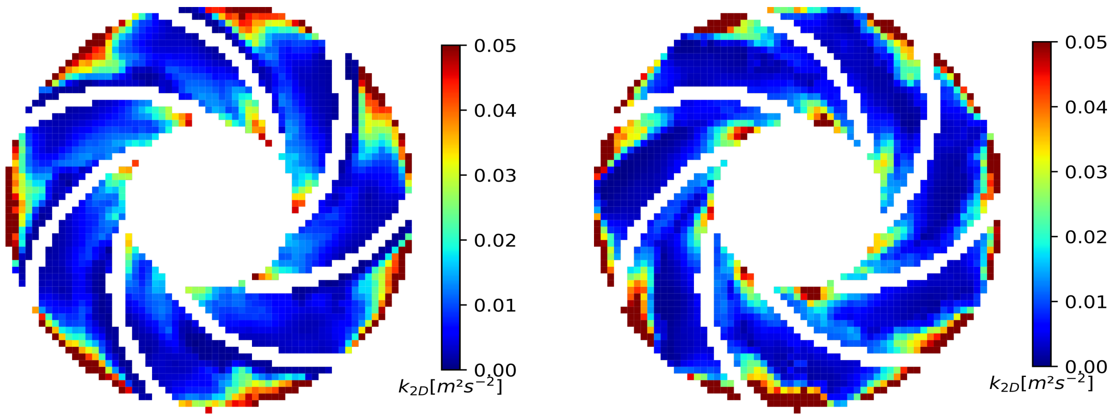

(A) result from raw PIV images (B) DL-based image processing

FIGURE 6.4 – Comparison of turbulent kinetic energy fields with and without deep learning (DL) processing.

6.2 Velocity and turbulent kinetic energy fields of the two-phase liquid-liquid flow

To investigate the influence of the dispersed oil on the water flow field, the instantaneous two-phase fields were pre-processed using the dynamic masking procedure and calculated with the angular average flow procedure (numeric rotary encoder). The results were then compared with single-phase results under similar operating conditions. The analyses were conducted at a rotation speed of 300 rpm, with continuous phase flow rates (Q^*) of 0.3, 0.5, and 0.7.

Figures 6.5a and 6.5b show the average relative velocity field of the two-phase and single-phase flows, respectively, for the condition of $Q^* = 0.3$. It can be seen that the presence of dispersed droplets in the two-phase flow (Fig. 6.5a) reduces the velocity of the jets at the inlet of the channels to the right of the impeller. In contrast, in the suction blades of the channels close to the volute tongue (to the left of the impeller), recirculation zones develop in the single-phase case (Fig. 6.5b) due to the unbalance of apparent forces and the geometric restriction imposed by the volute, as discussed in Sec. 5.1. However, the presence of dispersed droplets in the flow delays or even prevents the formation of these vortex structures. This inhibition occurs because the oil droplets act as physical obstacles that interrupt the continuity of the water flow, dispersing kinetic energy. Consequently, this decreases the intensity of the jets and reduces the flow's ability to form unstable vortices.

As the flow rate of the continuous phase increases to $Q^* = 0.5$ (Figs. 6.5c and 6.5d), similar flow field structures are observed throughout all impeller channels. Because the flow rate is inversely proportional to the size of the dispersed droplets (Perissinotto *et al.*, 2019b), due to its reduced size, the small dispersed oil drops do not have a large impact in the of impeller channels flow pattern. This characteristic is also observed for $Q^* = 0.7$ (Figs. 6.5e and 6.5f), where a notable similarity in flow structures can be seen between the two-phase and single-phase cases, especially in the channels towards the right side of the impeller, differing only in the magnitude of the relative velocity. However, in the channels near the volute tongue, it is observed that the jets originating at the impeller inlet in the suction regions of the blades are more intense in the two-phase case (Fig. 6.5e), particularly in the regions at the impeller outlet.

Figure 6.6 shows examples of instantaneous fields of the two-phase flow for the different flow conditions analyzed. On the left side, raw TR-PIV images are presented for different acquisition times, while the figures on the right side present the instantaneous relative velocity fields for the same acquisition times. As can be observed, the dispersed droplets break into smaller and smaller droplets as Q^* increases, confirming the observations of Perissinotto *et al.* (2019b). Additionally, from the instantaneous velocity fields for the conditions $Q^* = 0.3$ and 0.5, we can observe that the vortex structures are less prominent compared to similar operating conditions for single-phase flow. It is also noted that in the condition of $Q^* = 0.7$, jets form near the impeller suction blades.

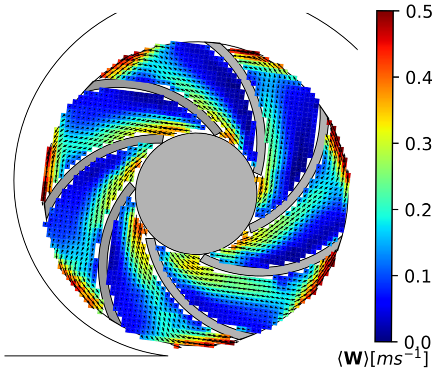

(A) two-phase liquid-liquid - $Q^* = 0.3$

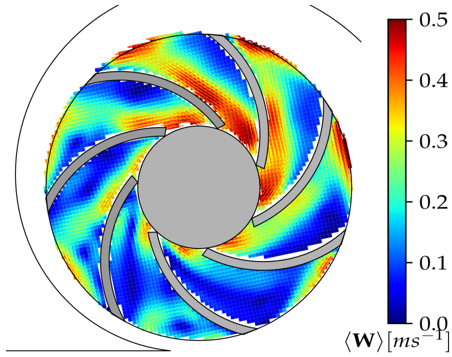

(B) single-phase - $Q^* = 0.3$

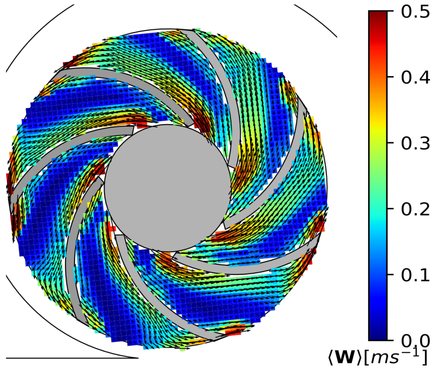

(C) two-phase liquid-liquid - $Q^* = 0.5$

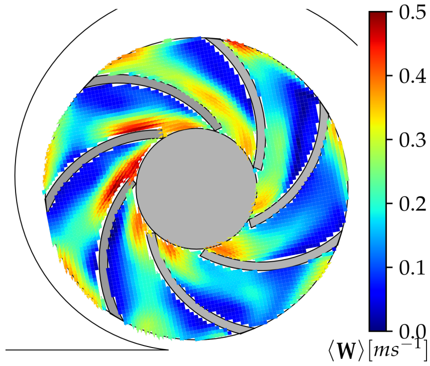

(D) single-phase - $Q^* = 0.5$

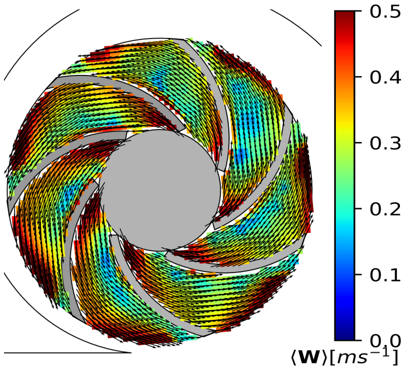

(E) two-phase liquid-liquid - $Q^* = 0.7$

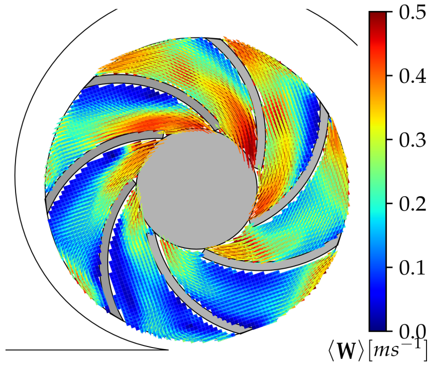

(F) single-phase - $Q^* = 0.7$

FIGURE 6.5 – Average relative velocity fields of two-phase liquid-liquid flow (left) and single-phase flow (right) in a centrifugal pump impeller.

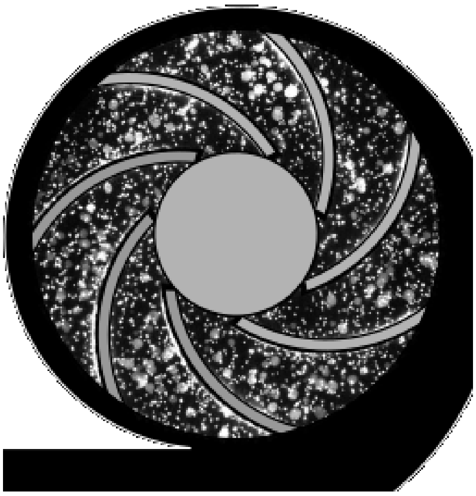

(A) $Q^* = 0.3$; $t = 0.0$ s

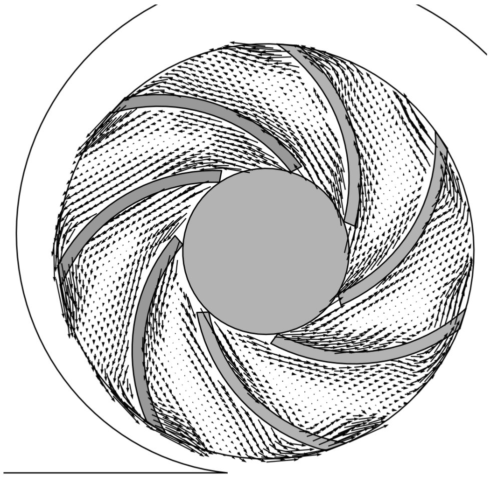

(B) $Q^* = 0.3$; $t = 0.0$ s

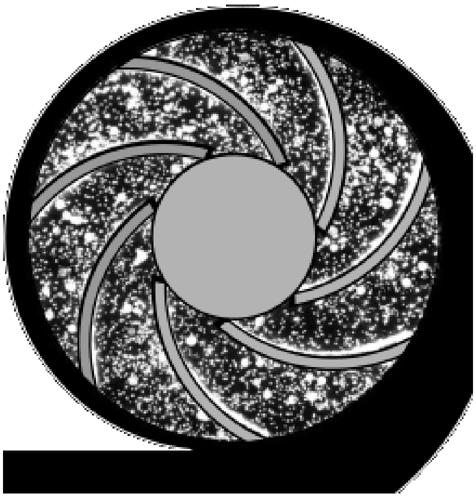

(C) $Q^* = 0.5$; $t = 0.016$ s

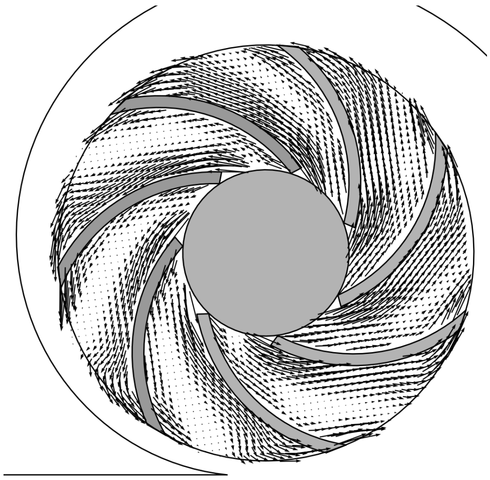

(D) $Q^* = 0.5$; $t = 0.016$ s

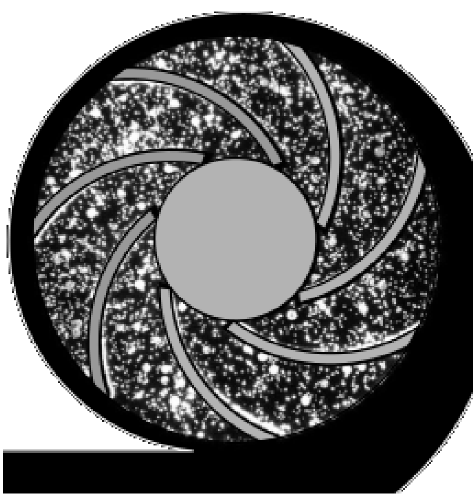

(E) $Q^* = 0.7$; $t = 0.031$ s

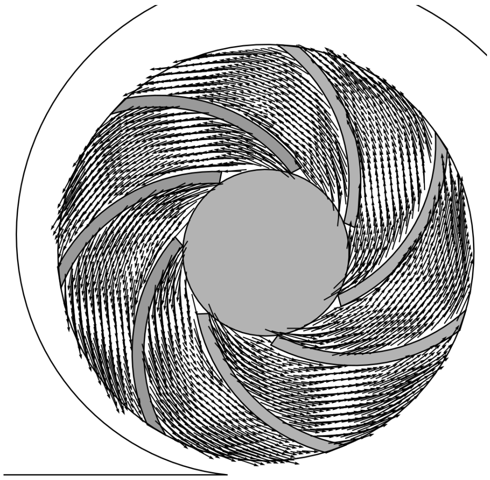

(F) $Q^* = 0.7$; $t = 0.031$ s

FIGURE 6.6 – Raw TR-PIV images of two-phase liquid-liquid flow (left) and instantaneous velocity fields (right) in a centrifugal pump impeller.

The turbulent kinetic energy fields for the two-phase and single-phase flows are shown in Fig. 6.7.

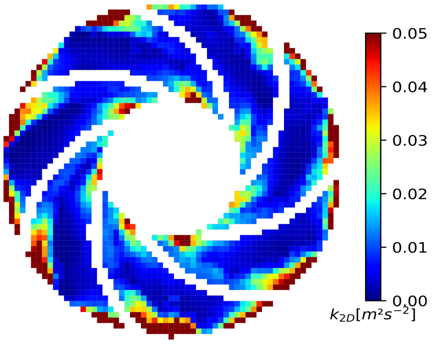

(A) two-phase liquid-liquid - $Q^* = 0.3$

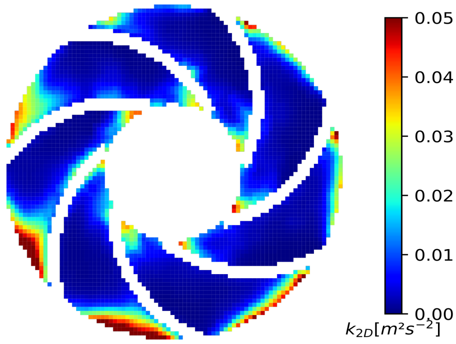

(B) single-phase - $Q^* = 0.3$

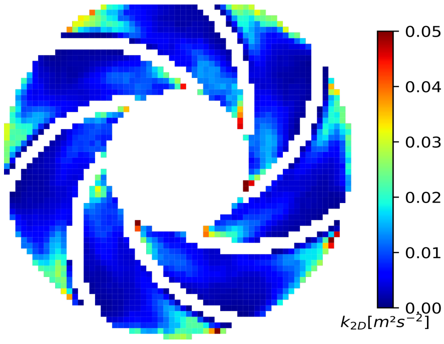

(C) two-phase liquid-liquid - $Q^* = 0.5$

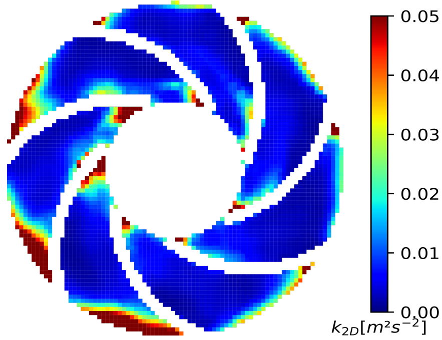

(D) single-phase - $Q^* = 0.5$

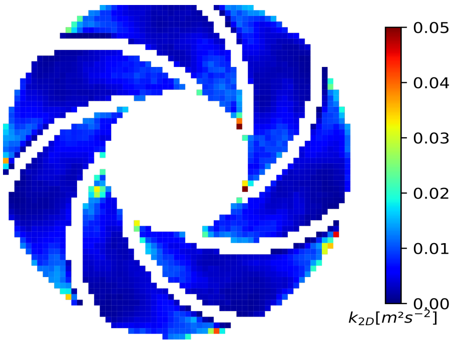

(E) two-phase liquid-liquid - $Q^* = 0.7$

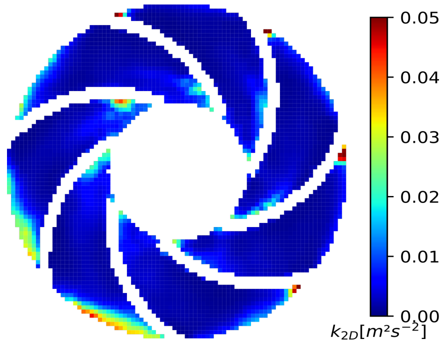

(F) single-phase - $Q^* = 0.7$

FIGURE 6.7 – Average turbulent kinetic energy fields of two-phase liquid-liquid flow (left) and single-phase flow (right) in a centrifugal pump impeller.

It is observed that the TKE fields exhibit a similar distribution throughout the domain for the two-phase cases, with higher values near the inlet and outlet sections of the impeller channel. Additionally, as the continuous phase approaches the design flow rate, the TKE values of the two-phase flow decrease. This result suggests a relationship between the size of the dispersed droplets and the TKE values.

When comparing the two-phase results with their respective single-phase cases, we observe significant changes in the TKE fields, especially in the regions at the exit of the impeller. This difference is most pronounced for $Q^* = 0.3$, due to the substantial deceleration of the dispersed droplets as they transition from the rotating impeller to the stationary volute. Although the droplets slow down, their turbulent kinetic energy increases in the two-phase flow. This phenomenon occurs because the deceleration of the droplets enhances the relative velocity fluctuations between the droplets and the continuous phase.

The results presented in this section elucidate several characteristics of liquid-liquid two-phase flows within centrifugal pump impellers. Additionally, they introduce a coupled TR-PIV/CNN methodology for evaluating complex two-phase flow fields.

7 Conclusions

This PhD thesis presents the principal results of an experimental investigation into single-phase and two-phase liquid-liquid flows within a centrifugal pump impeller. To facilitate these tests, a novel centrifugal pump prototype was designed and manufactured with transparent components, allowing optical access to the internal flow. Additionally, a TR-PIV system was employed for flow measurement. The following sections detail the key observations and interpretations derived from this study, focusing on single-phase (Sec. 7.1) and two-phase (Sec. 7.2) flow dynamics.

7.1 Single-phase flow

1. From the averages of relative velocities, we show that several recirculation regions develop in the impeller for a flow rate of $Q^* = 0.3$. This occurs due to a change in the stagnation point, which is a consequence of the unbalance of apparent forces at this flow condition. This flow pattern is observed for all rotation speeds investigated. At the flow corresponding to the BEP ($Q^* = 1.0$), the streamlines follow the curvature of the blades without significant flow separation for the three rotational speeds. As the flow rate increases to $Q^* = 1.5$, the formation of small instabilities is detected on the pressure side of the blades in different radial positions of the impeller, which may be associated with the detachment of the boundary layer.

2. The vorticity fields showed significant backflow near the volute tongue for the low flow rate condition ($Q^* = 0.3$). For $Q^* = 1.0$, localized areas of positive vorticity were observed near the rotor eye and pressure blades in channels distant from the volute tongue, while $Q^* = 1.5$ exhibited a relatively uniform vorticity distribution along the impeller across all channels.

3. From the turbulent kinetic energy, we show that the highest turbulence values are detected at the lowest flow rate ($Q^* = 0.3$), especially next to the impeller exit. In opposition,

for the design ($Q^* = 1.0$) and highest flow rates ($Q^* = 1.5$), the turbulent kinetic energy presents lower values. This fact is a consequence of the flow uniformity, as the apparent forces are balanced for these two last conditions.

4. From the POD analyses for the low flow rate condition ($Q^* = 0.3$), the first pair of modes are correlated, and 50% of the total turbulent energy is contained in these modes. Such results suggest the occurrence of possible coherent structures for this pump operating condition, for the three rotational speeds studied in this paper. As the flow rate increases to the design point ($Q^* = 1.0$), the flow tends to be well-behaved, so that more POD modes are needed for the reconstruction of the flow. This is an indication that this condition is dominated by turbulent structures of smaller scales. The same is observed for the higher flow rate ($Q^* = 1.5$).

5. From the temporal characteristics of the flow, we conclude that the unstable flow structures with higher energy levels are formed at a frequency comparable to the pump rotation speed. Then, these structures break up at harmonic frequencies. In other words, these structures are initially coherent, but then they break up into smaller vortices through the cascade effect.

6. At the design condition ($Q^* = 1.0$), turbulence production exhibited notably low values throughout most regions, except for areas near the impeller inlet. Under part-load conditions ($Q^* = 0.3$), localized regions of intense turbulence production were observed near the impeller inlet and outlet. Conversely, at a higher flow rate ($Q^* = 1.5$), turbulence production was intensified on the surface of the blades, particularly close to the entrance of each channel. Additionally, turbulence production was detected in peripheral regions of the channels, associated with vorticity released from the trailing edge of the blades and high viscous stresses.

7. For the low flow rate condition, regions of high energy dissipation correspond to locations of high vorticity in the impeller, suggesting that a portion of the energy generated is dissipated within the pump component. Nevertheless, the design condition demonstrates considerably smaller values of turbulent dissipation, implying reduced turbulence due to

the absence or decreased presence of vortical structures. At the highest flow rate condition, the impeller eye experiences a higher dissipation rate compared to $Q^* = 0.3$ and $Q^* = 1.0$. In addition, dissipation is higher on the pressure side of the blades than the suction side, attributed to flow separation predominantly occurring on the pressure side.

8. The loss distributions calculated from the flow kinetic energy equation exhibit analogous features to the patterns observed in turbulence production fields. Moreover, our findings provide additional support for the notion that the flow field is intimately linked to the observed loss patterns. In situations where flow rates exceed $Q^* > 1.0$, the prevailing flow structures are marked by small-scale features, structures attributed primarily to turbulence dissipation. On the other hand, in cases of low flow rates, large-scale structures dominate, resulting in energy loss primarily driven by turbulence production.

9. The quantitative results obtained through the modeling adopted for the calculations of L_2 disagreed reasonably with the results taken directly from the experimental instrumentation L_1. This is associated with the physical model adopted to calculate L_2 which implicitly assumes dynamic equilibrium. This assumption allows us to approximate the turbulence dissipation rate by measuring the total kinetic energy flow from the resolved to the unresolved scale (SGS flow). It is also important to note that, like all turbulence models, the model employed to calculate the subgrid-scale stress tensor, τ_{ij}, has physical limitations. Moreover, the inherent limitation of data acquisition restricted to a two-dimensional (2D) plane offers only a limited view of the complex flow dynamics occurring in the centrifugal pump impeller. It is thus evident that a comprehensive understanding of these phenomena needs the acquisition of fully resolved three-component velocity as a function of time. Even so, we can then conclude that investigations using the L_2 method can be used, considering their limitations, as an alternative for analyzing losses in centrifugal pump impellers.

7.2 Two-phase flow

1. Failure to apply dynamic masking in TR-PIV images of two-phase flow results in an inversion of the velocity values between the pressure and suction blades. This inversion occurs due to the accumulation of oil droplets transported by the water flow to the suction blade, which is a consequence of recirculation zones within the aqueous phase.

2. Despite differences in the magnitude of the velocity values caused by the presence of dispersed oil droplets, the velocity field of the continuous phase in two-phase flow closely resembles that of single-phase flow. This similarity is due to the fact that the pump head remains approximately the same for both flow types.

3. At lower flow rates ($Q^* = 0.3$), the dispersed droplets reduce the velocity of the jets at the inlet of the channels and inhibit the formation of vortex structures near the volute tongue. This is because the oil droplets act as physical obstacles, disrupting the water flow and dispersing kinetic energy, which decreases jet intensity and reduces vortex formation.

4. As the flow rate of the continuous phase increases ($Q^* = 0.5$ and $Q^* = 0.7$), the size of the dispersed droplets decreases, leading to a reduction in their impact on the flow field. This results in flow structures that are increasingly similar to those observed in single-phase flow, with higher TKE values near the impeller's inlet and outlet. The decrease in TKE values with higher flow rates suggests that smaller droplets contribute less to turbulence, aligning more closely with the continuous phase and reducing the overall turbulence.

7.3 Future works

Based on the raw TR-PIV data generated in this PhD work, the following future activities are suggested:

- Evaluate the unsteady flow in the centrifugal pump impeller using a coupled approach of triple decomposition and proper orthogonal decomposition to analyze the coherent flow structures;
- Analyze the unstable flow inside the centrifugal pump impeller, particularly the evolution of the dynamic stall phenomenon, using the DMD and EMD modal decomposition techniques to address the limitations of the POD technique described in Sec. 5.4;
- Estimate the velocity field from PIV data using a reduced-order model based on Galerkin projection;
- Conduct an analysis using a coupled approach of triple decomposition and proper orthogonal decomposition to examine the influence of dispersed oil droplets in the unstable flow field in the centrifugal pump impeller;
- Perform a Lagrangian analysis using the PTV technique to characterize the kinematics and dynamics of oil drops in the two-phase liquid-liquid flow;
- Perform coupled PTV-PIV analysis to determine and evaluate the interfacial moment closure correlations of dispersed two-phase flow;
- To validate the consideration of "almost" two-dimensional turbulence and inverse energy cascade, as described in Sec. 5.5, propose conducting a CFD analysis varying the flow direction in the z-axis (6 mm in this work) to validate this observation.

Bibliography

ABADI, M., AGARWAL, A., BARHAM, P., BREVDO, E., *ET AL.* 2015. *TensorFlow: Large-scale machinelearning on heterogeneous systems.* `https://www.tensorflow.org/?hl=pt-br`.

ABRANTES, J. K., PAULA, I. B., & AZEVEDO, L. F. A. 2012. Medição de escoamentos turbulentos utilizando velocimetria por imagem de partículas. *Capítulo*, **5**, 133–209.

ADRIAN, R. J. 1984. Scattering particle characteristics and their effect on pulsed laser measurements of fluid flow: speckle velocimetry vs particle image velocimetry. *Applied optics*, **23**(11), 1690–1691.

ADRIAN, R. J. 1991. Particle-imaging techniques for experimental fluid mechanics. *Annual review of fluid mechanics*, **23**(1), 261–304.

ADRIAN, R. J. 1997. Dynamic ranges of velocity and spatial resolution of particle image velocimetry. *Measurement Science and Technology*, **8**(12), 1393.

ADRIAN, R. J. 2005. Twenty years of particle image velocimetry. *Experiments in fluids*, **39**(2), 159–169.

ADRIAN, R. J., & WESTERWEEL, J. 2011. *Particle image velocimetry.* Cambridge university press.

ANDERS, S., NOTO, D., SEILMAYER, M., & ECKERT, S. 2019. Spectral random masking: a novel dynamic masking technique for PIV in multiphase flows. *Experiments in Fluids*, **60**, 1–6.

ANGELI, P., & HEWITT, G. F. 2000. Flow structure in horizontal oil–water flow. *International journal of multiphase flow*, **26**(7), 1117–1140.

BAJ, P., BRUCE, P. J. K., & BUXTON, O. R. H. 2015. The triple decomposition of a fluctuating velocity field in a multiscale flow. *Physics of Fluids*, **27**(7).

Barrios, L., & Prado, M. G. 2009a. Experimental visualization of two phase flow inside an electrical submersible pump stage. *Pages 453–467 of: International Conference on Offshore Mechanics and Arctic Engineering*, vol. 43475.

Barrios, L., & Prado, M. G. 2009b. Modeling two phase flow inside an electrical submersible pump stage. *Pages 469–484 of: International Conference on Offshore Mechanics and Arctic Engineering*, vol. 43475.

Batchelor, G. K. 1969. Computation of the energy spectrum in homogeneous two-dimensional turbulence. *The Physics of Fluids*, **12**(12), II–233. Batchelor's 1969.

Bradski, G. 2000. The openCV library. *Dr. Dobb's Journal: Software Tools for the Professional Programmer*, **25**(11), 120–123.

Brauner, N., & Maron, D. M. 1992. Flow pattern transitions in two-phase liquid-liquid flow in horizontal tubes. *International journal of multiphase flow*, **18**(1), 123–140.

Buchhave, P. 1992. Particle image velocimetry—status and trends. *Experimental Thermal and Fluid Science*, **5**(5), 586–604.

Bulgarelli, N. A. V., Biazussi, J. L., Monte Verde, W., Castro, M. S., & Bannwart, A. C. 2020. Experimental study of phase inversion phenomena in electrical submersible pumps under oil/water flow. *Journal of Offshore Mechanics and Arctic Engineering*, **142**(4), 041402.

Bulgarelli, N. A. V., Biazussi, J. L., Monte Verde, W., Perles, C. E., Castro, M. S., & Bannwart, A. C. 2021a. Experimental investigation on the performance of Electrical Submersible Pump (ESP) operating with unstable water/oil emulsions. *Journal of Petroleum Science and Engineering*, **197**, 107900.

Bulgarelli, N. A. V., Biazussi, J. L., Monte Verde, W., Perles, C. E., Castro, M. S., & Bannwart, A. C. 2021b. Relative viscosity model for oil/water stable emulsion flow within electrical submersible pumps. *Chemical Engineering Science*, **245**, 116827.

Bulgarelli, N. A. V., Biazussi, J. L., Monte Verde, W., Perles, C. E., Castro, M. S., & Bannwart, A. C. 2022. A novel criterion based on slip ratio to assess the flow behavior of W/O emulsions within centrifugal pumps. *Chemical Engineering Science*, **247**, 117050.

Burden, R. L., Faires, J. D., & Burden, A. M. 2015. *Numerical analysis*. Cengage learning.

Cantwell, B., & Coles, D. 1983. An experimental study of entrainment and transport in the turbulent near wake of a circular cylinder. *Journal of fluid mechanics*, **136**, 321–374.

Cavicchio, C. A. M., Biazussi, J. L., Castro, M. S., Bannwart, A. C., Rodriguez, O. M. H., & Carvalho, C. H. M. 2018. Experimental study of viscosity effects on heavy crude oil-water core-annular flow pattern. *Experimental Thermal and Fluid Science*, **92**, 270–285.

Cerqueira, R. F. L., & Paladino, E. E. 2021. Development of a deep learning-based image processing technique for bubble pattern recognition and shape reconstruction in dense bubbly flows. *Chemical Engineering Science*, **230**, 116163.

Cerqueira, R. F. L., Perissinotto, R. M., Monte Verde, W., Biazussi, J. L., Castro, M. S., & Bannwart, A. C. 2023. Development and assessment of a particle tracking velocimetry (PTV) measurement technique for the experimental investigation of oil drops behaviour in dispersed oil–water two-phase flow within a centrifugal pump impeller. *International Journal of Multiphase Flow*, **159**, 104302.

Charles, R. H., K. Jarrod, M., Stéfan, J. W., Ralf, G., et al. 2020. Array programming with NumPy. *Nature*, **585**(7825), 357–362.

Chen, B., Li, X., & Zhu, Z. 2022a. Investigations of energy distribution and loss characterization in a centrifugal impeller through PIV experiment. *Ocean Engineering*, **247**, 110773.

Chen, B., Li, X., & Zhu, Z. 2022b. Time-resolved particle image velocimetry measurements and proper orthogonal decomposition analysis of unsteady flow in a centrifugal impeller passage. *Frontiers in Energy Research*, **9**, 818232.

Chen, B., Yu, L., Li, X., & Zhu, Z. 2024. Insights into turbulent flow structure and energy dissipation in centrifugal pumps: A study utilizing time-resolved particle image velocimetry and proper orthogonal decomposition. *Ocean Engineering*, **304**, 117903.

Chen, W., Li, Y., Liu, Z., & Hong, Y. 2023. Understanding of energy conversion and losses in a centrifugal pump impeller. *Energy*, **263**, 125787.

Christensen, E. A., Brøns, M., & Sørensen, J. N. 1999. Evaluation of proper orthogonal decomposition–based decomposition techniques applied to parameter-dependent nonturbulent flows. *SIAM Journal on Scientific Computing*, **21**(4), 1419–1434.

Cimarelli, A., Leonforte, A., De Angelis, E., Crivellini, A., & Angeli, D. 2019. On negative turbulence production phenomena in the shear layer of separating and reattaching flows. *Physics Letters A*, **383**(10), 1019–1026.

Cubas, J. M. C., Stel, H., Ofuchi, E. M., Neto, M. A. M., & Morales, R. E. M. 2020. Visualization of two-phase gas-liquid flow in a radial centrifugal pump with a vaned diffuser. *Journal of Petroleum Science and Engineering*, **187**, 106848.

Davidson, P. A. 2015. *Turbulence: an introduction for scientists and engineers*. 2 edn. Oxford university press.

Delafosse, A., Collignon, M., Crine, M., & Toye, D. 2011. Estimation of the turbulent kinetic energy dissipation rate from 2D-PIV measurements in a vessel stirred by an axial Mixel TTP impeller. *Chemical Engineering Science*, **66**(8), 1728–1737.

Dong, R., Chu, S., & Katz, J. 1992a. Quantitative visualization of the flow within the volute of a centrifugal pump. Part A: Technique. *Journal of Fluids Engineering*, **114**(1), 390–395.

Dong, R., Chu, S., & Katz, J. 1992b. Quantitative visualization of the flow within the volute of a centrifugal pump. Part B: results and analysis. *Journal of Fluids Engineering*, **114**(1), 396–403.

Ducci, A., & Yianneskis, M. 2005. Direct determination of energy dissipation in stirred vessels with two-point LDA. *AIChE journal*, **51**(8), 2133–2149.

Duncan, J., Dabiri, D., Hove, J., & Gharib, M. 2010. Universal outlier detection for particle image velocimetry (PIV) and particle tracking velocimetry (PTV) data. *Measurement Science and Technology*, **21**(5), 057002.

El-Adawy, M., Heikal, M. R., Aziz, A. R. A., Adam, I. K., *et al.* 2018. On the application of proper orthogonal decomposition (POD) for in-cylinder flow analysis. *Energies*, **11**(9), 2261.

Elsinga, G. E., Wieneke, B., Scarano, F., & Schröder, A. 2008. Tomographic 3D-PIV and applications. *Pages 103–125 of: Particle Image Velocimetry: New Developments and Recent Applications.* Springer.

Ertürk, N., Vernet, A., Pallares, J., Castilla, R., & Raush, G. 2013. Small-scale characteristics and turbulent statistics of the flow in an external gear pump by time-resolved PIV. *Flow Measurement and Instrumentation*, **29**, 52–60.

Estevan, V. 2002. *Uma análise fenomenológica da operação de bomba centrífuga com escoamento bifásico.* Ph.D. thesis, University of Campinas.

Feng, J., Benra, F. K., & Dohmen, H. J. 2009. Comparison of periodic flow fields in a radial pump among CFD, PIV, and LDV results. *International Journal of Rotating Machinery*, **410838**.

Feng, J., Ge, Z., Yang, H., Zhu, G., Li, C., & Luo, X. 2021. Rotating stall characteristics in the vaned diffuser of a centrifugal pump. *Ocean Engineering*, **229**, 108955.

Fogleman, M., Lumley, J. L., Rempfer, D., & Haworth, D. 2004. Application of the proper orthogonal decomposition to datasets of internal combustion engine flows. *Journal of Turbulence*, **5**(1), 023.

Fonseca, W. D. P., Cerqueira, R. F. L., Perissinotto, R. M., Monte Verde, W., Castro, M. S., & Franklin, E. M. 2023. Particle image velocimetry in the impeller of a centrifugal pump: A POD-based analysis. *Flow Measurement and Instrumentation*, **94**, 102483.

Fonseca, W. D. P., Perissinotto, R. M., Cerqueira, R. F. L., Monte Verde, W., Castro, M. S., & Franklin, E. M. 2024. Particle image velocimetry in the impeller of a centrifugal pump: Relationship between turbulent flow and energy loss. *Flow Measurement and Instrumentation*, **99**, 102675.

Gabriele, A., Nienow, A. W., & Simmons, M. J. H. 2009. Use of angle resolved PIV to estimate local specific energy dissipation rates for up-and down-pumping pitched blade agitators in a stirred tank. *Chemical Engineering Science*, **64**(1), 126–143.

Gabriele, A., Tsoligkas, A. N., Kings, I. N., & Simmons, M. J. H. 2011. Use of PIV to measure turbulence modulation in a high throughput stirred vessel with the addition of high Stokes number particles for both up-and down-pumping configurations. *Chemical engineering science*, **66**(23), 5862–5874.

Golub, G. H., & Van Loan, C. F. 2013. *Matrix computations.* JHU press.

Gordeyev, S. V., & Thomas, F. O. 2000. Coherent structure in the turbulent planar jet. Part 1. Extraction of proper orthogonal decomposition eigenmodes and their self-similarity. *Journal of Fluid Mechanics*, **414**, 145–194.

Gordeyev, S. V., & Thomas, F. O. 2002. Coherent structure in the turbulent planar jet. Part 2. Structural topology via POD eigenmode projection. *Journal of Fluid Mechanics*, **460**, 349–380.

Grassi, B., Strazza, D., & Poesio, P. 2008. Experimental validation of theoretical models in two-phase high-viscosity ratio liquid–liquid flows in horizontal and slightly inclined pipes. *International journal of multiphase flow*, **34**(10), 950–965.

Gülich, J. F. 2008. *Centrifugal pumps.* Vol. 2. Springer.

Gulli, A., & Pal, S. 2017. *Deep learning with Keras.* Packt Publishing Ltd.

GUO, R., LI, R., & ZHANG, R. 2019. Reconstruction and prediction of flow field fluctuation intensity and flow-induced noise in impeller domain of jet centrifugal pump using gappy pod method. *Energies*, **12**(1), 111.

HART, D. P. 2000. PIV error correction. *Experiments in fluids*, **29**(1), 13–22.

HINZE, J. O. 1994. *Turbulence*. McGraw-Hill.

HOQUE, M. M., SATHE, M. J., MITRA, S., JOSHI, J. B., & EVANS, G. M. 2015. Comparison of specific energy dissipation rate calculation methodologies utilising 2D PIV velocity measurement. *Chemical Engineering Science*, **137**, 752–767.

HSIEH, K., LIEN, F., & YEE, E. 2010. Towards a unified turbulence simulation approach for wall-bounded flows. *Flow, turbulence and combustion*, **84**, 193–218.

HUSSAIN, A. K. M. F., & REYNOLDS, W. C. 1970. The mechanics of an organized wave in turbulent shear flow. *Journal of Fluid mechanics*, **41**(2), 241–258.

IBRAHIM, S. Y., & MALOKA, I. E. 2006. Emulsification of secondary oil/water dispersions using a centrifugal pump. *Petroleum science and technology*, **24**(5-6), 513–522.

ILAK, M., & ROWLEY, C. W. 2008. Modeling of transitional channel flow using balanced proper orthogonal decomposition. *Physics of Fluids*, **20**(3), 034103.

JAMIL, A., BAHAROM, M. B., & AZIZ, A. R. A. 2021. IC engine in-cylinder cold-flow analysis–A critical review. *Alexandria Engineering Journal*, **60**(3), 2921–2945.

JIA, X., ZHANG, Y., LV, HAO, & ZHU, ZUCHAO. 2023. Study on external performance and internal flow characteristics in a centrifugal pump under different degrees of cavitation. *Physics of Fluids*, **35**(1).

KEANE, R. D., & ADRIAN, R. J. 1990. Optimization of particle image velocimeters. I. Double pulsed systems. *Measurement science and technology*, **1**(11), 1202.

KEANE, R. D., & ADRIAN, R. J. 1992. Theory of cross-correlation analysis of PIV images. *Applied scientific research*, **49**(3), 191–215.

Keller, J., Blanco, E., Barrio, R., & Parrondo, J. 2014. PIV measurements of the unsteady flow structures in a volute centrifugal pump at a high flow rate. *Experiments in Fluids*, **55**(10), 1–14.

Krause, N., Zähringer, K., & Pap, E. 2005. Time-resolved particle imaging velocimetry for the investigation of rotating stall in a radial pump. *Experiments in Fluids*, **39**(2), 192–201.

Kundu, P. K., & Cohen, I. M. 2008. *Fluid Mechanics 4th*. Elsevier.

Laine, Q., Randriamanantena, T., Lamadie, F., & Olmos, E. 2023. Experimental study of velocity and turbulence fields in a square mixer-settler tank: Comparison of shake the box PTV and 2D2C PIV. *Chemical Engineering Science*, **275**, 118636.

Li, Huokun, Lin, Hongkang, Huang, Wei, Li, Jiazhen, Zeng, Min, Ma, Jiming, & Hu, Xin. 2021. A new prediction method for the complete characteristic curves of centrifugal pumps. *Energies*, **14**(24), 8580.

Li, X., Chen, B., Luo, X., & Zhu, Z. 2020a. Effects of flow pattern on hydraulic performance and energy conversion characterisation in a centrifugal pump. *Renewable Energy*, **151**, 475–487.

Li, X., Chen, H., Chen, B., Luo, X., Yang, B., & Zhu, Z. 2020b. Investigation of flow pattern and hydraulic performance of a centrifugal pump impeller through the PIV method. *Renewable Energy*, **162**, 561–574.

Liberge, E., & Hamdouni, A. 2010. Reduced order modelling method via proper orthogonal decomposition (POD) for flow around an oscillating cylinder. *Journal of Fluids and Structures*, **26**(2), 292–311.

Liu, X., Li, Y., Liu, Z., Yang, W., & Tao, R. 2022. Dynamic evolution process of rotating stall vortex based on high-frequency PIV system in centrifugal impeller. *Ocean Engineering*, **259**, 111944.

Liu, X. D., Liu, Z., Zhong, Q., Li, Y., & Yang, W. 2021. Experimental investigation of relative velocity field based on image rotation method in pump impeller. *Flow Measurement and Instrumentation*, **82**, 102061.

Livne, M., Rieger, J., Aydin, O. U., Taha, A. A., *et al.* 2019. A U-Net deep learning framework for high performance vessel segmentation in patients with cerebrovascular disease. *Frontiers in neuroscience*, **13**, 97.

Lobanoff, V. S., & Ross, R. R. 2013. *Centrifugal pumps: design and application.* Elsevier.

Loh, W.L., & Premanadhan, V. K. 2016. Experimental investigation of viscous oil-water flows in pipeline. *Journal of Petroleum Science and Engineering*, **147**, 87–97.

Lu, J., Wu, F., Liu, X., Zhu, B., Yuan, S., & Wang, J. 2022. Investigation of the mechanism of unsteady flow induced by cavitation at the tongue of a centrifugal pump based on the proper orthogonal decomposition method. *Physics of Fluids*, **34**(10), 105113.

Lumley, J. L. 1967. The structure of inhomogeneous turbulent flows. *Atmospheric turbulence and radio wave propagation.*

Ma, X., & Karniadakis, G. E. 2002. A low-dimensional model for simulating three-dimensional cylinder flow. *Journal of Fluid Mechanics*, **458**, 181–190.

Mittag, S., & Gabi, M. 2016. Experimental investigation on pump-intake-elbow systems using refraction index matching and TR-SPIV. *In: 16th International Symposium on Transport Phenomena and Dynamics of Rotating Machinery.*

Monte Verde, W. 2016. *Modelagem do Desempenho de Bombas de BCS Operando com Misturas Gás-óleo Viscoso.* Ph.D. thesis, University of Campinas.

Monte Verde, W., Biazussi, J. L., Sassim, N. A., & Bannwart, A. C. 2017. Experimental study of gas-liquid two-phase flow patterns within centrifugal pumps impellers. *Experimental Thermal and Fluid Science*, **85**, 37–51.

Morales, R., Pereyra, E., Wang, S., & Shoham, O. 2013. Droplet formation through centrifugal pumps for oil-in-water dispersions. *Spe Journal*, **18**(01), 172–178.

MOURA, H. L. 2017. *Análise da qualidade de medidas F-PIV e da fluidodinâmica em coluna de bolhas utilizando invariantes caóticos= Quality analysis of F-PIV measurements and fluid dynamics study in a bubble column using chaotic invariants.* Ph.D. thesis, University of Campinas.

NI, D., HUANG, S., ZHANG, Y., GAO, B., & LU, S. 2023. Proper orthogonal decomposition energy analysis in a nuclear reactor coolant pump based on PIV at the best efficiency point. *Nuclear Engineering and Design*, **410**, 112386.

OLIVIER, V., *ET AL.* 2010. *Airy functions and applications to physics.* World Scientific.

PANTON, R. L. 2013. *Incompressible flow.* 4 edn. John Wiley & Sons.

PAONE, N., RIETHMULLER, M. L., & VAN DEN BRAEMBUSSCHE, R. A. 1989. Experimental investigation of the flow in the vaneless diffuser of a centrifugal pump by particle image displacement velocimetry. *Experiments in Fluids*, **7**(6), 371–378.

PEDERSEN, N., LARSEN, P. S., & JACOBSEN, C. B. 2003. Flow in a centrifugal pump impeller at design and off-design conditions—part I: particle image velocimetry (PIV) and laser Doppler velocimetry (LDV) measurements. *Journal of Fluids Engineering*, **125**(1), 61–72.

PERISSINOTTO, R. M. 2023. *Estudo experimental de visualização de escoamentos no interior de impelidores de bombas centrífugas.* Ph.D. thesis, University of Campinas.

PERISSINOTTO, R. M., MONTE VERDE, W., GALLASSI, M., GONÇALVES, G. F. N., CASTRO, M. S., CARNEIRO, J., BIAZUSSI, J. L., & BANNWART, A. C. 2019a. Experimental and numerical study of oil drop motion within an ESP impeller. *Journal of Petroleum Science and Engineering*, **175**, 881–895.

PERISSINOTTO, R. M., MONTE VERDE, W., CASTRO, M. S., BIAZUSSI, J. L., ESTEVAM, V., & BANNWART, A. C. 2019b. Experimental investigation of oil drops behavior in dispersed oil-water two-phase flow within a centrifugal pump impeller. *Experimental Thermal and Fluid Science*, **105**, 11–26.

PERISSINOTTO, R. M., MONTE VERDE, W., PERLES, C. E., BIAZUSSI, J. L., CASTRO, M. S., & BANNWART, A. C. 2020. Experimental analysis on the behavior of water drops dispersed in oil within a centrifugal pump impeller. *Experimental Thermal and Fluid Science*, **112**, 109969.

PERISSINOTTO, R. M., MONTE VERDE, W., BIAZUSSI, J. L., BULGARELLI, N. A. V., FONSECA, W. D. P., CASTRO, M. S., FRANKLIN, E. M., & BANNWART, A. C. 2021. Flow visualization in centrifugal pumps: A review of methods and experimental studies. *Journal of Petroleum Science and Engineering*, 108582.

PERISSINOTTO, R. M., CERQUEIRA, R. F. L., FONSECA, W. D. P., BIAZUSSI, J. L., MONTE VERDE, W., BANNWART, A. C., FRANKLIN, E. M., & CASTRO, M. S. 2023. Particle image velocimetry in a centrifugal pump: Details of the fluid flow at different operation conditions. *Flow Measurement and Instrumentation*, **89**, 102282.

PERISSINOTTO, R. M., CERQUEIRA, R. F. L., MONTE VERDE, W., FONSECA, W. D. P., FRANKLIN, E. M., & CASTRO, M. S. 2024a. Analysis of energy losses and head produced by a radial impeller using particle image velocimetry (no prelo). *Journal of the Brazilian Society of Mechanical Sciences and Engineering.*

PERISSINOTTO, R. M., FONSECA, W. D. P., CERQUEIRA, R. F. L., MONTE VERDE, W., BANNWART, A. C., FRANKLIN, E. M., & CASTRO, M. S. 2024b. Particle image velocimetry in a centrifugal pump: Influence of walls on the flow at different axial positions. *Journal of Fluids Engineering*, **146**(3).

POPE, S. B. 2000. *Turbulent flows.* Cambridge university press.

PRASAD, A. K. 2000. Stereoscopic particle image velocimetry. *Experiments in fluids*, **29**(2), 103–116.

RAFFEL, M., WILLERT, C. E., SCARANO, F., KÄHLER, C. J., WERELEY, S. T., & KOMPENHANS, J. 2018. *Particle image velocimetry: a practical guide.* Springer.

REYNOLDS, O. 1895. On the dynamical theory of incompressible viscous fluids and the determination of the criterion. *Philosophical transactions of the royal society a*, 123–164.

RODRIGUEZ, O. M. H., & OLIEMANS, R. V. A. 2006. Experimental study on oil–water flow in horizontal and slightly inclined pipes. *International Journal of Multiphase Flow*, **32**(3), 323–343.

RONNEBERGER, O., FISCHER, P., & BROX, T. 2015. U-net: Convolutional networks for biomedical image segmentation. *Pages 234–241 of: Medical Image Computing and Computer-Assisted Intervention–MICCAI 2015: 18th International Conference, Munich, Germany, October 5-9, 2015, Proceedings, Part III 18*. Springer.

SCARANO, F. 2001. Iterative image deformation methods in PIV. *Measurement science and technology*, **13**(1), R1.

SCARANO, F. 2012. Tomographic PIV: principles and practice. *Measurement Science and Technology*, **24**(1), 012001.

SCARANO, F., & RIETHMULLER, M. L. 1999. Iterative multigrid approach in PIV image processing with discrete window offset. *Experiments in Fluids*, **26**(6), 513–523.

SCHÄFER, J., SCHMITT, P., HLAWITSCHKA, M. W., & BART, HANS-JÖRG. 2019. Measuring particle size distributions in multiphase flows using a convolutional neural network. *Chemie Ingenieur Technik*, **91**(11), 1688–1695.

SCHMITT, P., SIBIRTSEV, S., HLAWITSCHKA, M. W., STYN, R., JUPKE, A., & BART, HANS-JÖRG. 2021. Droplet Size Distributions of Liquid-Liquid Dispersions in Centrifugal Pumps. *Chemie Ingenieur Technik*, **93**(1-2), 129–142.

SEMERARO, O., BELLANI, G., & LUNDELL, F. 2012. Analysis of time-resolved PIV measurements of a confined turbulent jet using POD and Koopman modes. *Experiments in fluids*, **53**(5), 1203–1220.

SEMLITSCH, B., & MIHĂESCU, M. 2016. Flow phenomena leading to surge in a centrifugal compressor. *Energy*, **103**, 572–587.

SEMLITSCH, B., WANG, Y., & MIHĂESCU, M. 2014. Flow effects due to pulsation in an internal combustion engine exhaust port. *Energy Conversion and Management*, **86**, 520–536.

SHAO, C., LI, C., & ZHOU, J. 2018. Experimental investigation of flow patterns and external performance of a centrifugal pump that transports gas-liquid two-phase mixtures. *International Journal of Heat and Fluid Flow*, **71**, 460–469.

SHAOFEI, W., HAOWEN, X., ZHONGYANG, Q., & CHONG, P. 2023. Coherent flow structures near tongue region in a centrifugal fan with forward-curved blades. *Journal of Fluids Engineering*, **145**(3), 31202.

SHAVIT, U., LOWE, R. J., & STEINBUCK, J. V. 2007. Intensity capping: a simple method to improve cross-correlation PIV results. *Experiments in Fluids*, **42**, 225–240.

SHENG, J., MENG, H., & FOX, R. O. 2000. A large eddy PIV method for turbulence dissipation rate estimation. *Chemical engineering science*, **55**(20), 4423–4434.

SINHA, M., & KATZ, J. 2000. Quantitative visualization of the flow in a centrifugal pump with diffuser vanes—I: on flow structures and turbulence. *Journal of Fluids Engineering*, **122**(1), 97–107.

SIROVICH, L. 1987. Turbulence and the dynamics of coherent structures. I. Coherent structures. *Quarterly of Applied Mathematics*, **45**(3), 561–571.

SMAGORINSKY, J. 1963. General circulation experiments with the primitive equations: I. The basic experiment. *Monthly weather review*, **91**(3), 99–164.

SMITS, A. J. 2012. *Flow visualization: techniques and examples.* World Scientific.

SOUZA, L. F., MIOTTO, R. F., & WOLF, W. R. 2024. Analysis of transient and intermittent flows using a multidimensional empirical mode decomposition. *Theoretical and Computational Fluid Dynamics*, 1–21.

STANISLAS, M., & MONNIER, J. C. 1997. Practical aspects of image recording in particle image velocimetry. *Measurement Science and Technology*, **8**(12), 1417.

STEL, H., OFUCHI, E. M., SABINO, R. H. G., ANCAJIMA, F. C., ET AL. 2019. Investigation of the motion of bubbles in a centrifugal pump impeller. *Journal of Fluids Engineering*, **141**(3), 031203.

Taira, K., Brunton, S. L., Dawson, S. T. M., Rowley, C. W., *et al.* 2017. Modal analysis of fluid flows: An overview. *Aiaa Journal*, **55**(12), 4013–4041.

Taira, K., Hemati, M. S., Brunton, S. L., Sun, Y., *et al.* 2020. Modal analysis of fluid flows: Applications and outlook. *AIAA journal*, **58**(3), 998–1022.

Tang, Y., Wang, F., Wang, C., Ye, C., Qu, Q., & Xu, J. 2024. Investigation on the influence of seal clearance leakage on the rotating stall characteristics for a centrifugal pump. *Physics of Fluids*, **36**(2).

Tennekes, H., & Lumley, J. L. 1972. *A first course in turbulence.* MIT press.

Thielicke, W., & Sonntag, R. 2021. Particle Image Velocimetry for MATLAB: Accuracy and enhanced algorithms in PIVlab. *Journal of Open Research Software*, **9**(1).

Towne, A., Schmidt, O. T., & Colonius, T. 2018. Spectral proper orthogonal decomposition and its relationship to dynamic mode decomposition and resolvent analysis. *Journal of Fluid Mechanics*, **847**, 821–867.

Ullum, U., Schmidt, J. J., Larsen, P. S., & McCluskey, D. R. 1998. Statistical analysis and accuracy of PIV data. *Journal of Visualization*, **1**, 205–216.

Van Dyke, M. 1982. *An album of fluid motion.* Vol. 176. Parabolic Press Stanford.

Van Oudheusden, BW. 2013. PIV-based pressure measurement. *Measurement Science and Technology*, **24**(3), 032001.

Vernet, R., Thomas, L., & David, L. 2009. Analysis and reconstruction of a pulsed jet in crossflow by multi-plane snapshot POD. *Experiments in fluids*, **47**(4), 707–720.

Versteeg, H. K., & Malalasekera, W. 2007. *An introduction to computational fluid dynamics: the finite volume method.*

Verwey, C., & Birouk, M. 2022. Dissipation rate estimation in a highly turbulent isotropic flow using 2D-PIV. *Flow, Turbulence and Combustion*, **109**(3), 647–665.

Virtanen, P., Gommers, R., Oliphant, T. E., Haberland, M., *et al.* 2020. SciPy 1.0: Fundamental Algorithms for Scientific Computing in Python. *Nature Methods*, **17**, 261–272.

Volk, M. 2013. *Pump characteristics and applications.* CRC Press.

Wang, W., Gong, J., & Angeli, P. 2011. Investigation on heavy crude-water two phase flow and related flow characteristics. *International journal of multiphase flow*, **37**(9), 1156–1164.

Wang, X., Wang, Y., Liu, H., Xiao, Y., Jiang, L., & Li, M. 2023. A numerical investigation on energy characteristics of centrifugal pump for cavitation flow using entropy production theory. *International Journal of Heat and Mass Transfer*, **201**, 123591.

Wang, Y., Yang, H., Chen, B., Gao, P., Chen, H., & Zhu, Z. 2019. Analysis of vortices formed in flow passage of a five-bladed centrifugal water pump by means of PIV method. *AIP advances*, **9**(7).

Weiss, J. 2019. A tutorial on the proper orthogonal decomposition. *Page 3333 of: AIAA Aviation 2019 Forum.*

Wereley, S. T., & Meinhart, C. D. 2001. Second-order accurate particle image velocimetry. *Experiments in fluids*, **31**(3), 258–268.

Wernet, M. P. 2000. Development of digital particle imaging velocimetry for use in turbomachinery. *Experiments in Fluids*, **28**(2), 97–115.

Westerweel, J. 1993. *Digital particle image velocimetry: Theory and application.* Ph.D. thesis, Delft University of Technology.

Westerweel, J., & Scarano, F. 2005. Universal outlier detection for PIV data. *Experiments in fluids*, **39**, 1096–1100.

White, F. M. 2015. *Fluid mechanics.* 8 edn. McGraw-Hill.

Wieneke, B. 2005. Stereo-PIV using self-calibration on particle images. *Experiments in fluids*, **39**, 267–280.

WILLCOX, K. 2006. Unsteady flow sensing and estimation via the gappy proper orthogonal decomposition. *Computers & Fluids*, **35**(2), 208–226.

WILLERT, C. E., & GHARIB, M. 1991. Digital particle image velocimetry. *Experiments in fluids*, **10**(4), 181–193.

XU, D., & CHEN, J. 2013. Accurate estimate of turbulent dissipation rate using PIV data. *Experimental Thermal and Fluid Science*, **44**, 662–672.

YUAN, D., DENG, J., HAN, R., LI, D., & TAN, S. 2021. Experimental study on flow structures of central blockage accidents in a rectangular channel using PIV and POD. *Annals of Nuclear Energy*, **153**, 108037.

ZHANG, N., GAO, B., LI, Z., NI, D., & JIANG, Q. 2018. Unsteady flow structure and its evolution in a low specific speed centrifugal pump measured by PIV. *Experimental Thermal and Fluid Science*, **97**, 133–144.

ZHANG, R., GUO, R., YANG, J., & LUO, J. 2017. Inverse method of centrifugal pump impeller based on proper orthogonal decomposition (POD) method. *Chinese Journal of Mechanical Engineering*, **30**(4), 1025–1031.

ZHANG, Z., CHEN, H., YIN, J., MA, Z., ET AL. 2021. Unsteady flow characteristics in centrifugal pump based on proper orthogonal decomposition method. *Physics of Fluids*, **33**(7), 075122.

ZHAO, L., CHANG, Z., ZHANG, Z., HUANG, R., & HE, D. 2021. Visualization of gas-liquid flow pattern in a centrifugal pump impeller and its influence on the pump performance. *Measurement: Sensors*, **13**, 100033.